Earth Materials and Environmental Applications 2020

Lead Guest Editor: Zhaohui Li
Guest Editors: Guocheng Lv and Jianxi Zhu

Earth Materials and Environmental Applications 2020

Earth Materials and Environmental Applications 2020

Lead Guest Editor: Zhaohui Li
Guest Editors: Guocheng Lv and Jianxi Zhu

Chief Editor

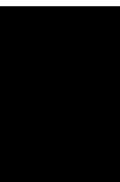Amit Bandyopadhyay, USA

Editorial Board

Yuri Ribakov, Israel
Aniello Riccio, Italy
Anna Richelli, Italy
Antonio Riveiro, Spain
Marco Rossi, Italy
Pascal Roussel, France
Fernando Rubio-Marcos, Spain
Francesco Ruffino, Italy
Mark H. Rümmeli, China
Pietro Russo, Italy
F.H. Samuel, Canada
MariaGabriella Santonicola, Italy
Hélder A. Santos, Finland
Carlo Santulli, Italy
Fabrizio Sarasini, Italy
Michael J. Schu#tze, Germany
Raffaele Sepe, Italy
Mercedes Solla, Spain
Donato Sorgente, Italy
Charles C. Sorrell, Australia
Andres Sotelo, Spain
Damien Soulat, France
Adolfo Speghini, Italy
Antonino Squillace, Italy
Koichi Sugimoto, Japan
Sam-Shajing Sun, USA
Baozhong Sun, China
Youhong Tang, Australia
Shengwen Tang, China
Kohji Tashiro, Japan
Hao Tong, China
Miguel Angel Torres, Spain
Laszlo Toth, France
Achim Trampert, Germany
Tomasz Trzepieciński, Poland
Matjaz Valant, Slovenia
Luca Valentini, Italy
Lijing Wang, Australia
Zhongchang Wang, Portugal
Jörg M. K. Wiezorek, USA
Jiang Wu, China
Guoqiang Xie, China
Jinyang Xu, China
Zhonghua Yao, China
Yee-wen Yen, Taiwan
Wenbin Yi, China
Hao Yi, China

Tetsu Yonezawa, Japan
Hiroshi Yoshihara, Japan
Lenka Zaji#c#kova#, Czech Republic
Zhigang Zang, China
Michele Zappalorto, Italy
Jinghuai Zhang, China
Gang Zhang, Singapore
Mikhail Zheludkevich, Germany
Wei Zhou, China
You Zhou, Japan
Hongtao Zhu, Australia

Contents

Editorial

Earth Materials and Environmental Applications 2020

Zhaohui Li [iD],[1] **Guocheng Lv,**[2] **and Jianxi Zhu**[3]

[1]*Geosciences Department, University of Wisconsin-Parkside, Kenosha, WI 53144, USA*
[2]*China University of Geosciences, Beijing, China*
[3]*Chinese Academy of Sciences, Guangzhou, China*

Correspondence should be addressed to Zhaohui Li; li@uwp.edu

The special issues of Earth Materials and Environmental Applications were published in 2015 and 2016 in *Adv. Mater. Sci. Eng.* Strong positive influence on the communities of geoscientists and environmental engineers resulted in our initiation of proposing the 3rd special issue in 2020. Due to the COVID-19 pandemic, the manuscript submission was seriously affected. As such, we had only 6 papers published in this special issue. Still, the special issue had research related to Earth materials from nuclear waste disposal, to deep well strip mining, and to use of Earth materials for contaminant removal from water. In the area of improvement of the permeability of clayey soil, double cutoff transverse relaxation times (T2 cutoffs) using low-field nuclear magnetic resonance (NMR) technology were developed. Studies on eight types of artificial clayey soil with different mineralogical compositions showed that the prediction accuracy of the improved model was much higher. In order to promote the sustainable use of oil shale residues, a novel subgrade material (SOF) composed of silty clay, oil shale ash residue, and fly ash was developed. The road performance, dynamic properties, and environment impact tests on mechanical property and environmental safety of an industrial residue waste subgrade material were evaluated. The deformation variation of the accumulation settlement of SOF under vehicle loadings after several years was far lower than the limit of expressway and Grade I highway. Furthermore, the chemical stability and toxicity of SOF leachates are in line with the benchmarks of Class II surface water and Class III ground water. In the area of surface and new building deformation analysis of deep well strip mining, advanced measuring instruments were developed on the stable surface of the old mining area and a simulation was used to determine the subsidence factor of different mining depths, mining widths, mining lengths, and mining thicknesses. The surface deformation was simulated and calculated, and the relationship between the different load positions, load sizes, loading building sizes, and the surface-activated deformation was determined. In another study, numerical modelling to predict the maturation of the clay barrier was developed to evaluate clay seal maturation in deep boreholes with nuclear waste and the results from simulation were compared to those from laboratory tests with good agreement. The effect of calcium carbonate on the mechanical properties and microstructure of red clay was studied by adding precipitated calcium carbonate to red clay at ratios of 0%, 5%, 10%, 15%, and 20%, and then, shear tests were conducted. The results showed that as the calcium carbonate content increased, the strength of red clay first decreased and then increased with a maximum strength obtained with 20% calcium carbonate. And, higher calcium carbonate content resulted in stronger agglomeration of red clay particles in the soil samples. In the study of sorptive removal of color dye safranin O (SO) by fibrous clay minerals and zeolites, it was found that the cation exchange capacity (CEC) of the minerals played a key role in SO$^+$ removal and the sorbed SO$^+$ cations were limited to the external surfaces of the minerals due to limited channel size of the fibrous minerals. In contrast, dense multilayers or admicelles of SO$^+$ formed on zeolite surfaces.

Zhaohui Li

Conflicts of Interest

We declare no conflicts of interest.

Acknowledgments

Research Article

An Improved Predictive Model for Determining the Permeability Coefficient of Artificial Clayey Soil Based on Double T_2 Cut-Offs

Zhen Lu [ID],[1,2] **Aimin Sha** [ID],[1,2] **Junfeng Gao** [ID],[1,2] **Meng Jia,**[1,2] **and Wentong Wang** [ID][1,2]

[1]*Key Laboratory for Special Area Highway Engineering of Ministry of Education, Chang'an University,*
 Xi'an, Shaanxi 710064, China
[2]*School of Highway, Chang'an University, Xi'an, Shaanxi 710064, China*

Correspondence should be addressed to Aimin Sha; ams@chd.edu.cn

Permeability is one of the most important engineering properties of clayey soil. However, the traditional method for determining the permeability coefficient is time-consuming. To establish a simple and accurate predictive method to obtain the permeability coefficient of artificial clayey soil based on the double cut-off transverse relaxation times (T_2 cut-offs) using low-field nuclear magnetic resonance (NMR) technology, eight kinds of artificial clayey soil with different mineralogical compositions were prepared in the laboratory. Evaporation tests at 40°C were carried out on the saturated artificial clayey soil samples in an oven. During the evaporation process, NMR tests were also performed on the artificial clayey soil every hour. The results showed that the evaporation process could be divided into three stages according to different evaporation rates: the constant rate stage (CRS), the falling rate stage (FRS), and the residual stage (RS). The water evaporated in the CRS and FRS was defined as the absolute movable water and the partially movable water, respectively. The water that could not evaporate in the RS was defined as the immovable water. Based on the cumulative signal amplitudes in the T_2 spectrum corresponding to different kinds of water, the double T_2 cut-offs were defined. On the basis of the double T_2 cut-offs and T_2 spectrum of the saturated sample, an improved Timur–Coates (TC) model was established. The prediction capability of the improved model was evaluated by finding the determination coefficient (R^2), mean absolute error (MAE), and root-mean-square error (RMSE). Compared with the typical TC model, the prediction accuracy of the improved model was much higher. In addition, the relationships between the double T_2 cut-offs and fractal dimension (D) of the T_2 spectrum of saturated artificial clayey soil were also identified.

1. Introduction

In recent years, artificial clayey soil has been widely used in various engineering constructions [1, 2]. As one of the most important engineering parameters, the permeability coefficient is closely related to the consolidation deformation of soil, seepage of groundwater, and diffusion of pollutants in environmental soil [1–3]. The permeability coefficient of artificial clayey soil needs to be determined before the design and construction of civil engineering, highway engineering, dam engineering, and refuse treatment engineering projects. The most commonly used method for measuring the permeability coefficient of an artificial clayey soil is variable head permeability testing. However, variable head permeability testing is time- and effort-consuming [4]. Many

previous studies have proposed models for predicting the permeability coefficient of clayey soil [1, 3–9]. However, these models need other parameters which are hard to obtain, and the errors between the measured and predicted values of permeability coefficients cannot be ignored. Therefore, it is necessary to build a simple and accurate predictive model.

In recent years, low-field NMR has been widely used to characterize the pore size distributions of porous media such as coal, shale, soil, and sandstone based on the T_2 spectra [10–13]. Based on the pore size distributions of porous media, many studies have been performed to predict the permeability of these porous media. Yao et al. established a permeability model for coal from the Schlumberger Doll Research (SDR) equation and Timur–Coates (TC) equation

by using NMR relaxometry [14]. Further, Li et al. classified the pore types of shale using the T_2 spectrum and proposed a permeability model for shale based on the regional TC model [15]. Rezaee et al. also developed a predictive model for sandstone on the basis of the NMR parameters from the T_2 spectrum [16]. However, few studies have focused on predictive models based on NMR for clayey soil. Therefore, to simplify the determination of the permeability coefficient of clayey soil, we previously proposed a novel method for predicting the permeability coefficients of artificial clayey soil based on the TC model by using low-field NMR [17]. This novel method was proved to have sufficient prediction capability. In this previous study [17], the water in the soil was classified into two kinds: free water and bound water. Based on this classification, a TC model for artificial clayey soil was proposed. The TC model was also called the free fluid model. In theory, the greater the detail in which the water in artificial clayey soil is classified, the higher the prediction accuracy of the model.

On the basis of our previous study [17], we continued to research on this prediction. The aim of this paper was to establish an improved model for predicting the permeability coefficients of clayey soil. Instead of the classification of water used in the previous study, the water in artificial clayey soil was divided into three kinds—absolute movable water, partially movable water, and immovable water—in this study. Based on this novel classification, an improved TC model was developed. The determination coefficient (R^2), mean absolute error (MAE), and root-mean-square error (RMSE) were used to evaluate the prediction accuracy of the improved model. Compared with the model proposed in our previous study, the prediction reliability of the novel model is better. The double T_2 cut-offs were defined to distinguish cumulative signal amplitudes in the T_2 spectrum corresponding to the weights of different kinds of water in artificial clayey soil. Similar to our previous study, the relationships between the double T_2 cut-offs and fractal dimension (D) were also established to remove evaporation testing from the determination process of the permeability coefficient. Using this method, the permeability coefficient of artificial clayey soil can be determined simply, quickly, and accurately.

2. Materials and Methods

2.1. Materials. Two clay mineral (montmorillonite and kaolinite) powders and one sand powder were used in this study to prepare artificial clayey soil. The sand powder was purchased from Guangzhou Jialiang Mineral Products Co., Ltd. (Guangzhou, China). The montmorillonite and kaolinite powders were provided by Inner Mongolia Ningcheng Tianyu Chemical Co., Ltd. (Chifeng, China) and Guangzhou Yifeng Chemical Technology Co., Ltd. (Guangzhou, China), respectively. A Mastersizer 2000 laser particle analyzer was used to determine the grain size distributions of these three mineral powders in this study. The grain size distributions are depicted in Figure 1. The Atterberg limits, specific gravity values, and classifications of the three kinds of powders were determined following the methods in ASTM D4318, ASTM

D2487, and ASTM D2478, respectively. The X-ray fluorescence was also used to determine the chemical compositions of the powders. The basic properties of the three powders, including their Atterberg limits, specific gravity, and chemical composition, are summarized in Table 1.

2.2. Methods

2.2.1. NMR Theory. As a nondestructive, fast, and accurate testing technology, nuclear magnetic resonance technology is widely used to evaluate the pore characteristics of porous media [10, 12]. The NMR theory is briefly summarized as follows.

NMR relaxation consists of three parts: bulk relaxation, diffusion relaxation, and surface relaxation. The relaxation time can be divided into two categories: longitudinal relaxation time (T_1) and transverse relaxation time (T_2). The transverse relaxation time is more often used because it is shorter than the longitudinal relaxation time and easier to measure using an NMR analyzer [18]. The transverse relaxation time can be calculated by the following equation [10, 19–21]:

$$\frac{1}{T_2} = \frac{1}{T_{2B}} + \frac{1}{T_{2D}} + \frac{1}{T_{2S}}, \tag{1}$$

where T_{2B} is the transverse bulk relaxation time, T_{2D} is the transverse diffusion relaxation time, and T_{2S} is the transverse surface relaxation time.

T2D can be calculated by the following [22]:

$$\frac{1}{T_{2D}} = \frac{C_d \left(\gamma G T_E \right)^2}{12}, \tag{2}$$

where C_d is the diffusion coefficient of the fluid in the pores, G is the gradient magnetic field intensity, and T_E is the echo interval time. When the magnetic field is uniform, G equals 0.

T2S can be calculated by the following equation [23]:

$$\frac{1}{T_{2S}} = \rho_2 \left(\frac{S}{V} \right)_{\text{pore}}, \tag{3}$$

where S is the surface area of the pore, V is the volume of the pore, and ρ_2 is the surface relaxivity of the pore surface. The surface relaxivity is mainly affected by the physicochemical properties of the soil particle surface [24].

The relationship between the surface area of the pore, the volume of the pore, and the diameter of the pore can be expressed by the following equation:

$$\frac{S}{V} = \frac{F_s}{r}, \tag{4}$$

where r is the diameter of the pore and F_s is the shape factor of the pore. For planar, columnar, and spherical pores, F_s is equal to 1, 2, and 3, respectively.

Equation (4) can be converted into

$$\frac{1}{T_{2S}} = \rho_2 \frac{F_s}{r}. \tag{5}$$

When the magnetic field is uniform, G equals 0, so $1/T_{2D}$ equals 0. When the liquid in the pore is distilled water, T_{2B} is
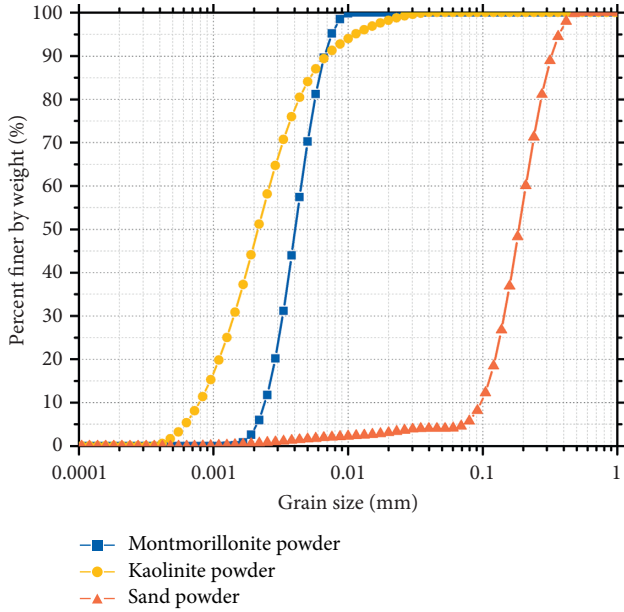
FIGURE 1: The grain size distributions of the sand, kaolinite, and montmorillonite powders.

TABLE 1: Basic properties of the three mineral powders used in this study.

Property	Materials		
	Sand	Kaolinite	Montmorillonite
Atterberg limits			
Plastic limit (%)	—	32.00	61.34
Liquid limit (%)	—	68.99	178.65
Plasticity index	—	36.99	117.31
Grain size distribution			
Clay (%; <0.005 mm)	1.63	70.23	84.1
Silt (%; 0.005 mm–0.075 mm)	4.15	29.77	15.9
Sand (%; >0.075 mm)	94.22	0	0
Chemical composition			
SiO_2 (%)	98.85	57.82	66.63
Al_2O_3 (%)	0.57	35.24	16.07
K_2O (%)	—	3.89	—
Fe_2O_3 (%)	0.08	1.86	6.50
CaO (%)	0.18	—	3.99
MgO (%)	—	0.37	5.32
Specific gravity	2.68	2.76	2.61
Classification	—	CH	CH

much larger than T_{2S}, so $1/T_{2B}$ can also be considered negligible [25]. Equation (1) can then be simplified into the following equation:

$$\frac{1}{T_2} \approx \frac{1}{T_{2S}} = \rho_2 \frac{F_s}{r}. \tag{6}$$

From the previous equation, there is a linear relationship between T_2 and r. The quantity of pores with a specific pore size can then be obtained from the T_2 spectra of water-saturated samples. A small T_2 corresponds to a small pore and a large T_2 corresponds to a large pore [26].

2.2.2. Sample Preparation.

Eight artificial clayey soil samples were prepared in the laboratory. All the samples consisted of clay mineral (montmorillonite or kaolinite) and sand. Four samples consisted of montmorillonite and sand, while the other four consisted of kaolinite and sand. These two groups were named the M-group and K-group, respectively. The clay mineral (montmorillonite or kaolinite) contents in each group were increased from 40% to 100% at intervals of 20%. The eight artificial clayey soil samples were named after the clay mineral content and clay mineral type. For example, M80 consisted of montmorillonite and sand, and the clay mineral content was 80%.

All eight artificial clayey soils were prepared under laboratory conditions. The process of sample preparation is briefly summarized as follows. The mineral powders were oven-dried at 250°C for 24 hours to a constant weight. At 250°C, almost all of the water in the artificial clayey soil was removed and the structure of the clay particles was unaffected [27–30]. Next, the clay mineral powder and sand powder in a dry state were thoroughly mixed at fixed proportions. Then, distilled water was added to the mixtures until the water content reached the plastic limit. To make the mixtures reach a full hydration state, the mixtures were stirred using a mortar-mixing apparatus at 60 rounds/min for 5 min and put into self-sealing plastic bags for two days. Following the hydration period, the mixtures were shaped in a hollow cylinder with an inner diameter and height of 31.9 mm and 80 mm, respectively, using a Jack under static pressure to reach the fixed dry density. Finally, the eight artificial clayey soil samples were saturated by the vacuum saturation method.

2.2.3. NMR and Evaporation Tests.

A MesoMR12-150H-I NMR analyzer (NIUMAG Co., Ltd., Suzhou, China), shown in Figure 2, was used for NMR tests. The composition of the instrument used in this study was the same as that used in a previous study [21]. The parameters of the NMR tests in this study are shown in Table 2. The pulse sequence of the NMR tests used in this study was the Carr–Purcell–Meiboom–Gill (CPMG) pulse sequence [31]. Because of magnetic field inhomogeneities, the value of T_2 measured by a free induction decay (FID) pulse sequence is less than the actual value [10]. The CPMG pulse sequence selected in this study was the same as that in previous studies [20, 23, 26, 32]. The T_2 spectra were obtained automatically using the software installed on the NMR analyzer. Inversion software was developed based on inverse Laplace transform [33] and the simultaneous iterative reconstruction technique (SIRT) [34].

The NMR tests were first performed on the eight saturated samples and then carried out on the evaporated samples every hour until the T_2 spectrum did not change. The samples were evaporated in an oven, with the drying temperature set to 40°C to simulate the highest temperature of the subgrade under natural conditions. It is noted that the temperature of the sample has dramatic effects on the T_2 spectrum. The temperature of the sample needs to be equal to the temperature of the magnetic field (30°C). So, after the sample was taken out from the oven and before each NMR
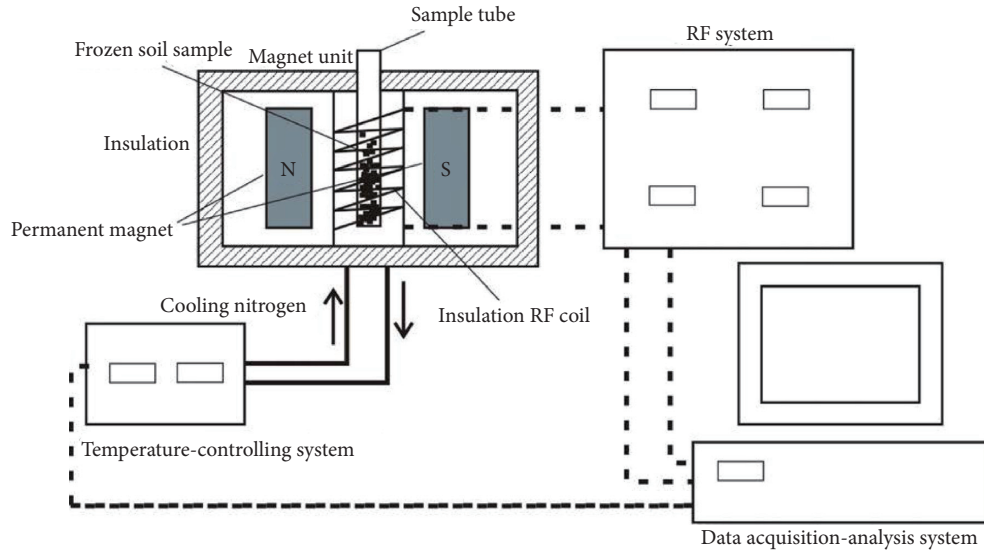
FIGURE 2: Composition of the MesoMR12-150H-I NMR analyzer [21].

TABLE 2: Parameters of the NMR tests.

Parameter	Value	Unit
Magnetic induction intensity	0.55	T
Frequency	13	MHz
Coil diameter	60	mm
Ambient temperature	30	°C
90° pulse width	20	μs
180° pulse width	30.48	μs
Sampling points	208018	—
Sampling frequency	200	kHz
Frequency delay	8	μs
Latency time of repeated sampling	8000	ms
Analog gain	20	—
Digital gain	3	—
Accumulated sampling number	4	—
Echo time	260	μs
Echo number	4000	—

test, the sample needed to be cooled to 30°C. During the cooling process, the sample was wrapped in plastic wrap to prevent further dehydration.

3. Results and Discussion

3.1. Morphology of T_2 Spectra during the Evaporation Process. The variations of the T_2 spectra during the evaporation process of artificial clayey soils consisting of different clay minerals (kaolinite and montmorillonite) and sand are presented in Figure 3. All the T_2 spectra in Figure 3 are unimodal, which suggests that the pores in both saturated and evaporated samples were distributed uniformly and continuously [15, 35]. The T_2 spectra of artificial clayey soil in the initial state shifted to the left with increasing clay content. According to equation (6), this might be because the relaxation coefficient increased or the pore diameter decreased with increasing clay content in the artificial clayey soil. All of the T_2 spectra of the eight artificial clayey soils shifted to the left with increasing evaporation time.

According to NMR theory, the pore size is proportional to T_2, so this means that the pore size kept decreasing during the evaporation process. This indicates that decreases in the pore size may be the reason for clayey soil shrinkage during evaporation [36].

According to our previous study [17], the weight of distilled water (m) in artificial clayey soil is proportional to the T_2 total signal amplitude (A_t), which is equal to the total area under the T_2 spectrum curve. The relationship between A_t and m can be expressed by equation (7); the R^2 value of equation (7) was 0.996, as shown in Figure 4. This indicated that the weight of evaporated water can be expressed by the attenuated cumulative T_2 signal amplitudes:

$$A_t = 302.6\,m. \tag{7}$$

The variation of the total T_2 signal amplitude with respect to evaporation time is shown in Figure 5. During evaporation, A_t kept decreasing, while the decay rate was different at various evaporation times. The decay rate of A_t was defined as R_t, which can be calculated by the following equation:

$$R_t = \frac{\Delta A_t}{t}, \tag{8}$$

where ΔA_t is the attenuated A_t during evaporation time t.

The R_t values for each hour during evaporation were calculated and are presented in Figure 6. From Figure 6, it can be seen that R_t was approximately constant firstly and then decreased to 0. According to the R_t values, the evaporation process can be divided into three stages: the constant rate stage (CRS), the falling rate stage (FRS), and the residual stage (RS). The demarcation points of the three stages were defined as T_f and T_r. The demarcation point of CRS and FRS is T_f, and the demarcation point of FRS and RS is T_r. The T_f values of artificial clayey soils which consisted of the same clay mineral were found to be the same. The T_f value of artificial clayey soil consisting of kaolinite and sand was 20 h,
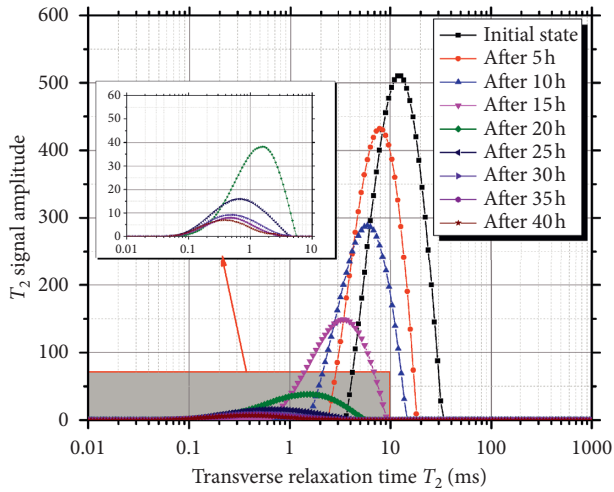
(a)
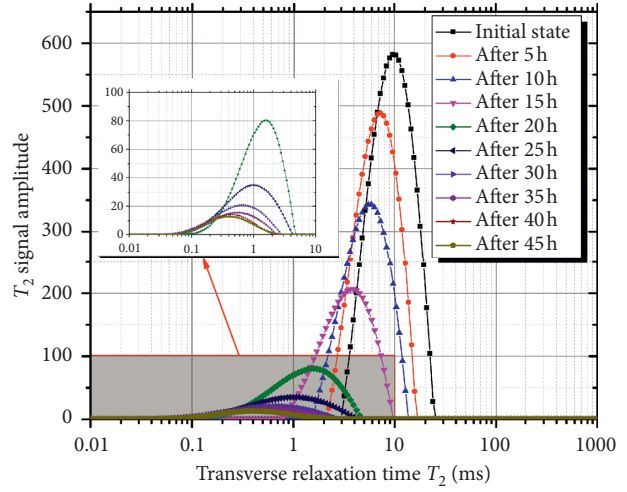
(b)
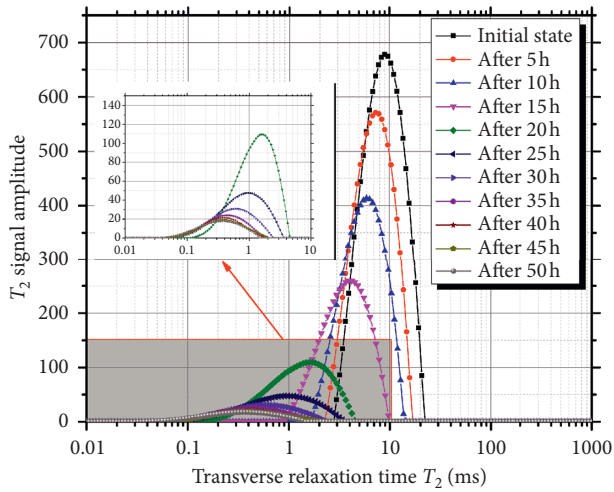
(c)
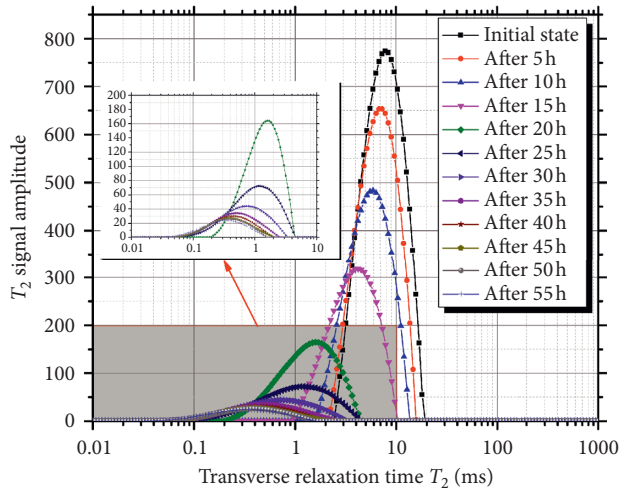
(d)
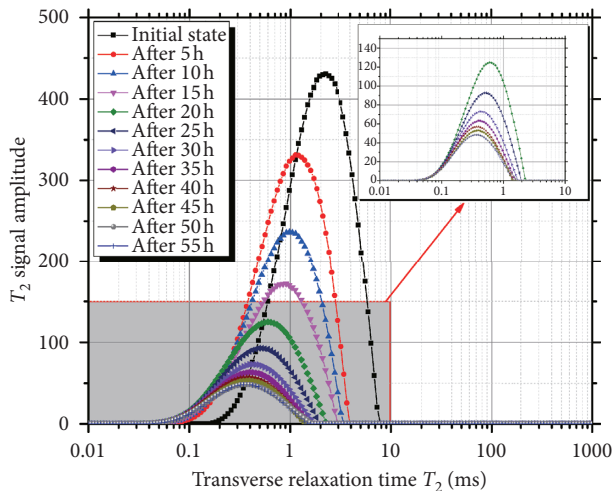
(e)
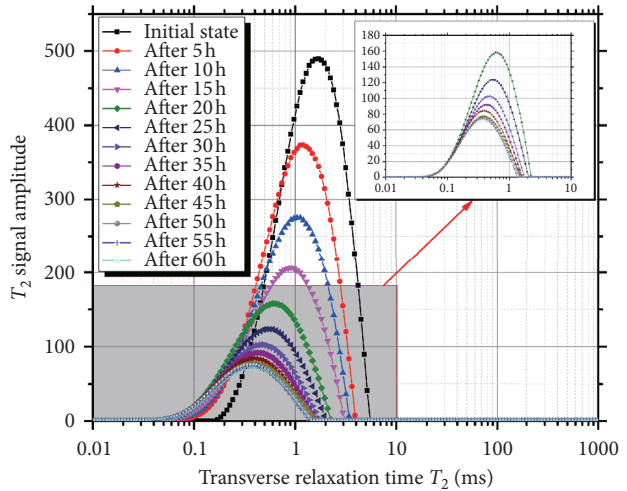
(f)

FIGURE 3: Continued.

(g)

(h)
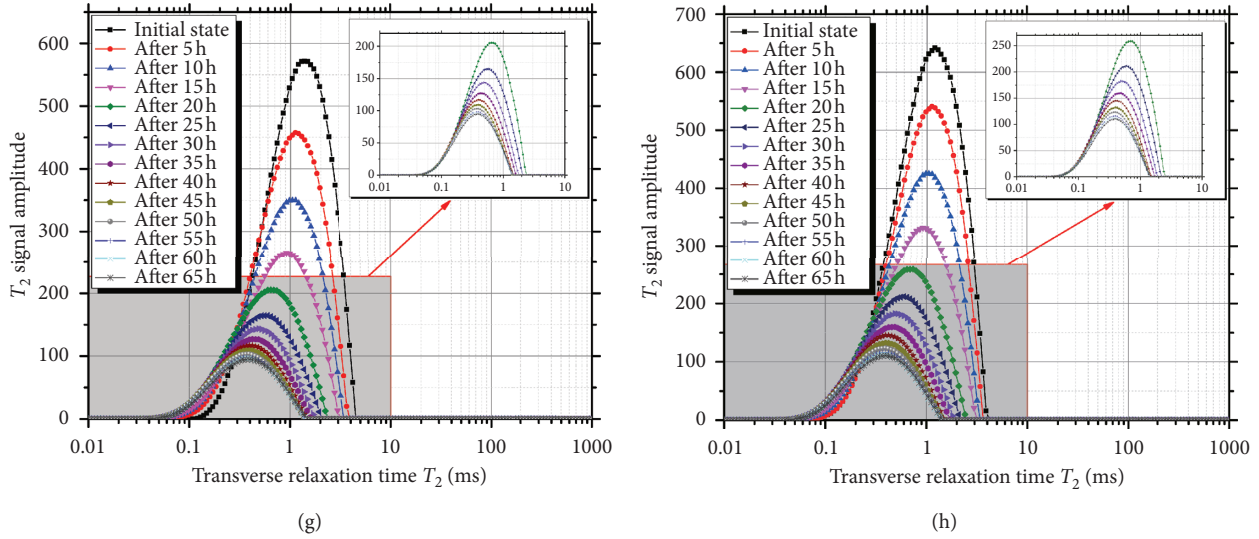
FIGURE 3: The variations of the T_2 spectra of artificial clayey soils during evaporation: (a) K40; (b) K60; (c) K80; (d) K100; (e) M40; (f) M60; (g) M80; (h) M100.
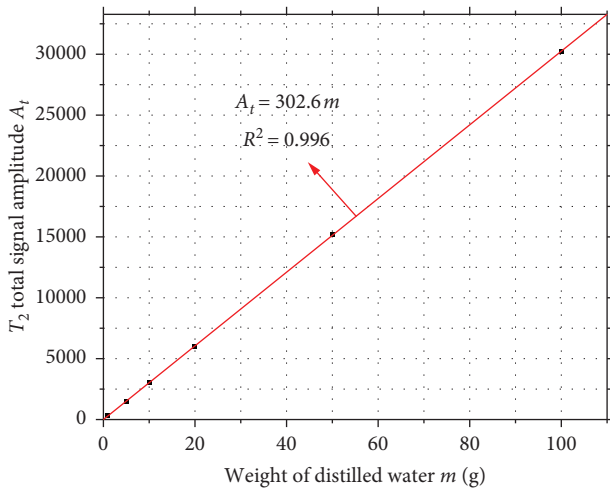
FIGURE 4: Relationship between the weight of distilled water in artificial clayey soil and the T_2 total signal amplitude.

while the T_f value of artificial clayey soil consisting of montmorillonite and sand was 6 h. The results indicated that the T_r values of artificial clayey soils with different clay mineral types and contents varied greatly.

3.2. The Improved TC Permeability Prediction Model.

The two most commonly used permeability prediction models of porous media based on NMR technology are the SDR model and the TC model. According to our previous study [17], the SDR model was not suitable for predicting the permeability coefficients of clayey soils that consist of different minerals. This can be explained by the fact that the relaxation coefficients of clayey soils with different mineralogical compositions vary greatly. The geometric mean transverse relaxation time (T_{2gm}) of clayey soils with different

mineralogical compositions cannot be used to compare the average pore size directly.

The TC model can be described by the following equation:

$$k_{\text{TC}} = a\varphi_{\text{NMR}}^{m}\left(\frac{\text{FFV}}{\text{BFV}}\right)^{n}, \tag{9}$$

where FFV and BFV are the volumes of free fluid and bound fluid, respectively, in a porous medium. The three empirical constants (a, m, n) are related to the properties of porous media. φ_{NMR} is the total porosity of artificial clayey soil as measured by NMR tests. For saturated artificial clayey soil, φ_{NMR} can be determined by the following equation:

$$\varphi_{\text{NMR}} = \frac{A_t}{302.6\rho_w V}, \tag{10}$$

where ρ_w is the density of distilled water and V is the volume of artificial clayey soil.

In our previous study [17], it was proved that the TC model can be used to determine the permeability coefficient of artificial clayey soil. In addition, the TC model is also called the free fluid model. The key to determining the permeability coefficient via the TC model is to calculate the volumes of two kinds of fluids (FFV and BFV) accurately. The FFV and BFV were defined as the water evaporated in the constant and other rate stages, respectively. However, it is more reasonable to divide the evaporation process into three stages according to Figure 6. This is because the greater the detail in which the water is classified, the higher the prediction accuracy of the model. In this study, the water evaporated in the CRS and FRS was defined as the absolute movable water and the partially movable water, respectively. The water that could not evaporate in the RS was defined as the immovable water. According to NMR theory, the weights of water evaporated in different stages correspond to different parts of the cumulative signal amplitudes in the T_2
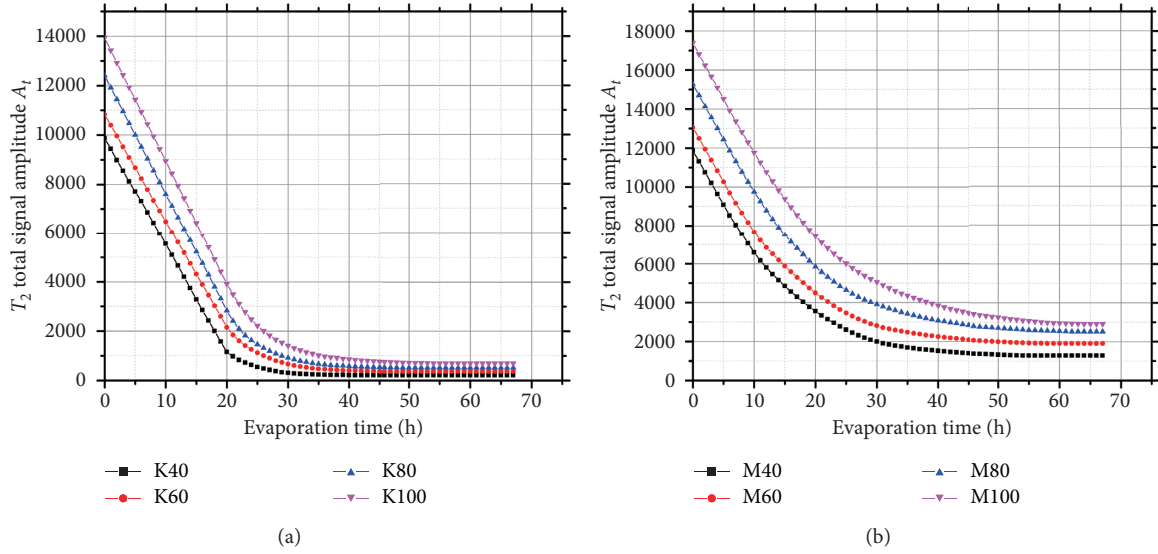
Figure 5: Variation of the total T_2 signal amplitude with respect to evaporation time: (a) K-group and (b) M-group.
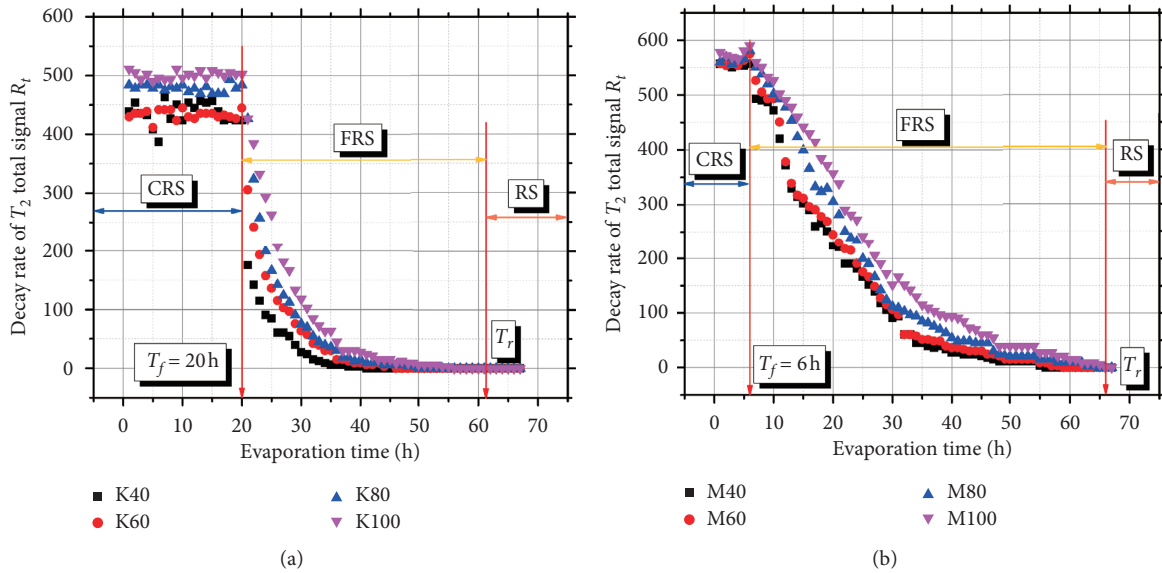
Figure 6: The decay rate of the T_2 total signal versus evaporation time: (a) K-group and (b) M-group.

spectra of saturated artificial clayey soils. The T_2 cut-off was used to discriminate the cumulative signal amplitudes corresponding to the different kinds of water. In this study, double T_2 cut-offs (T_{2cf} and T_{2cr}) were defined to discriminate the three kinds of water. As shown in Figure 7, the cumulative signal amplitudes between T_{2min} and T_{2cr} (A_{imw}) correspond to the immovable water. Similarly, the cumulative signal amplitudes between T_{2cr} and T_{2cf} (A_{pmw}) correspond to the partially movable water, and the cumulative signal amplitudes between T_{2cf} and T_{2max} correspond to the absolute movable water (A_{amw}). A_t, φ_{NMR}, A_{imw}, A_{pmw}, and A_{amw} values of the eight artificial clayey soils are summarized in Table 3.

To establish the improved TC permeability coefficient prediction model, the permeability coefficients (K_{TC}) of the

eight artificial clayey soils were also measured by variable head permeability tests. It is noted that the permeability coefficients are not the same as the permeability (k_{TC}) in the TC model. According to previous studies [17, 37], K_{TC} is proportional to k_{TC}. The TC model can thus be converted into the following equation:

$$K_{TC} = b \cdot k_{TC} = b \cdot a\varphi_{NMR}^m \left(\frac{FFV}{BFV}\right)^n = B\varphi_{NMR}^m \left(\frac{FFV}{BFV}\right)^n. \quad (11)$$

From the previous equation, there are relationships between K_{TC} and φ_{NMR} and the volume ratios of different kinds of water. The relationships between K_{TC} and φ_{NMR}, A_{pmw}/A_{amw}, and A_{imw}/A_{amw} are shown in Figure 8. As presented in Figure 8, K_{TC} decreased with increasing A_{pmw}/A_{amw} and A_{imw}/A_{amw}. It is noted that K_{TC} decreased with

(a)

(b)

(c)

(d)

(e)

(f)
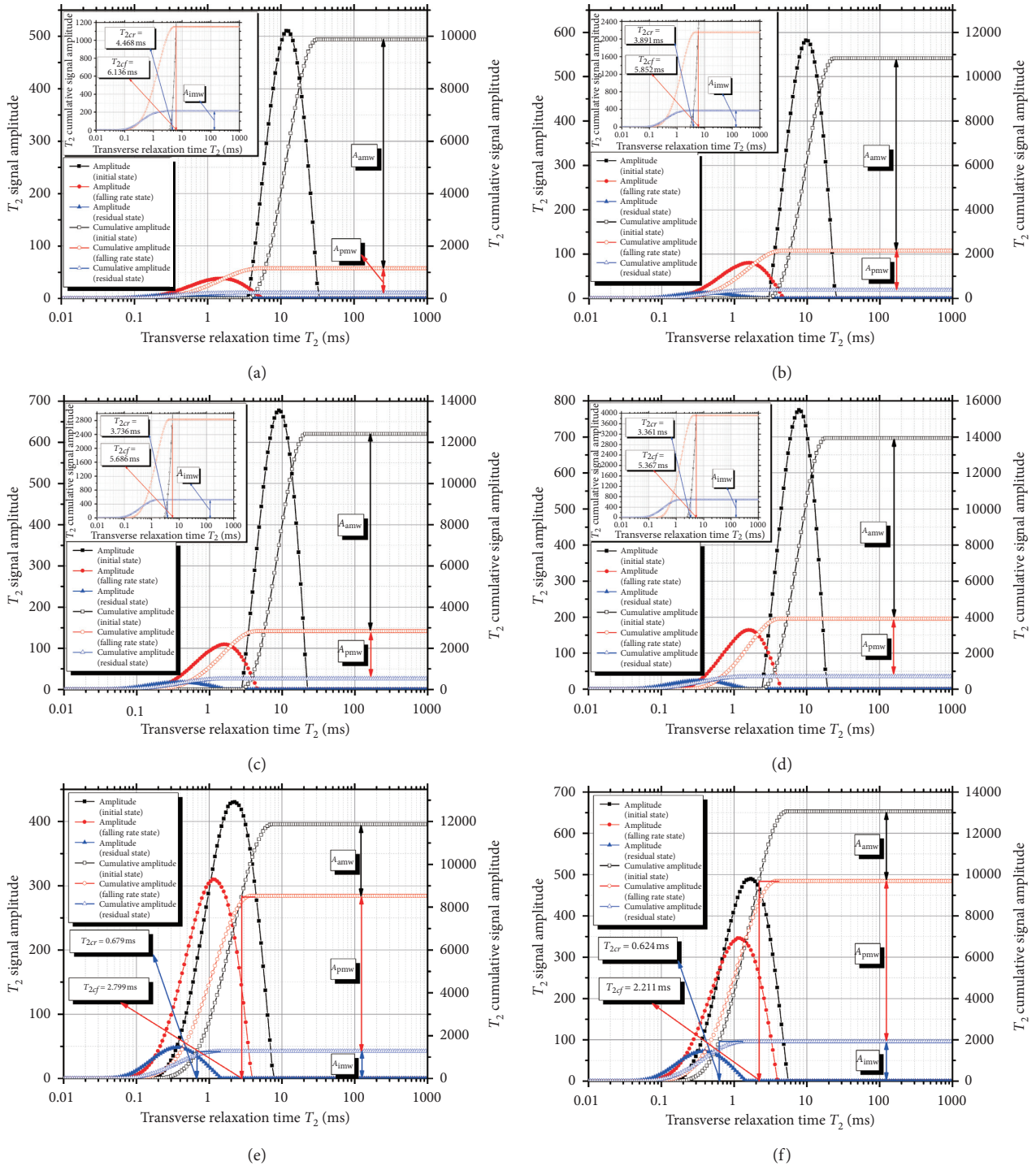
FIGURE 7: Continued.

(g)

(h)
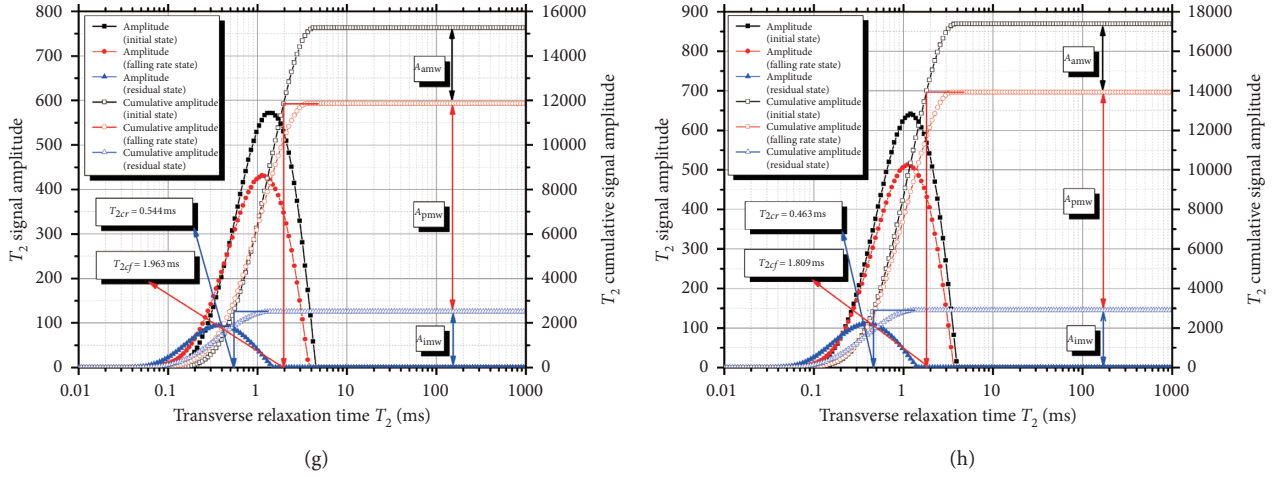
FIGURE 7: Double T_2 cut-offs of the eight artificial clayey soils: (a) K40, (b) K60, (c) K80, (d) K100, (e) M40, (f) M60, (g) M80, and (h) M100.

TABLE 3: A_t, φ_{NMR}, A_{imw}, A_{pmw}, and A_{amw} values of the eight kinds of artificial clayey soil.

|	A_t	φ_{NMR}	A_{imw}	A_{pmw}	A_{amw}
M40	11864.73	0.40843	1273.73	7253.32	3337.68
M60	13051.19	0.44927	1909.46	7782.87	3358.86
M80	15260.68	0.52533	2512.15	9353.37	3395.17
M100	17385.43	0.59847	2896.94	11032.8	3455.69
K40	9875.78	0.33996	213.38	938.06	8723.96
K60	10826.21	0.37268	371.38	1282.31	8972.52
K80	12407.74	0.42712	518.59	2314.89	9574.26
K100	13937.11	0.47977	695.33	3219.66	10022.11

increasing φ_{NMR} mainly because there were differences in the mineralogical compositions of the eight artificial clayey soils. For clayey soils consisting of the same mineral, K_{TC} decreased with decreasing φ_{NMR}.

As shown in Figure 8, the relationships between K_{TC} and φ_{NMR}, A_{pmw}/A_{amw}, and A_{imw}/A_{amw} can be expressed by the following equations:

$$K_{TC} = 0.027\varphi_{NMR}^{-8.337}, \tag{12}$$

$$K_{TC} = 3.891\left(\frac{A_{pmw}}{A_{amw}}\right)^{-1.789}, \tag{13}$$

$$K_{TC} = 0.751\left(\frac{A_{imw}}{A_{amw}}\right)^{-1.529}. \tag{14}$$

The R^2 values of equations (12)–(14) were 0.927, 0.984, and 0.983, respectively. On the basis of equations (11)–(14), the improved TC model could be further established. This model can be expressed by the following equation:

$$K_{TC} = 0.546\varphi_{NMR}^{-3.051}\left(\frac{A_{pmw}}{A_{amw}}\right)^{-0.156}\left(\frac{A_{imw}}{A_{amw}}\right)^{-0.632}. \tag{15}$$

Figure 9 presents a comparison of the predicted and measured permeability coefficients. All points are very close to the line $y = x$. This indicates that the improved TC model

can be used to reliably predict the permeability coefficient of artificial clayey soil.

R^2, mean absolute error (MAE), and root-mean-square error (RMSE) are often used to evaluate the prediction capability of a predictive model. These parameters can be determined by the following equations:

$$R^2 = 1 - \frac{\sum_{i=1}^{N}\left(X_{prei} - X_{meai}\right)^2}{\sum_{i=1}^{N}\left(X_{prei} - \overline{X}_{meai}\right)^2}, \tag{16}$$

$$\text{MAE} = \frac{1}{N}\sum_{i=1}^{N}\left|X_{prei} - X_{meai}\right|, \tag{17}$$

$$\text{RMSE} = \sqrt{\frac{1}{N}\sum_{i=1}^{N}\left[X_{prei} - X_{meai}\right]^2}, \tag{18}$$

where X_{prei}, X_{meai}, and $\overline{X}_{meai}$ symbolize the predicted, measured, and mean measured values, respectively.

This improved TC model was proposed based on double T_2 cut-offs. The typical TC model based on a single T_2 cut-off for artificial clayey soil was established in our previous study [17]. The R^2, MAE, and RMSE values of the two models are listed in Table 4 and shown in Figure 10. As shown in Table 4, the R^2, MAE, and RMSE values of the improved TC model are 0.999, 1.050, and 1.370, respectively. However, the corresponding values of the typical TC model are 0.957, 3.096, and 3.828, respectively. It can be seen that the R^2 value of the improved TC model is bigger than that of the typical TC model. This suggests that the connection between the measured K and predicted K in the improved TC model is stronger than that in the typical TC model. In addition, the MAE and RMSE values of the improved TC model are much smaller than those of the typical TC model. This indicates that the error between the measured K and predicted K of the improved TC model is much smaller than that of the typical TC model. The prediction capability of the improved TC model is thus much higher than that of the typical TC model.

(a)

(b)

(c)
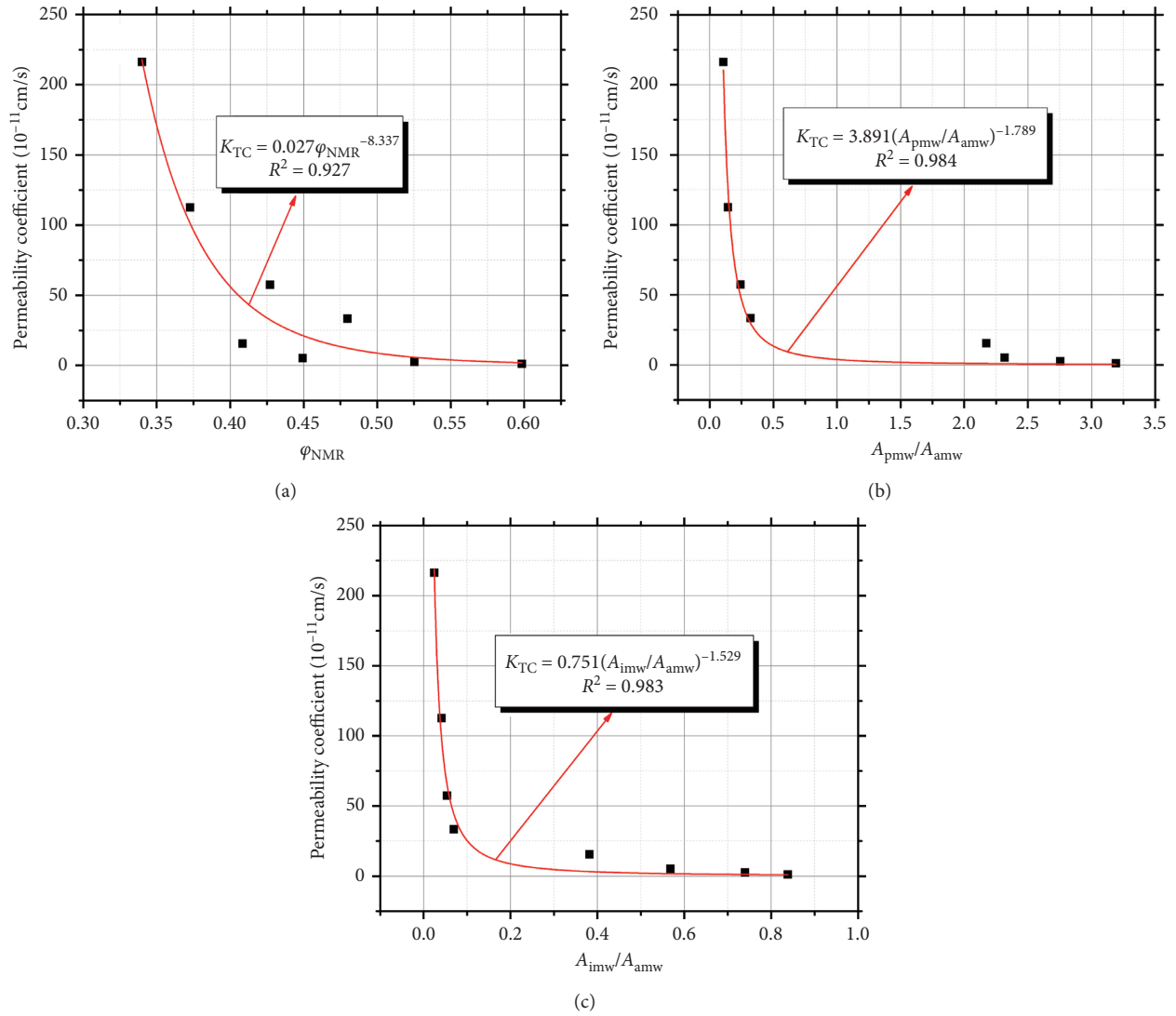
FIGURE 8: The relationships between K_{TC} and φ_{NMR}, A_{pmw}/A_{amw}, and A_{imw}/A_{amw}: (a) φ_{NMR}, (b) A_{pmw}/A_{amw}, and (c) A_{imw}/A_{amw}.
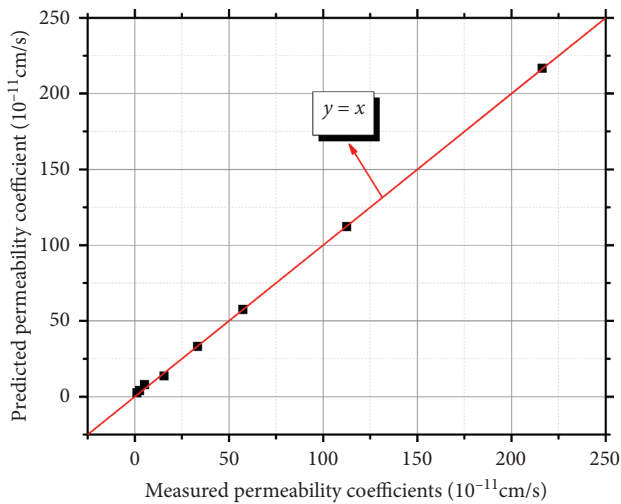
FIGURE 9: Comparison of the predicted and measured permeability coefficients.

TABLE 4: The determination coefficient (R^2), mean absolute error (MAE), and root-mean-square error (RMSE) values of the improved Timur–Coates (TC) model and typical TC model.

Model	R^2	MAE	RMSE
Improved TC model	0.999	1.050	1.370
Typical TC model	0.957	3.096	3.828

3.3. Determination of the Double T_2 Cut-Offs Based on Fractal Analysis. Before applying the improved TC model, it is necessary to determine the double T_2 cut-offs to classify the cumulative signal amplitudes of T_2 spectra corresponding to different kinds of water in artificial clayey soil. It takes a long time and great effort to determine the double T_2 cut-offs by evaporation tests. According to our previous study [17], the T_2 cut-off can be determined by fractal analysis. There is a linear relationship between the T_2 cut-off and the fractal dimension (D) of the T_2 spectrum of saturated artificial clayey soil. The D value can then be used to determine the
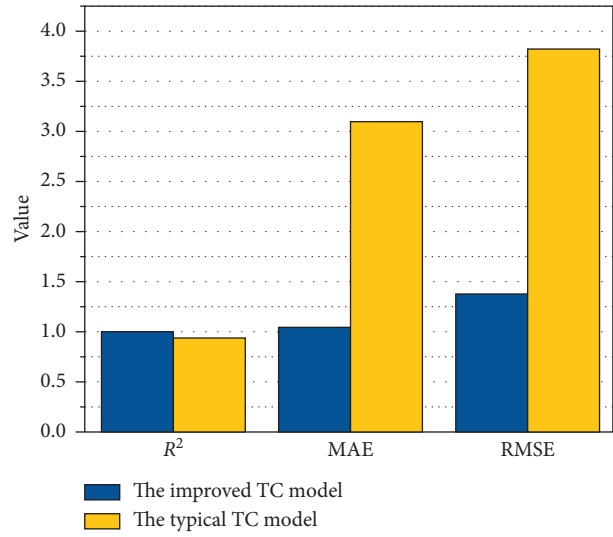
FIGURE 10: The R^2, MAE, and RMSE values of the improved and typical TC models.

TABLE 5: The D, T_{2cr}, and T_{2cf} values of the eight artificial clayey soils.

Artificial clayey soil	M40	M60	M80	M100	K40	K60	K80	K100
D	2.605	2.573	2.535	2.505	2.447	2.406	2.354	2.303
T_{2cr}	0.679	0.624	0.544	0.463	4.468	3.891	3.736	3.361
T_{2cf}	2.799	2.211	1.963	1.809	6.136	5.852	5.686	5.367
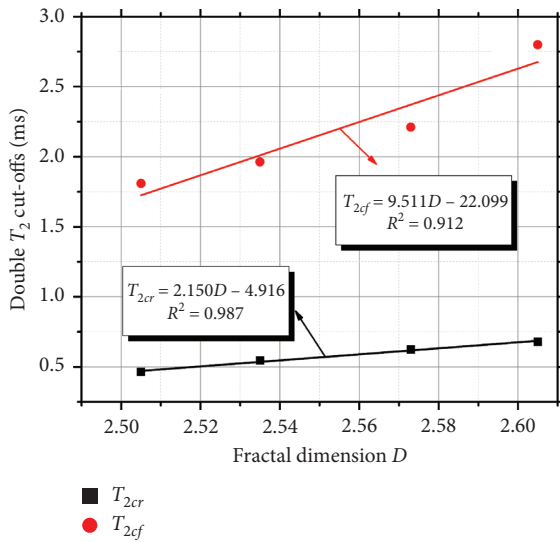
(a)
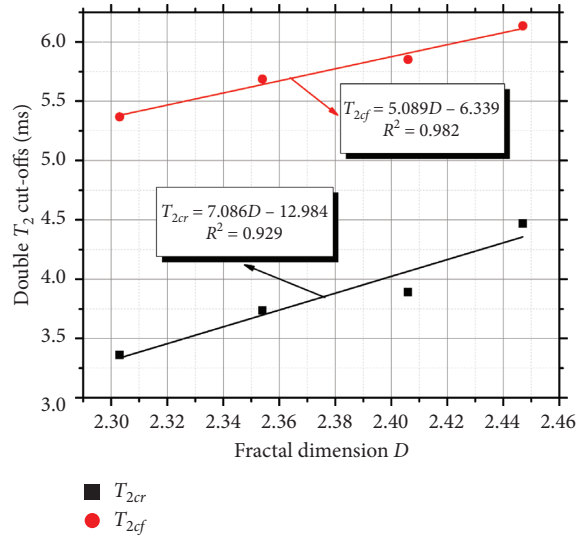
(b)

FIGURE 11: The relationships between the double T_2 cut-offs and fractal dimensions: (a) M-group and (b) K-group.

double T_2 cut-offs. It is noteworthy that the fractal dimensions were determined based on the T_2 spectra obtained from the results of the NMR tests. The pore size of an artificial clayey soil is proportional to T_2, so, actually, the fractal dimensions were determined according to the pore size distributions of the artificial clayey soil. So, the fractal dimensions in the manuscript were treated for space. The D,

T_{2cr}, and T_{2cf} values of the eight artificial clayey soils are listed in Table 5. As shown in Table 5, a smaller fractal dimension was obtained for samples with higher clay content. Further, the fractal dimensions of the M series were larger than those of the K series. According to the relevant literature [38, 39], the probability density function of pore size can be written as follows:

(a)

(b)
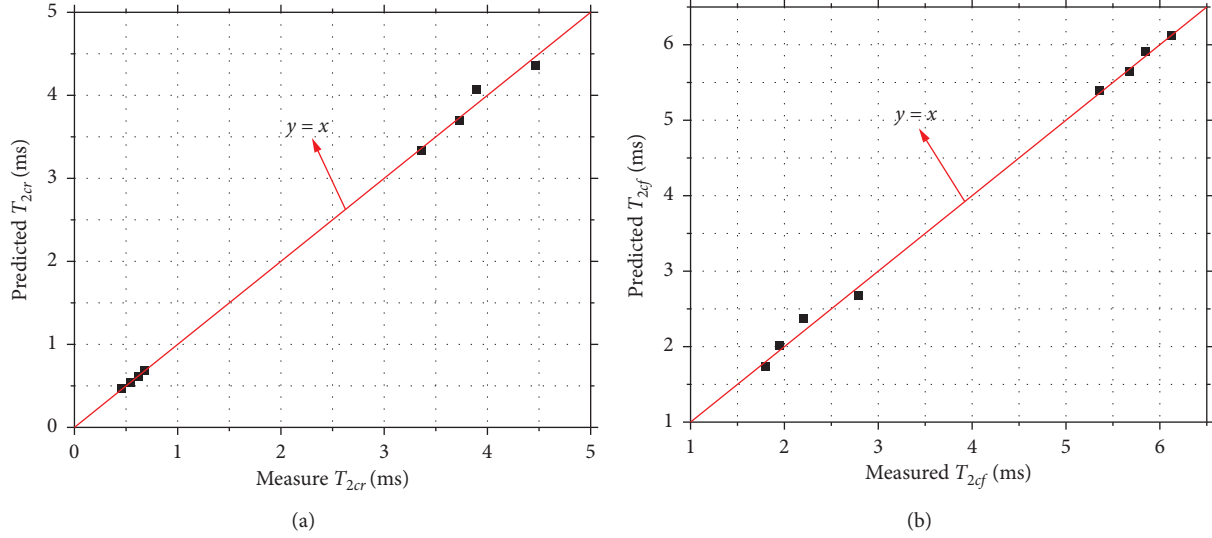
FIGURE 12: Comparison of the predicted and measured double T_2 cut-offs: (a) T_{2cr} and (b) T_{2cf}.

$$f(r) = cr^{-1-D}, \tag{19}$$

where c is constant. It can be concluded from equation (19) that the fractal dimension of artificial clayey soil decreases with increasing uniformity of the pore distribution. This indicates that the uniformity of artificial clayey soil with higher clay content is higher. For artificial clayey soil with the same clay content, the uniformity of the M series was worse than that of the K series.

The relationships between the double T_2 cut-offs and fractal dimensions are shown in Figure 11. As shown in Figure 11(a), the relationships between the double T_2 cut-offs and fractal dimensions of artificial clayey soil in the M-group can be expressed by the following equations:

$$T_{2cr-m} = 2.150\,D - 4.916, \tag{20}$$

$$T_{2cf-m} = 9.511\,D - 22.099. \tag{21}$$

As presented in Figure 11(b), the relationships between the double T_2 cut-offs and fractal dimensions of artificial clayey soil in the K-group can be expressed by the following equations:

$$T_{2cr-k} = 7.086\,D - 12.984, \tag{22}$$

$$T_{2cf-k} = 5.089\,D - 6.339. \tag{23}$$

The predicted double T_2 cut-offs of artificial clayey soil can be calculated by equations (20)–(23). A comparison between the predicted and measured double T_2 cut-offs is presented in Figure 12. The points in Figures 12(a) and 12(b) are very close to the line $y = x$; this indicates that the error between the predicted and measured double T_2 cut-offs is small.

The R^2, MAE, and RMSE values were also determined to evaluate the prediction accuracy of equations (20)–(23), and these values for the predictive equations are shown in

TABLE 6: The R^2, MAE, and RMSE values of the predictive equations for the double T_2 cut-offs.

Double T_2 cut-offs	R^2	MAE	RMSE
T_{2cr}	0.998	0.0476	0.0753
T_{2cf}	0.998	0.0687	0.0835

Table 6. From Figure 12 and Table 6, it can be seen that the prediction capability of the predictive equations for the double T_2 cut-offs is sufficient.

4. Conclusions

Evaporation and NMR tests were carried out on eight artificial clayey soils with different mineral compositions. On the basis of the results of tests and a discussion, the main conclusions are as follows:

(1) The T_2 total signal amplitude is proportional to the weight of distilled water in artificial clayey soil. During the evaporation process, the T_2 total signal amplitude decreased until it was stable. The decay rate of the T_2 total signal amplitude was constant at first and then decreased gradually to zero. Based on the different decay rates, the evaporation process can be divided into three stages: the constant rate stage, the falling rate stage, and the residual stage.

(2) Based on the three stages of the evaporation process, the water in artificial clayey soil can be classified into three categories: absolute movable water, partially movable water, and immovable water. Double T_2 cut-offs were also defined to distinguish the cumulative signal amplitudes in the T_2 spectrum corresponding to the different kinds of water.

(3) An improved TC model for predicting the permeability coefficient of artificial clayey soil was proposed. The improved and typical models were

evaluated by determining their R^2, MAE, and RMSE values. The prediction accuracy of the improved model is much higher than that of the typical one.

(4) To simplify the prediction process, the relationships between the double T_2 cut-offs and the fractal dimension of the T_2 spectrum of saturated clayey soil were also established.

Data Availability

The data used to support the findings of this study have not been made available because the data also form part of an ongoing study (National Key Research and Development Program of China).

Conflicts of Interest

The authors declare no conflicts of interest.

Acknowledgments

References

[1] Y. Deng, Z. Wu, Y. Cui, S. Liu, and Q. Wang, "Sand fraction effect on hydro-mechanical behavior of sand-clay mixture," *Applied Clay Science*, vol. 135, pp. 355–361, 2017.

[2] Q. A. Al Rashid, H. M. Abuel-Naga, E.-C. Leong, Y. Lu, and H. Al Abadi, "Experimental-artificial intelligence approach for characterizing electrical resistivity of partially saturated clay liners," *Applied Clay Science*, vol. 156, pp. 1–10, 2018.

[3] T. Kozlowski and A. Ludynia, "Permeability coefficient of low permeable soils as a single-variable function of soil parameter," *Water*, vol. 11, no. 12, p. 20, 2019.

[4] L. L. Zeng, Z. S. Hong, Y. Q. Cai, and J. Han, "Change of hydraulic conductivity during compression of undisturbed and remolded clays," *Applied Clay Science*, vol. 51, no. 1-2, pp. 86–93, 2011.

[5] G. Mesri and R. E. Olson, "Mechanisms controlling the permeability of clays," *Clays and Clay Minerals*, vol. 19, no. 3, pp. 151–158, 1971.

[6] A. M. Samarasinghe, Y. Huang, and V. Drnevich, "Permeability and consolidation of normally consolidated soils," *Journal of the Geotechnical Engineering Division*, vol. 108, no. 6, pp. 835–850, 1982.

[7] B. Dolinar, "Predicting the hydraulic conductivity of saturated clays using plasticity-value correlations," *Applied Clay Science*, vol. 45, no. 1-2, pp. 90–94, 2009.

[8] G. Achari and R. Joshi, "A reexamination of the permeability index of clays: discussion," *Canadian Geotechnical Journal*, vol. 31, no. 1, pp. 140-141, 2011.

[9] K. Yamada, Y. Watabe, and K. Saitoh, "Hydraulic conductivity and compressibility of mixtures of nagoya clay with sand or bbntonite," *Geotechnique (UK)*, vol. 61, no. 3, pp. 211–219, 2011.

[10] A. A. Behroozmand, K. Keating, and E. Auken, "A review of the principles and applications of the NMR technique for near-surface characterization," *Surveys in Geophysics*, vol. 36, no. 1, pp. 27–85, 2014.

[11] B. Kong, F. Xia, B. Yu, T. Xia, and Z. Ding, "Pore size changes in marine soft soil under various freezing conditions," *Journal of Marine Science and Engineering*, vol. 8, no. 3, p. 170, 2020.

[12] Z. Liu, D. Liu, Y. Cai, Y. Yao, Z. Pan, and Y. Zhou, "Application of nuclear magnetic resonance (NMR) in coalbed methane and shale reservoirs: a review," *International Journal of Coal Geology*, vol. 218, Article ID 103261, 2020.

[13] Y. Sun, C. Zhai, J. Z. Xu, Y. Z. Cong, L. Qin, and C. Zhao, "Characterisation and evolution of the full size range of pores and fractures in rocks under freeze-thaw conditions using nuclear magnetic resonance and three-dimensional X-ray microscopy," *Engineering Geology*, vol. 271, p. 14, 2020.

[14] Y. Yao, D. Liu, J. Liu, and S. Xie, "Assessing the water migration and permeability of large intact bituminous and anthracite coals using NMR relaxation spectrometry," *Transport in Porous Media*, vol. 107, no. 2, pp. 527–542, 2015.

[15] A. Li, W. Ding, R. Wang et al., "Petrophysical characterization of shale reservoir based on nuclear magnetic resonance (NMR) experiment: a case study of lower cambrian Qiongzhusi formation in eastern Yunnan province, South China," *Journal of Natural Gas Science and Engineering*, vol. 37, pp. 29–38, 2017.

[16] R. Rezaee, A. Saeedi, and B. Clennell, "Tight gas sands permeability estimation from mercury injection capillary pressure and nuclear magnetic resonance data," *Journal of Petroleum Science and Engineering*, vol. 88-89, pp. 92–99, 2012.

[17] Z. Lu, A. Sha, and W. Wang, "Permeability evaluation of clay-quartz mixtures based on low-field NMR and fractal analysis," *Applied Sciences*, vol. 10, no. 5, p. 1585, 2020.

[18] S. Haber-Pohlmeier, S. Stapf, and A. Pohlmeier, "NMR fast field cycling relaxometry of unsaturated soils," *Applied Magnetic Resonance*, vol. 45, no. 10, pp. 1099–1115, 2014.

[19] C. Buchmann, M. Meyer, and G. E. Schaumann, "Characterization of wet aggregate stability of soils by H-NMR relaxometry," *Magnetic Resonance in Chemistry*, vol. 53, no. 9, pp. 694–703, 2015.

[20] M. Meyer, C. Buchmann, and G. E. Schaumann, "Determination of quantitative pore-size distribution of soils with 1H NMR relaxometry," *European Journal of Soil Science*, vol. 69, no. 3, pp. 393–406, 2018.

[21] H. Tian, C. Wei, H. Wei, and J. Zhou, "Freezing and thawing characteristics of frozen soils: bound water content and hysteresis phenomenon," *Cold Regions Science and Technology*, vol. 103, pp. 74–81, 2014.

[22] L. R. Stingaciu, A. Pohlmeier, P. Blümler et al., "Characterization of unsaturated porous media by high-field and low-field NMR relaxometry," *Water Resources Research*, vol. 45, no. 8, p. 8412, 2009.

[23] F. Jaeger, S. Bowe, H. Van As, and G. E. Schaumann, "Evaluation of 1 H NMR relaxometry for the assessment of pore-size distribution in soil samples," *European Journal of Soil Science*, vol. 60, no. 6, pp. 1052–1064, 2009.

[24] K. Keating and S. Falzone, "Relating nuclear magnetic resonance relaxation time distributions to void-size distributions for unconsolidated sand packs," *Geophysics*, vol. 78, no. 6, pp. D461–D472, 2013.

[25] H. Tian, C. Wei, and L. Tan, "Effect of freezing-thawing cycles on the microstructure of soils: a two-dimensional NMR relaxation analysis," *Cold Regions Science and Technology*, vol. 158, pp. 106–116, 2019.

[26] L. Kong, H. M. Sayem, and H. Tian, "Influence of drying-wetting cycles on soil-water characteristic curve of undisturbed granite residual soils and microstructure mechanism

by nuclear magnetic resonance (NMR) spin-spin relaxation time (T_2) relaxometry," *Canadian Geotechnical Journal*, vol. 55, no. 2, pp. 208–216, 2018.

[27] Y.-T. Huang, Z.-Y. Hseu, and H.-C. Hsi, "Influences of thermal decontamination on mercury removal, soil properties, and repartitioning of coexisting heavy metals," *Chemosphere*, vol. 84, no. 9, pp. 1244–1249, 2011.

[28] Y. Wang, S. Lu, T. Ren, and B. Li, "Bound water content of air-dry soils measured by thermal analysis," *Soil Science Society of America Journal*, vol. 75, no. 2, pp. 481–487, 2011.

[29] J. Kucerik, D. Tokarski, M. S. Demyan, I. Merbach, and C. Siewert, "Linking soil organic matter thermal stability with contents of clay, bound water, organic carbon and nitrogen," *Geoderma*, vol. 316, pp. 38–46, 2018.

[30] S. Li, C. Wang, X. Zhang, L. Zou, and Z. Dai, "Classification and characterization of bound water in marine mucky silty clay," *Journal of Soils and Sediments*, vol. 19, no. 5, pp. 2509–2519, 2019.

[31] I. Menapace, E. Masad, G. Papavassiliou, and E. Kassem, "Evaluation of ageing in asphalt cores using low-field nuclear magnetic resonance," *International Journal of Pavement Engineering*, vol. 17, no. 10, pp. 847–860, 2016.

[32] L. R. Stingaciu, L. Weihermüller, S. Haber-Pohlmeier, S. Stapf, H. Vereecken, and A. Pohlmeier, "Determination of pore size distribution and hydraulic properties using nuclear magnetic resonance relaxometry: a comparative study of laboratory methods," *Water Resources Research*, vol. 46, no. 11, 2010.

[33] Y.-Q. Song, L. Venkataramanan, M. D. Hürlimann, M. Flaum, P. Frulla, and C. Straley, "T_1-T_2 correlation spectra obtained using a fast two-dimensional Laplace inversion," *Journal of Magnetic Resonance*, vol. 154, no. 2, pp. 261–268, 2002.

[34] K. A. Dines and R. J. Lytle, "Computerized geophysical tomography," *Proceedings of the IEEE*, vol. 67, no. 7, pp. 1065–1073, 1979.

[35] M. N. Testamanti and R. Rezaee, "Determination of NMR T_2 cut-off for clay bound water in shales: a case study of Carynginia formation, Perth Basin, Western Australia," *Journal of Petroleum Science and Engineering*, vol. 149, pp. 497–503, 2017.

[36] C. S. Tang, B. Shi, C. Liu, W. B. Suo, and L. Gao, "Experimental characterization of shrinkage and desiccation cracking in thin clay layer," *Applied Clay Science*, vol. 52, no. 1-2, pp. 69–77, 2011.

[37] W. Jiang, D. Yuan, J. Shan, W. Ye, H. Lu, and A. Sha, "Experimental study of the performance of porous ultra-thin asphalt overlay," *International Journal of Pavement Engineering*, pp. 1–13, 2020.

[38] G. Tao and J. Zhang, "Two categories of fractal models of rock and soil expressing volume and size-distribution of pores and grains," *Science Bulletin*, vol. 54, no. 23, pp. 4458–4467, 2009.

[39] G. L. Tao, Y. Chen, L. W. Kong, H. L. Xiao, Q. S. Chen, and Y. X. Xia, "A simple fractal-based model for soil-water characteristic curves incorporating effects of initial void ratios," *Energies*, vol. 11, no. 6, p. 20, 2018.

Research Article

Sorptive Removal of Color Dye Safranin O by Fibrous Clay Minerals and Zeolites

Ben Sieren,[1] Jessica Baker,[1] Xisen Wang,[2] Samuel J. Rozzoni,[2] Kristen Carlson,[1] Alyssa McBain,[1] Daniel Kerstan,[1] Lori Allen,[2] Libing Liao ⓘ,[3] and Zhaohui Li ⓘ[1]

[1]*Department of Geosciences, University of Wisconsin–Parkside, 900 Wood Road, Kenosha, WI 53144, USA*
[2]*Department of Chemistry, University of Wisconsin–Parkside, 900 Wood Road, Kenosha, WI 53144, USA*
[3]*Beijing Key Laboratory of Materials Utilization of Nonmetallic Minerals and Solid Wastes,*
National Laboratory of Mineral Materials, School of Materials Science and Technology, China University of Geosciences, Beijing,
29 Xueyuan Road, Beijing 100083, China

Correspondence should be addressed to Libing Liao; lbliao@cugb.edu.cn and Zhaohui Li; li@uwp.edu

Academic Editor: Matjaz Valant

The increased use of color dyes in industry imposes a great threat to the environment. As such, developing cost-effective techniques for dye removal from wastewater attracted great attention. Earth materials, particularly those with large specific surface area (SSA) and high cation exchange capacity (CEC), were evaluated for their potential use for wastewater treatment. In this study, palygorskite, sepiolite, and clinoptilolite were evaluated for their removal of cationic dyes using safranin O (SO$^+$) as a model compound. The CEC values of the materials played a key role in SO$^+$ removal while other physicochemical conditions, such as temperature, equilibrium solution pH, and ionic strength, had less influence on SO$^+$ removal. Sorbed SO$^+$ cations were limited to the external surfaces of the minerals, as their channel sizes are less than the size of SO$^+$ cation. Molecular dynamic simulations showed dense monolayer SO$^+$ uptake on palygorskite due to its relatively large CEC value. In contrast, loosely packed monomer SO$^+$ uptake was adopted on sepiolite for its large SSA and low CEC. Dense multilayers or admicelles of SO$^+$ formed on zeolite surfaces. As such, for the best SO removal, palygorskite is better than sepiolite, though both are fibrous clay minerals.

1. Introduction

Pigments and dyes are widely used in different types of industries including textile and leather dyeing, paper, printing, pharmaceutical, and cosmetics [1]. As such, large-scale production and widespread applications resulted in many synthetic organic dyes to permeate into different compartments of water and soil bodies [2]. To prevent direct discharges of waters containing different types, amounts, and toxicities of dyes that threaten the environment, numerous studies were conducted recently to treat the dye-containing water [3]. However, as there are more than 10,000 types of dyes used and each may have different physicochemical properties [4], and different approaches were undertaken for dye removal including physical [3], chemical [4], and biological [5], effective methods for removal of a particular dye might be limited. In addition, most of the studies were focused on developing new materials, mostly nanomaterials [3, 6], due to their large specific surface area (SSA) and high reactivity. However, high material costs may limit their immediate practical values.

Earth materials have long been used to sorb color dyes for painting purposes. A typical example is Maya blue, a mixture of indigo dyes with palygorskite, used to color sculpture, artwork, and textiles around the Aztec area in Mexico over 1200 years. Due to the skyrocketing use of color dyes and inexpensive material cost, earth material was studied extensively for the removal of color dyes, most of them were of cationic and zwitterionic in nature, from solution because of large SSA and high cation exchange capacity (CEC) of many phyllo- and tectosilicates, such as different types of clay minerals and zeolites.

Safranin O (SO), also called Basic Red 2, Cotton Red, Gossypimine, Safranin T, and Safranin Y or A, is a water-soluble reddish-brown powder [7], commonly used in tracer and biological laboratory purposes [8]. As such, methods tested for its removal from water include physicochemical, biological, and chemical methods [9].

Studies on SO removal by clay minerals were limited. Montmorillonite (MMT), due to its high CEC and SSA values, could sorb SO to a capacity of 380 mg/g or 1.1 mmol/g [10]. In a different study, SO removal capacity by bentonite collected from Khulais, Saudi Arabia, was 294 mg/g or 1.1 mmol/g [11], but neither the CEC value of the clay nor the mechanism of SO removal was discussed. An SO removal capacity of 24 mg/g or 68 mmol/kg was reported for a Saudi Arabia natural clay [8]; however, the major components of the clay were quartz, chamosite, albite, dickite, and microcline as determined by X-ray diffraction analyses, and the mechanism of SO removal was not mentioned.

SO sorption capacity on kaolinite was up to 16 mg/g or 45 mmol/kg as reported in one study [12]. On a different kaolinite, SO sorption capacity as high as 160 mmol/kg was also reported, and the relatively hydrophobic silica face of kaolinite contributed more to the SO sorption and aggregation [13]. SO sorption on a raw ferruginous kaolinite was up to 59.3 mg/g or 168 mmol/kg and was attributed to physical behavior, heterogeneous nature, and multilayer formation [14].

Palygorskite (PAL) and sepiolite (SEP) are fibrous phyllosilicates. Both have channels running parallel to the fiber length with channel sizes of 0.37 by 0.64 nm for SEP and 0.37 by 1.06 nm for SEP that are accessible by inorganic cations [15]. Thus, not only the surfaces but also the channel area is responsible for cation exchanges and specific sorption of cations. In one study, an SO sorption capacity of 200 mg/g was found on a natural Iraqi PAL, but the CEC value of the PAL was not reported [16]. No studies of SO sorption on natural sepiolite were reported, but an SO sorption capacity of 18.48 mg/g was reported on iron oxide/sepiolite magnetite composite (MSep) [17].

Zeolite is a group of minerals in tectosilicates with abundant resources, available globally, and has already found many applications because of its high CEC and SSA [18]. A clinoptilolite zeolite (CZ) was studied for the sorption and release of photodynamically active dyes hypericin (Hyp), methylene blue (MB), chlorin e6, Al-phthalocyanine, and fluorescein under multiphoton microscopy, and the results suggested even distribution of the dyes on the surface of CZ with the potential release of Hyp from CZ surfaces in the presence of biomolecules, indicating that CZ could serve as an effective material for drug delivery and controlled release in biological systems [19]. Sorption of SO on CZ showed a capacity of 0.08 mg/g, and the sorption increased with initial solution pH [20], but the mechanism was not discussed. In a different study, even for the CZ modified by iron oxide nanoparticles, the MB sorption capacity was still at 52 mg/g, corresponding to 170 mmol/kg, and again, the mechanism of MB removal was not discussed [21]. Sorption of SO on a CZ from Yemen resulted in a capacity of 43 mg/g or 120 mmol/kg, and the SO uptake on ZEO was attributed to cation exchange and chemisorption [22]. On the opposite, after acid modification, the uptake of a color dye Red 24 on a CZ was only 0.9 mmol/kg [23]. A magnetic zeolite NaA achieved an SO removal capacity of 149 mg/g or 425 mmol/kg after sodium dodecyl sulfate (SDS) modification [18], while the purpose of SDS coating was not mentioned, nor noncoating zeolite as controls was compared.

This study aims to use the selected phyllo- and tecto-silicates with open channels to assess their SO removal from water under different physicochemical conditions and to correlate changes in material properties of the sorbents after SO uptake as characterized by different instruments. In addition, the interactions between SO and the minerals were simulated by molecular dynamic simulations. The configuration of sorbed SO^+ cations on the mineral surfaces was derived from the sorption study and instrumental analyses in conjunction with the simulation. Then, the SO removal mechanism by the minerals was proposed.

2. Materials and Methods

2.1. Materials. The SO used is in a chloride form (CAS number of 477-73-6, $M = 350.84$ g/mol). Literature values are 50 g/L for solubility [24] and 11 for pKa [13]. Molecular sizewise, it is 1.16 nm long by 0.96 nm wide by 0.4 nm thick, as determined by a molecular editor Avogadro (https://avogadro.cc/) (Figure 1).

The minerals used include fibrous phyllosilicates palygorskite (PAL) and sepiolite (SEP) and tectosilicate zeolite (ZEO), all with channel structures where sorption of inorganic cations is attainable. The PAL used is PFl-1, and the SEP used is SepSp-1. Both were reference clays obtained from the Source Clay Minerals Repository. The ZEO used is clinoptilolite obtained from the St. Cloud Mine in Winston, NM. The CEC values are 175 [25] and 15 [26] meq/kg, for PFl-1 and SpeSp-1, respectively, while their SSA values are 173 [27] and 250 m²/g [26]. For ZEO, the external CEC (ECEC) is 90 meq/kg and the SSA is 15.7 m²/g [28].

2.2. SO Uptake. For SO removal by PAL and ZEO, 0.25 g of solid and 10 mL of SO solution were added to each 50 mL centrifuge tube. For SEP, 0.5 g of solid and 10 mL of solution were used due to its lower CEC value. The initial concentrations for the isotherm study varied from 0.3 to 2.5 mM for ZEO and SPE and up to 5 mM for PAL, and the mixtures were shaken on a reciprocal shaker at 150 rpm and room temperature ($23 \pm 1°C$) for 24 h. For the kinetic study, mixing lasted from 0.1 to 24 h. To investigate the influence of solution pH on SO removal, the equilibrium pH was adjusted multiple times during the 24 h period to achieve final values between 3 and 11 with an interval close to 1. For the influence of solution ionic strength on SO removal, the SO solution was made with 0.001, 0.01, 0.1, and 1.0 M of NaCl instead of DI water. The influence of temperature on SO removal was tested at 23, 33, 43, and 53°C with a deviation of less than 1°C. In all these studies, the initial SO concentrations were fixed at 4.5, 2.0, and 1.0 mM for PAL, ZEO, and

(a)   (b)
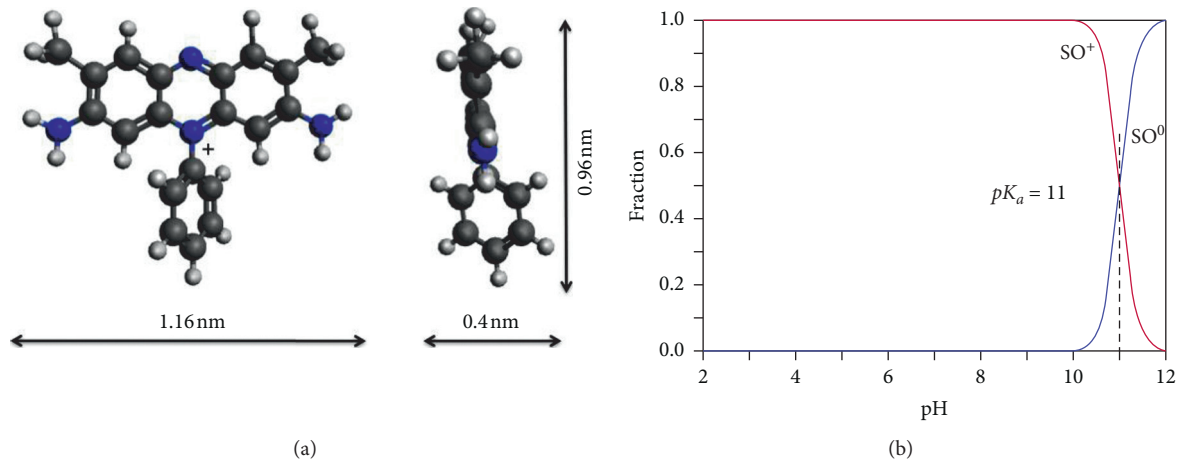
FIGURE 1: Molecular structure of SO viewed from different directions (a) and its pH speciation (b).

SEP, respectively, and shaken for 24 h. After mixing, samples were centrifuged at 3500 rpm for 10 min and the supernatants passed through 0.45 μm syringe filters before being analyzed for equilibrium SO concentrations using a UV-Vis method. The amount of SO sorbed was determined by the difference between the initial and equilibrium SO concentrations. Duplicates were tested for each experimental condition.

2.3. Instrumental Analyses. The equilibrium SO concentrations were determined by a UV-Vis spectrophotometer. The wavelength used was 516 nm [29, 30]. To assess the counterion Cl$^-$concentration in solution, an ion chromatography (IC) with a PRP-100 anion exchange column was used. Calibration was made using SO concentrations of 0.1 to 5 mM with an r^2 of 0.999.

A Shimadzu 6100 X-ray diffractometer was used for X-ray diffraction (XRD) analyses of the samples after sorption experiments. A Ni-filtered CuKα radiation at 30 kV and 40 mA and a scanning speed of 2°min were set for the experimental conditions, and the samples were scanned from 5 to 40° (2θ). The FTIR spectra were acquired on a Shimadzu IRAffinity-1S FTIR spectrometer equipped with a quartz attenuated total reflection device from 400 to 4000 cm^{-1} with a resolution of 4 cm^{-1}.

2.4. Molecular Dynamic Simulation. The molecular dynamic simulation was performed using the FORCITE module in Materials Studio 6.0 software to determine the surface configurations of sorbed SO$^+$ cations on different surfaces of the minerals. The number of SO$^+$ cations used for the simulation was based on the SSA of the minerals and the SO sorption capacity on each mineral. The unit cell parameters used were as follows: $a = 12.78$ Å, $b = 17.86$ Å, $c = 5.24$ Å, $\beta = 95.78°$, and $Z = 4$ for PAL; $a = 13.43$ Å, $b = 26.88$ Å, $c = 5.281$ Å, and $Z = 4$ for SEP; and $a = 17.688$ Å, $b = 17.902$ Å, $c = 7.409$ Å, $\beta = 116.5°$, and $Z = 4$ for ZEO. Also, the supercells were made of 2bx4c for PAL and SEP due to their

layered structure and 2bx4c, 2ax4c, and 2ax1.5b for ZEO due to its 3D structure. The constructed model was optimized geometrically.

3. Results and Discussion

3.1. Kinetics of SO Removal. SO removal by these minerals was relatively fast, and equilibrium could be reached within an hour for PAL and SEP (Figure 2(a)). In contrast, it may take up to 8 h to reach equilibrium for ZEO. This could be due to its larger particle size, and thus, longer diffusion time is needed to reach equilibrium. Similarly, uptake of SO on CMC-41 was thought as diffusion controlled [7]. The results were fitted to several kinetic models, and the pseudo-second-order kinetics fitted the data best. It has the following form:

$$q_t = \frac{kq_e^2 t}{1 + kq_e t},\tag{1}$$

that can be rearranged into a linear form as follows:

$$\frac{t}{q_t} = \frac{1}{kq_e^2} + \frac{1}{q_e}t,\tag{2}$$

where k (kg/mmol-h) and kq_e^2 (mmol/kg-h) are the rate constant and initial rate of SO removal by the minerals, while q_t and q_e (mmol/kg) are the amount of SO uptake at time t and at equilibrium. The initial rates and the rate constants are 1379, 213, and 23256 mmol/kg-h and 3.5, 0.04, and 0.7 kg/mmol-h for SO uptake on SEP, ZEO, and PAL, respectively. Meanwhile, calculated q_e values were 20, 76, and 180 mmol/kg for SO uptake on SEP, ZEO, and PAL, respectively, with the coefficients of determination r^2 all greater than 0.999 (inset of Figure 2(a)). The very high rate, large rate constant, and larger q_e for SO uptake on PAL correlated to its larger CEC and SSA values well. In comparison, the slow SO removal by ZEO confirmed the speculation that diffusion played an important role. In a previous study, SO sorption on MSep followed the pseudo-second-order kinetics with a k of 0.19 g/mg-min [17].

(a)

(b)
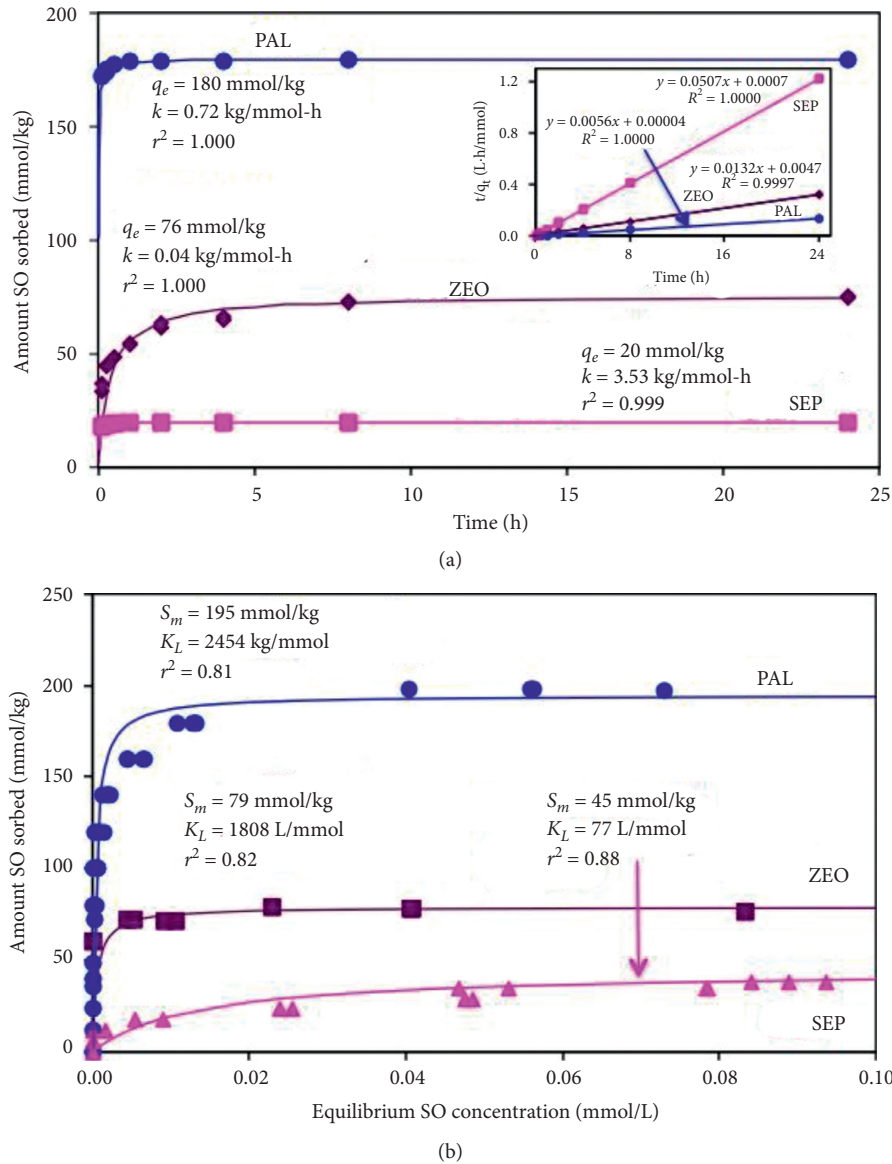
FIGURE 2: Kinetics (a) and isotherm (b) of SO sorption on PAL, ZEO, and SEP. The lines are pseudo-second-order (a) and Langmuir (b) fits the experimental data. Inset in (a) is linearized fit to the pseudo-second-order kinetics.

3.2. Isotherms of SO Uptake. Uptake of SO by the tested minerals is illustrated in Figure 2(b). Results were fitted to both the Freundlich and Langmuir models, and the latter had a better fit. The Langmuir isotherm has the following form:

$$C_s = \frac{K_L S_m C_L}{1 + K_L C_L}, \tag{3}$$

that can be converted into a linear form as follows:

$$\frac{C_L}{C_s} = \frac{1}{K_L S_m} + \frac{C_L}{S_m}, \tag{4}$$

where C_L and C_S are the equilibrium SO concentration in solution (mmol/L) and amount of SO sorbed on solid (mmol/kg), while S_m (mmol/kg) and K_L (L/mmol) are the Langmuir parameters corresponding to the SO sorption

capacity and SO affinity for the minerals. The fitted results are S_m = 195, 79, and 45 mmol/kg and K_L = 2450, 1808, and 77 L/mmol for SO sorption on PAL, ZEO, and SPE, respectively. The CEC values of PFL and SEP are 175 [25] and 15 [26] meq/kg. For ZEO, the ECEC value is 90 meq/kg [28].

A previous study showed an SO sorption capacity of 200 mg/g or 570 mmol/kg on PAL [16]. Sorption of MB on a PAL showed a capacity of 200 mmol/kg [31]. However, the CEC and SSA values and the purity of the mineral in these studies were not provided. Moreover, the data in their isotherm study only showed a capacity slightly over 100 mg/g or about 300 mmol/kg [16]. SO sorption on MSep also followed the Langmuir isotherm with a sorption capacity of 18.48 mg/g [17]. In a previous study, the SO uptake on CZ was 43 mg/g or 120 mmol/kg and was attributed to cation exchange and chemisorption [22]. The SO sorption on a synthetic ZEO was only 9.4 mg/g [32]. On a different type of

ZEO, the SO sorption only reached a capacity of 1.3 mg/g [33]. Even lower, sorption of SO on CZ was fitted to the Langmuir isotherm with a capacity of 0.055 mg/g, corresponding to only 0.155 mmol/kg [20], in comparison with 79 mmol/kg in this study (Figure 2(b)).

As the SO used is SO^+Cl^-, the equilibrium counterion Cl^- concentrations at the SO sorption capacity were about 30% lower than their initial concentrations as measured by ion chromatography, suggesting that some of the SO removal from solution was in a dimeric form balanced by counterion Cl^- bridging the two cations. An increase in dimer concentration was associated with increased SO concentration [34].

For CZ, there are three channels of which two channels are running parallel to each other and to the *c*-axis with a channel consisting of a 10-member ring of a size of 0.44–0.72 nm and another channel consisting of an 8-member ring of a size of 0.41–0.47 nm, while the third channel is parallel to *a*-axis and made of an 8-member ring of a size of 0.40–0.55 nm [35]. As the size of SO is greater than the channel size of the three channels, the uptake of SO is limited to the external surfaces of ZEO. Taking consideration of the limited SSA, the uptake of SO may form a multilayer sorption on ZEO.

3.3. Influence of Solution pH, Ionic Strength, and Temperature on SO Uptake.

Essentially, equilibrium solution pH had minimal influence of SO uptake on these minerals (Figure 3(a)). A similar pH effect on SO removal by PAL was reported earlier [16]. As the initial solution pH increased from 2 to 10, the amount of SO sorption on CZ increased from 3.5 to 7 mg/g [20]. Similarly, the SO uptake on ZEO increased from 30 to 60% as the initial solution pH increased from 2 to 10 [33]. A slight increase in SO removal from 82 to 95% was observed for a Yemen CZ [22]. With a pK_a value of 11, SO is in a cationic form when equilibrium solution pH is <11. The negligible pH influences on SO^+ uptake indicated that organic cations have a higher affinity for negatively charged mineral surfaces in comparison with inorganic cations.

Similar to equilibrium solution pH, solution ionic strength also had a minimal influence of SO uptake (Figure 3(b)). A previous study showed that added NaCl, $CaCl_2$, Na_2SO_4, and NH_4Cl in the range of 0–10% (w/v) also had minimal influence on SO uptake on modified zeolite [18]. The results suggested again that the organic cation had higher affinity for the negatively charged mineral surfaces in comparison with inorganic cations.

Influence of equilibrium temperature on SO uptake revealed exothermic processes for SO removal using PAL, ZEO, and SEP (Figure 3(c)). The thermodynamic parameters of SO removal can be related to the SO distribution coefficient K_d, the ratio of SO sorbed on solids to the equilibrium SO concentration in solution, by

$$\ln K_d = -\frac{\Delta H}{RT} + \frac{\Delta S}{R}, \tag{5}$$

where the ΔH and ΔS are the changes in enthalpy and entropy after SO uptake, R is the gas constant, and T is the temperature in K. The ΔH and ΔS values are related to the free energy ΔG of SO uptake by

$$\Delta G = \Delta H - T\Delta S. \tag{6}$$

The thermodynamic parameters of SO calculated from equations (5) and (6) showed small $\Delta S°$ values, moderate negative $\Delta H°$, and $\Delta G°$ values in the ranges of −14 to −24 kJ/mol (Table 1), indicating net attractive interactions via physical sorption or electrostatic interactions between the solute and sorbents. The $\Delta G°$ value was about −15 kJ/mol for SO uptake on MSep, suggesting physisorption [17].

3.4. XRD Analyses.

The SO used is crystalline as revealed by the XRD analysis (Figure 4 inset). None of the SO peaks showed up in the XRD patterns of the three minerals after uptake of different amounts of SO, confirming that the SO uptake from solution was via sorption instead of precipitation. Meanwhile, the *d*-spacings of the minerals did not change after SO uptake, indicating the location of sorbed SO^+ cations was limited to the external surfaces, although all three minerals have channel structures where the sites for the uptake of inorganic cations are available (Figure 4).

3.5. FTIR Analyses.

The full FTIR spectra of the three minerals together with the crystalline SO are displayed in Figure 5. For SO, the broad absorption bands at 3338 and 3183 cm^{-1} were assigned to the −OH and −NH$_2$ groups and to the N–H group [36]. However, in this study, they are located at 3313 and 3140 cm^{-1} (Figure 5). In a different study, bands at 1641 and 1610 cm^{-1} were assigned to the aromatic ring stretching vibration, 1493 cm^{-1} to the −CH$_3$ stretching vibration, and 1334 cm^{-1} to the aromatic C = N stretching vibration [37]. These bands were located at 1639, 1609, 1485, and 1323 cm^{-1} in this study (Figure 5). Meanwhile, the C = N stretching vibration band was located at 1320 cm^{-1} [38].

These bands did not show up after SO uptake on PAL from the initial SO concentration of 0.9 mM, corresponding to an SO uptake of 36 mmol/kg, except the one at 1323 cm^{-1}. At an initial concentration of 2.0 mM, corresponding to an SO uptake of 80 mmol/kg, the bands at 1485 and 1528 cm^{-1} started to appear and shifted to 1489 and 1533 cm^{-1}. Meanwhile, the band at 1323 cm^{-1} shifted to 1337 cm^{-1} (Figure 6(a)). At the SO sorption capacity of 198 mmol/kg, the bands remained at the same location (no further band shift was observed), but their intensities increased accordingly. For SEP, the only band showed up was the one at 1323 cm^{-1}, even at the highest SO input concentration of 2.5 mM, corresponding to an SO uptake of 43 mmol/kg, and the band shifted to 1331 cm^{-1} after SO uptake on SEP (Figure 6(b)). For ZEO, the 1323 cm^{-1} band showed up at an initial concentration of 0.9 mM, corresponding to an SO uptake of 36 mmol/kg, and the bands at 1323, 1485, 1533, and 1609 cm^{-1} all appeared at the SO initial concentration of 1.5 mM, corresponding to an SO uptake of 60 mmol/kg, and

(a)

(b)

(c)
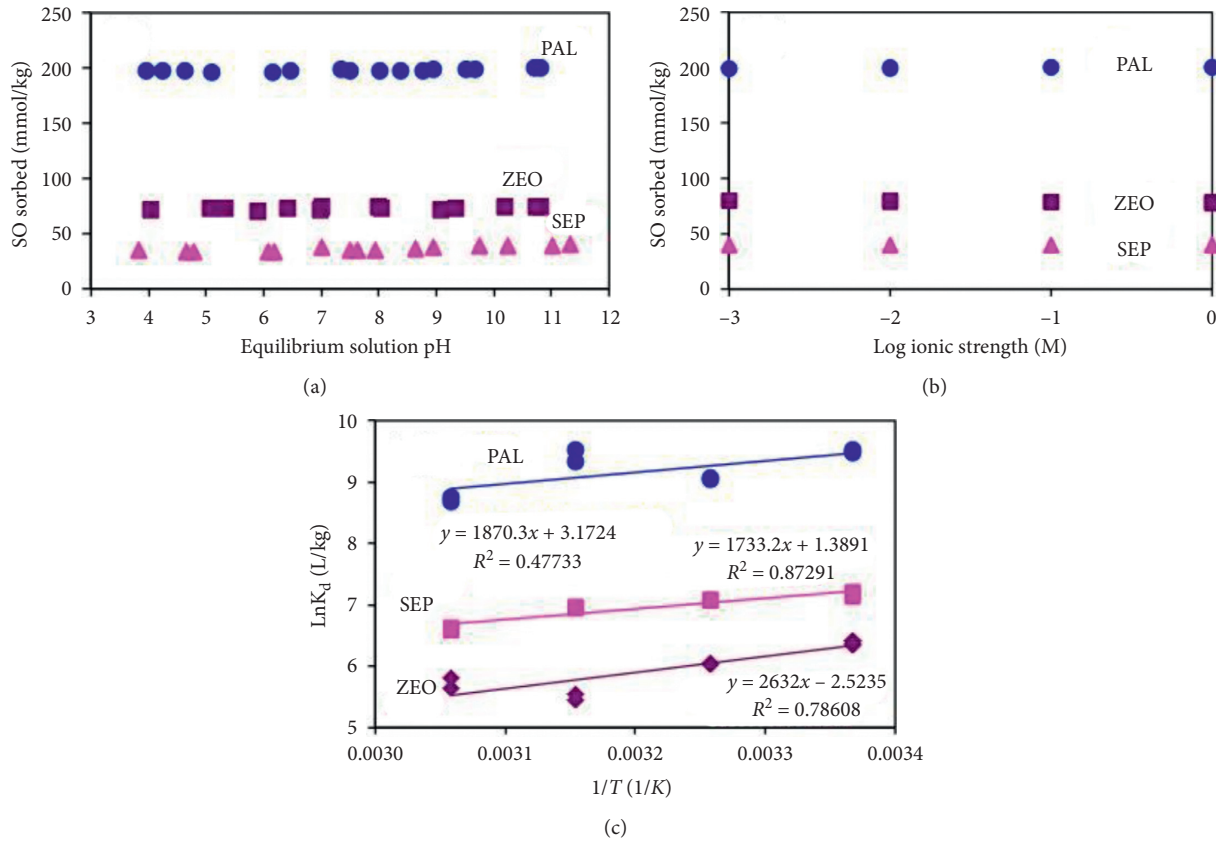
Figure 3: Influence of equilibrium solution pH (a), ionic strength (b), and temperature (c) on SO sorption on PAL, ZEO, and SEP.

Table 1: Thermodynamics of SO uptake on PAL, ZEO, and SEP.

Minerals	$\Delta G°$ (kJ/mol)				$\Delta H°$ (kJ/mol)	$\Delta S°$ (kJ/mol-K)
	296 K	306 K	316 K	326 K		
ZEO	−15.7	−15.5	−15.3	−15.0	−21.9	−0.02
SEP	−17.8	−17.9	−18.1	−18.2	−14.4	0.01
PAL	−23.4	−23.6	−23.9	−24.1	−15.6	0.03

(a)
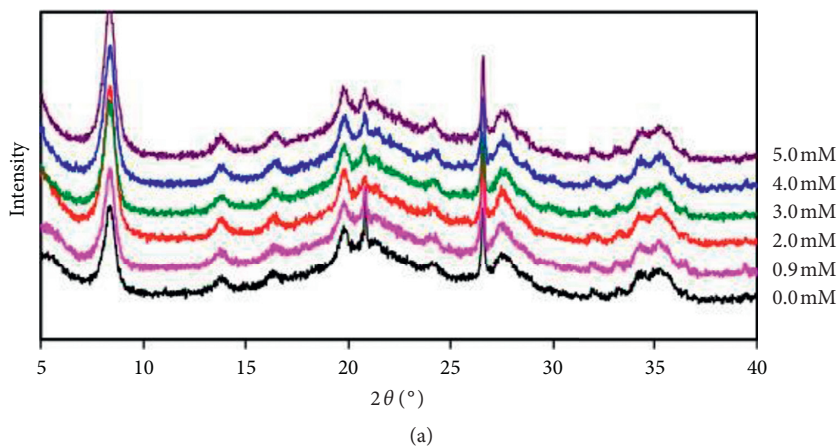
Figure 4: Continued.

(b)

(c)
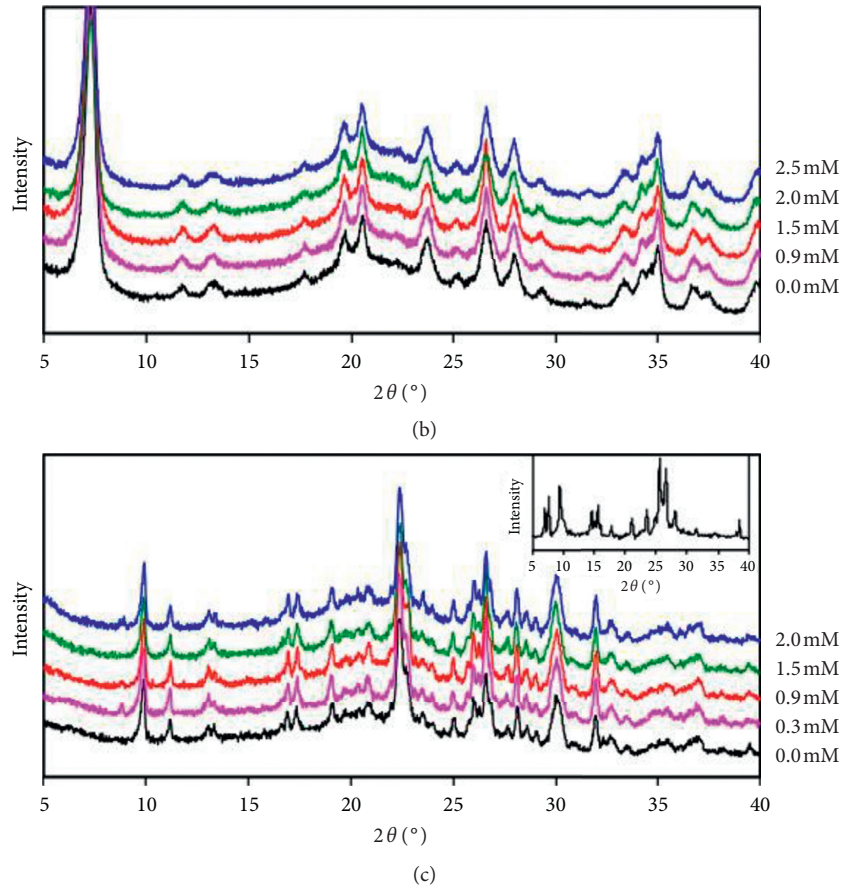
Figure 4: XRD patterns of PAL (a), SEP (b), and ZEO (c) after SO uptake from different initial SO concentrations. The inset in (c) is the XRD pattern of crystalline SO.

(a)

(b)

(c)
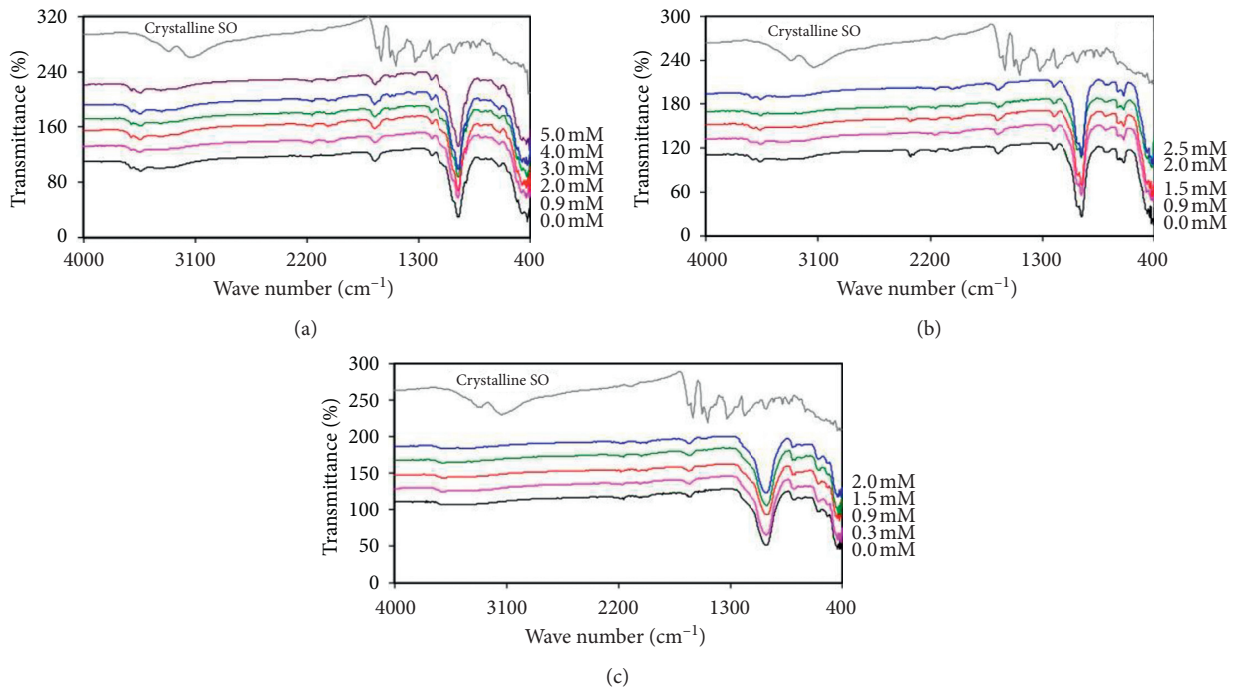
Figure 5: FTIR spectra of PAL (a), SEP (b), and ZEO (c) after SO sorption from different initial concentrations.
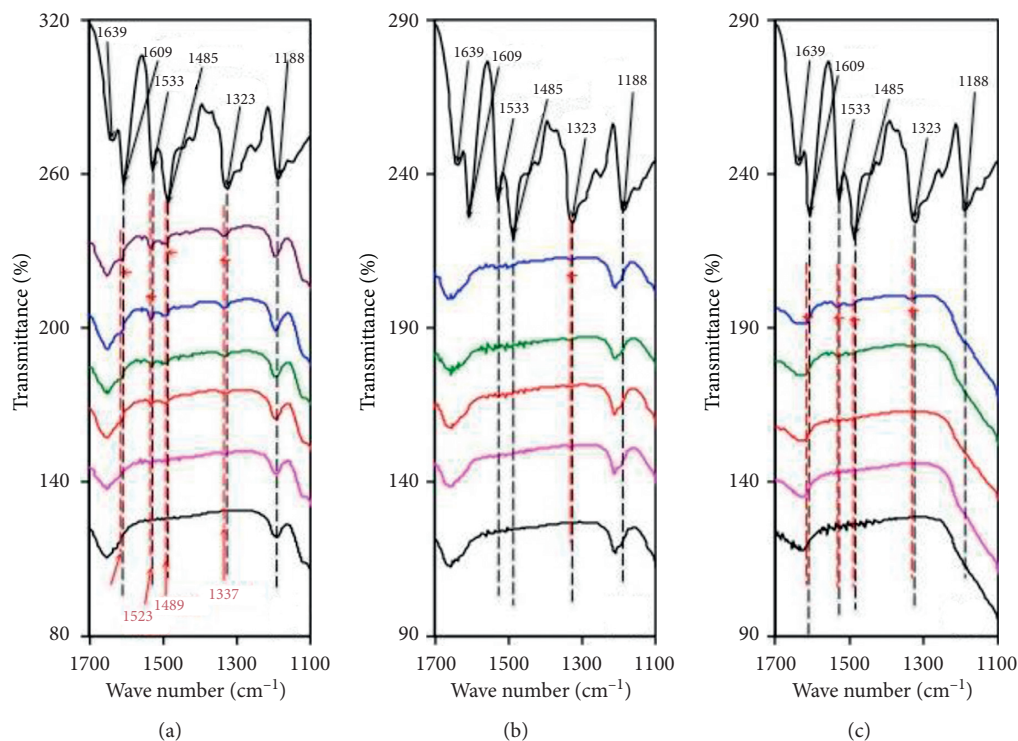
Figure 6: FTIR spectra of PAL (a), SEP (b), and ZEO (c) after SO sorption from different initial concentrations showing the enlargement at the wavenumbers of $1100–1700 \, cm^{-1}$.

they shifted to 1339, 1491, 1533, and $1618 \, cm^{-1}$ (Figure 6(c)). These shifts, particularly the C = N stretching vibration band located at $1323 \, cm^{-1}$, confirmed the participation of the C = N bond for the SO uptake on these mineral surfaces (Figure 6). Also, taking the consideration of the formula mass of 350 g/mol for SO, the sensitivity of FTIR for detection of sorbed SO is at the level of about 40 mmol/kg or 1.4%.

3.6. Molecular Dynamic Simulation. Molecular dynamic simulation was used to decipher the surface configuration of sorbed SO^+ cations at the sorption capacity for the minerals. For PAL and SEP, a supercell made of $2bx4c$ was used for the simulation, and the number of SO^+ cations used per supercell was calculated from the SO sorption capacity and the SSA of the minerals. The sorbed SO^+ cations formed a condensed monolayer configuration on PAL (Figure 7). In contrast, at the SO sorption maximum, the SO^+ cations formed monomers on SEP surfaces due to its much lower CEC and large SSA values (Figure 8). In both cases, the phenazine rings are parallel to the surfaces. ZEO is a granular mineral and supercells were made of $2bx4c$, $2ax4c$, and $2ax1.5b$, and the number of SO molecules used per supercell was calculated from the SO sorption capacity and the SSA of the minerals. Multilayer or admicelle formation of SO on ZEO was obtained because of the very low SSA value of ZEO (Figures 9–11).

3.7. Discussion. The CEC values are 175 [25] and 15 [26] meq/kg for PAL and SEP, respectively, while the ECEC for ZEO is 90 meq/kg [28]. Meanwhile, the SO uptake capacity was 195, 45, and 79 mmol/kg for PAL, SEP, and ZEO, respectively (Figure 2(b)), strongly suggesting that cation exchange played a crucial role in SO removal. On the other hand, their SSA values are 173 [27] and $250 \, m^2/g$ [26] and the SSA is $15.7 \, m^2/g$ [28] for PAL, SEP, and ZEO, respectively. As the XRD results showed no changes in d-spacings for all minerals (Figure 4), it suggested that the uptake of SO was on the external surfaces of the minerals. Using the CEC and SSA values, the calculated area per SO^+ occupied at the uptake capacity is 1.5, 9.3, and $0.33 \, nm^2$ for PAL, SEP, and ZEO, respectively. Meanwhile, the dimension of SO molecule is 1.16 nm long by 0.96 nm wide by 0.4 nm thick (Figure 1). The molecular simulation showed flat-lying SO^+ cations on {100} surface of PAL and SEP (Figures 7 and 8). Thus, a close monolayer packing of SO^+ on PAL and loose monomer packing of SO^+ on SEP suggested that the influence of SSA on SO uptake may not be critical. For ZEO, the SO sorption density was $0.33 \, nm^2$ per SO^+ cation, much smaller than the dimension of SO. As SO may form dimers in solution and its dimer concentration increased with increasing SO concentration [34], formation of SO multilayer or admicelles on ZEO is extremely likely due to its limited SSA and large ECEC and was confirmed by the molecular dynamic simulation (Figures 9–11).

(a)

(b)
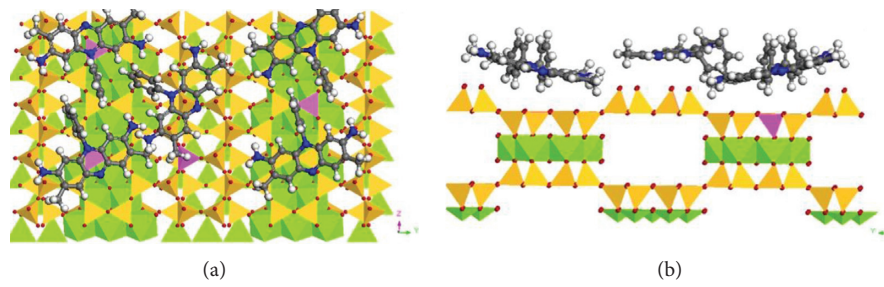
Figure 7: Molecular dynamic simulation showing SO uptake on the {100} surface (a) and projection along [001] (b) of PAL with 4 Si replaced with 4 Al in the supercell.

(a)

(b)
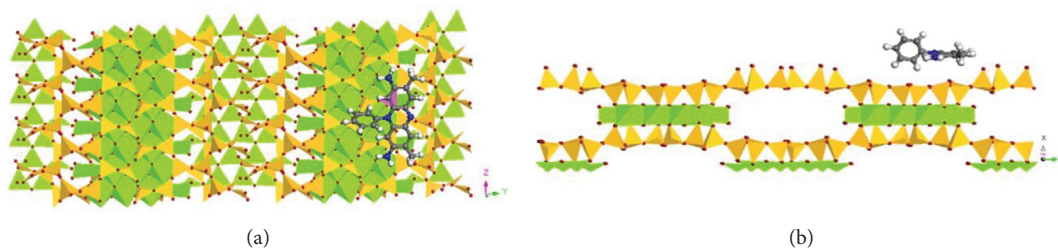
Figure 8: Molecular dynamic simulation showing SO uptake on the {100} surface (a) and projection along [001] (b) of SEP with 1 Si replaced with 1 Al in the supercell.

(a)

(b)
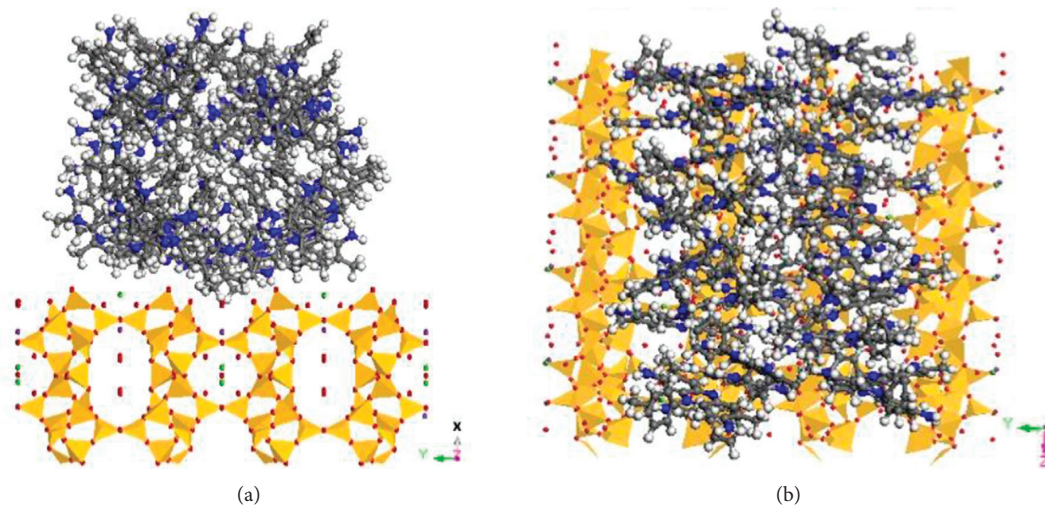
Figure 9: Molecular dynamic simulation showing SO uptake on the {100} surface (a) and projection along [100] (b) of ZEO. Supercell is made of 2bx4c.

(a)

(b)
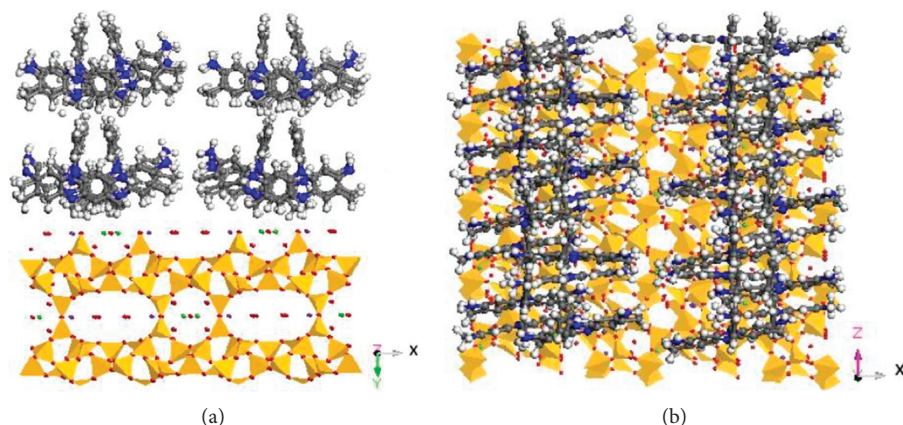
FIGURE 10: Molecular dynamic simulation showing SO uptake on the {010} surface (a) and projection along [010] (b) of ZEO. Supercell is made of 2*a*x4*c*.

(a)

(b)
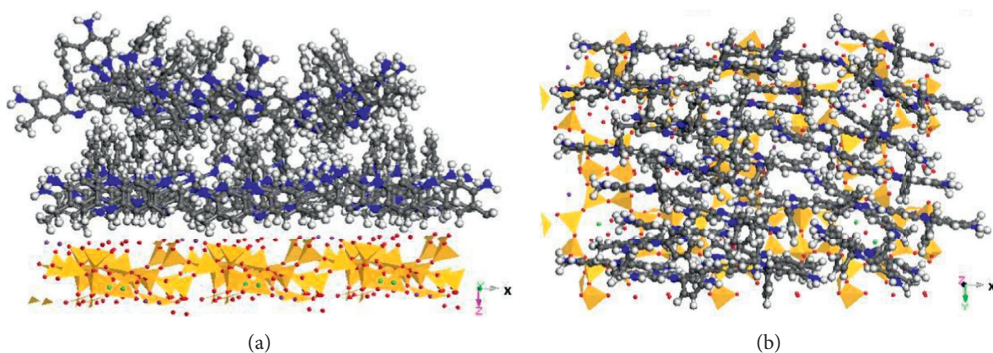
FIGURE 11: Molecular dynamic simulation showing SO uptake on the {001} surface (a) and projection along [001] (b) of ZEO. Supercell is made of 2*a*x1.5*b*.

4. Conclusion

In this study, the sorptive removal of SO using fibrous clay minerals palygorskite and sepiolite and tectosilicate clinoptilolite zeolite was assessed under different physicochemical conditions. The results revealed that the SO removal capacity by these minerals was primarily controlled by their cation exchange capacity, suggesting cation exchange between SO^+ and inorganic cations played a key role in SO removal. Other physicochemical parameters such as equilibrium, solution pH, and ionic strength had minimal effect on SO removal. The sorbed SO^+ cations may form loosely packed monomers, densely packed monolayer, and multilayer or admicelle formations limited by the specific surface area of the minerals. The XRD results confirmed that the sorbed SO^+ cations were limited to the external surfaces of the minerals as the dimension of SO^+ is larger than the channel size of the minerals. The FTIR results suggested participation of N^+ in the benzene ring for the electrostatic interaction with negatively charged Si-O tetrahedral surface. The electrostatic interactions between SO^+ and negatively charged mineral surfaces and the SO^+ surface configurations on mineral surfaces were confirmed by molecular dynamic simulations. As a result, the clay minerals with high CEC and SSA values are good candidates for cationic dye removal from water.

Data Availability

The data used to support the findings of the current study are available from the corresponding author upon request.

Conflicts of Interest

The authors declare that they have no conflicts of interest.

Acknowledgments

References

[1] S. Preethi, A. Sivasamy, S. Sivanesan, V. Ramamurthi, and G. Swaminathan, "Removal of safranin basic dye from aqueous solutions by adsorption onto corncob activated carbon," *Industrial & Engineering Chemistry Research*, vol. 45, no. 22, pp. 7627–7632, 2006.

[2] A. Tkaczyk, K. Mitrowska, and A. Posyniak, "Synthetic organic dyes as contaminants of the aquatic environment and their implications for ecosystems: a review," *Science of the Total Environment*, vol. 717, Article ID 137222, 2020.

[3] X.-L. Cao, Y.-N. Yan, F.-Y. Zhou, and S.-P. Sun, "Tailoring nanofiltration membranes for effective removing dye intermediates in complex dye-wastewater," *Journal of Membrane Science*, vol. 595, Article ID 117476, 2020.

[4] U. Shanker, M. Rani, and V. Jassal, "Degradation of hazardous organic dyes in water by nanomaterials," *Environmental Chemistry Letters*, vol. 15, no. 4, pp. 623–642, 2017.

[5] S. N. Singh, Ed., *Microbial Degradation of Synthetic Dyes in Wastewaters*, Springer, Berlin, Germany, 2014.

[6] A. H. Jawad, N. S. A. Mubarak, and A. S. Abdulhameed, "Hybrid crosslinked chitosan-epichlorohydrin/TiO2 nanocomposite for reactive red 120 dye adsorption: kinetic, isotherm, thermodynamic, and mechanism study," *Journal of Polymers and the Environment*, vol. 28, no. 2, pp. 624–637, 2020.

[7] S. Kaur, S. Rani, R. K. Mahajan, M. Asif, and V. K. Gupta, "Synthesis and adsorption properties of mesoporous material for the removal of dye safranin: kinetics, equilibrium, and thermodynamics," *Journal of Industrial and Engineering Chemistry*, vol. 22, pp. 19–27, 2015.

[8] M. S. Thabet and A. M. Ismaiel, "Saudi Arabia natural clay: characterization, equilibrium, kinetics and thermodynamics models for elimination of textile dyes," *International Journal of Environmental Monitoring and Protection*, vol. 5, no. 2, pp. 31–39, 2018.

[9] V. Gómez, M. S. Larrechi, and M. P. Callao, "Kinetic and adsorption study of acid dye removal using activated carbon," *Chemosphere*, vol. 69, no. 7, pp. 1151–1158, 2007.

[10] N. Peinemann and A. K. Helmy, "Cation exchange capacities of safranin, toluidine and alizarin complexes with montmorillonite," *Soil Science*, vol. 164, no. 9, pp. 650–654, 1999.

[11] S. S. Al-Shahrani, "Removal of safranin dye from wastewater using Khulays natural bentonite," *Journal of King Abdulaziz University*, vol. 29, no. 1, pp. 49–58, 2018.

[12] K. O. Adebowale, B. I. Olu-Owolabi, and E. C. Chigbundu, "Removal of safranin-O from aqueous solution by adsorption onto kaolinite clay," *Journal of Encapsulation and Adsorption Sciences*, vol. 4, no. 3, pp. 89–104, 2014.

[13] R. G. Harris, J. D. Wells, and B. B. Johnson, "Selective adsorption of dyes and other organic molecules to kaolinite and oxide surfaces," *Colloids and Surfaces A: Physicochemical and Engineering Aspects*, vol. 180, no. 1-2, pp. 131–140, 2001.

[14] M. R. Abukhadra, M. A. El-Meligy, and A. M. El-Sherbeeny, "Evaluation and characterization of Egyptian ferruginous kaolinite as adsorbent and heterogeneous catalyst for effective removal of safranin-O cationic dye from water," *Arabian Journal of Geosciences*, vol. 13, no. 4, p. 169, 2020.

[15] E. Galán, "Properties and applications of palygorskite-sepiolite clays," *Clay Minerals*, vol. 31, no. 4, pp. 443–453, 1996.

[16] D. N. Taha, I. A. S. Samaka, and L. A. Mohammed, "Adsorptive removal of dye from industrial effluents using natural Iraqi palygorskite clay as low-cost adsorbent," *Journal of Asian Scientific Research*, vol. 3, no. 9, pp. 945–955, 2013.

[17] M. Fayazi, D. Afzali, M. A. Taher, A. Mostafavi, and V. K. Gupta, "Removal of safranin dye from aqueous solution using magnetic mesoporous clay: optimization study," *Journal of Molecular Liquids*, vol. 212, pp. 675–685, 2015.

[18] T. Rohani and M. S. Seyedghasemi, "Application of surfactant-coated magnetic zeolite NaA as a new sorbent to remove safranin O dye from aqueous solutions," *Bulgarian Chemical Communications*, vol. 49, pp. 323–328, 2017.

[19] V. Hovhannisyan, C. Y. Dong, and S. J. Chen, "Photodynamic dye adsorption and release performance of natural zeolite," *Scientific Reports*, vol. 7, Article ID 45503, 2017.

[20] M. Qiu, C. Qian, J. Xu, J. Wu, and G. Wang, "Studies on the adsorption of dyes into clinoptilolite," *Desalination*, vol. 243, no. 1–3, pp. 286–292, 2009.

[21] A. Badeenezhad, A. Azhdarpoor, S. Bahrami, and S. Yousefinejad, "Removal of methylene blue dye from aqueous solutions by natural clinoptilolite and clinoptilolite modified by iron oxide nanoparticles," *Molecular Simulation*, vol. 45, no. 7, pp. 564–571, 2019.

[22] M. R. Abukhadra and A. S. Mohamed, "Adsorption removal of safranin dye contaminants from water using various types of natural zeolite," *Silicon*, vol. 11, no. 3, pp. 1635–1647, 2019.

[23] R. Ebrahimi, A. Maleki, B. Shahmoradi et al., "Organic dye removal from aqueous media by using acid modified clinoptilolite," *Journal of Advances in Environmental Health Research*, vol. 6, no. 2, pp. 118–127, 2018.

[24] S. Bekkouche, S. Merouani, O. Hamdaoui, and M. Bouhelassa, "Efficient photocatalytic degradation of safranin O by integrating solar-UV/TiO2/persulfate treatment: implication of sulfate radical in the oxidation process and effect of various water matrix components," *Journal of Photochemistry and Photobiology A: Chemistry*, vol. 345, pp. 80–91, 2017.

[25] D. Borden and R. F. Giese, "Baseline studies of the clay minerals society source clays: cation exchange capacity measurements by the ammonia-electrode method," *Clays and Clay Minerals*, vol. 49, no. 5, pp. 444-445, 2001.

[26] Z. Li, C. A. Willms, and K. Kniola, "Removal of anionic contaminants using surfactant-modified palygorskite and sepiolite," *Clays and Clay Minerals*, vol. 51, no. 4, pp. 445–451, 2003.

[27] A. U. Dogan, M. Dogan, M. Onal, Y. Sarikaya, A. Aburub, and D. E. Wurster, "Baseline studies of the clay minerals society source clays: specific surface area by the brunauer emmett teller (BET) method," *Clays and Clay Minerals*, vol. 54, no. 1, pp. 62–66, 2006.

[28] Z. Li and R. S. Bowman, "Counterion effects on the sorption of cationic surfactant and chromate on natural clinoptilolite," *Environmental Science & Technology*, vol. 31, no. 8, pp. 2407–2412, 1997.

[29] S. Manna, P. Das, and D. Roy, "Dye-containing wastewater treatment using treated jute," in *Waste Management and Resource Efficiency*, pp. 1263–1270, Springer, Singapore, Asia, 2019.

[30] F. Zhao and M. Sillanpää, "Cross-linked chitosan and β-cyclodextrin as functional adsorbents in water treatment," in *Advanced Water Treatment*, pp. 161–264, Elsevier, Amsterdam, Netherlands, 2020.

[31] R. Yang, D. Li, A. Li, and H. Yang, "Adsorption properties and mechanisms of palygorskite for removal of various ionic dyes from water," *Applied Clay Science*, vol. 151, pp. 20–28, 2018.

[32] P. Pereira, B. Ferreira, N. Oliveira et al., "Synthesis of zeolite a from metakaolin and its application in the adsorption of cationic dyes," *Applied Sciences*, vol. 8, no. 4, p. 608, 2018.

[33] S. Das and S. Barman, "Studies on removal of safranine-t and methyl orange dyes from aqueous solution using Nax zeolite synthesized from fly ash," *International Journal of Science, Environment and Technology*, vol. 2, no. 4, pp. 735–747, 2013.

[34] G. Balaji, R. K. Rekha, and A. Ramalingam, "Nonlinear characterization of safranin O dye for application in optical limiting," *Acta Physica Polonica A*, vol. 119, no. 3, pp. 359–363, 2011.

[35] N. Mansouri, N. Rikhtegar, H. A. Panahi, F. Atabi, and B. K. Shahraki, "Porosity, characterization and structural properties of natural zeolite-clinoptilolite-as a sorbent,"

Environment Protection Engineering, vol. 39, no. 1, pp. 139–152, 2013.

[36] M. K. Sahu and R. K. Patel, "Removal of safranin-O dye from aqueous solution using modified red mud: kinetics and equilibrium studies," *RSC Advances*, vol. 5, no. 96, pp. 78491–78501, 2015.

[37] S. A. Moon, B. K. Salunke, P. Saha, A. R. Deshmukh, and B. S. Kim, "Comparison of dye degradation potential of biosynthesized copper oxide, manganese dioxide, and silver nanoparticles using Kalopanax pictus plant extract," *Korean Journal of Chemical Engineering*, vol. 35, no. 3, pp. 702–708, 2018.

[38] H. Van Damme, M. Crespan, M. I. Cruz, and J. J. Fripiat, "Adsorption of safranine by Na^+, Ni^{2+} and Fe^{3+} montmorillonites," *Clays and Clay Minerals*, vol. 25, no. 1, pp. 19–25, 1977.

Research Article

Numerical Modelling of Clay Seal Maturation in Deep Boreholes with Nuclear Waste

Ting Yang [1], **Hans Mattsson** [2], **Roland Pusch** [2], **Jan Laue** [2], **Sven Knutsson** [2], **and Xiaodong Liu**[1,3]

[1]*State Key Laboratory of Nuclear Resources and Environment, East China University of Technology (ECUT), Nanchang 330013, China*
[2]*Department of Civil, Environmental and Natural Resources Engineering, Luleå University of Technology (LTU), Luleå, Sweden*
[3]*Jiu Jiang University, Jiujiang, China*

Correspondence should be addressed to Ting Yang; yt1551@126.com

One of the major challenges of high-level nuclear waste (HLW) isolation in deep boreholes is to anticipate the maturation behaviour of swelling clay when the waste, surrounded by dense clay encased in perforated tubes, is submerged into the borehole mud. The ultimate homogeneity of this clay seal acting as a barrier is expected to stabilize the borehole and to prevent possible leakage of radioactivity. In this study, a numerical model for predicting the maturation of the clay barrier has been developed. In the model, the water transport is controlled by the differences in the suction potential and the permeability. The model is able to simulate the maturation process, both the expeditious water transport and the clay migration into the surrounding mud, from beginning to end. Results from laboratory tests of the clay maturation were compared with the predictions made by the model. They are in good agreement, but refinement is proposed by taking the impact of the tube perforation on the maturation rate into more consideration. The proposed numerical model will also be useful in selecting a suitable design for clay barriers in HLW boreholes. Different combinations of clay dimensions and initial densities of mud and dense clay can thus be studied to determine the final homogenization and the end densities.

1. Introduction

One concept to store high-level radioactive waste (HLW) is to place it in canisters in the bottom regions of a very deep borehole (VDH); see Figure 1. To prevent leakage of radioactivity, the canisters are surrounded by a dense swelling clay. Dense swelling clay is also placed in blocks above the canisters in the boreholes. The canisters and the swelling clay are submerged in the boreholes into a clay mud [1]. The dense swelling clay and clay mud are called clay seals. Maturation of a clay seal is the process in which the dense clay comes in contact with water and swells against the borehole walls, creating a barrier of low permeability to prevent the possible leakage of radionuclides.

This study focuses on the numerical modelling of the maturation of clay seals in VDHs for HLW disposal. To the

authors' knowledge, this type of model has still not been proposed by anyone until now. However, in a paper by Börgesson et al. [2] a laboratory test on bentonite clay was modelled with focus on radially swelling using a commercial finite element software. Good agreement between experimental and numerical result was obtained with a constitutive model the researchers had developed themselves. The maturation of clay seals was not modelled, but since radial swelling is an important part, this strategy might be successful in modelling the maturation of clay seals too. The numerical model proposed in this study simulates the water transport and the soil migration process during the swelling from the initial heterogeneous state of mud and dense clay to the ultimate homogeneous condition of the entire clay seal. The model could be used to determine the duration of the maturation process for different designs of the storage
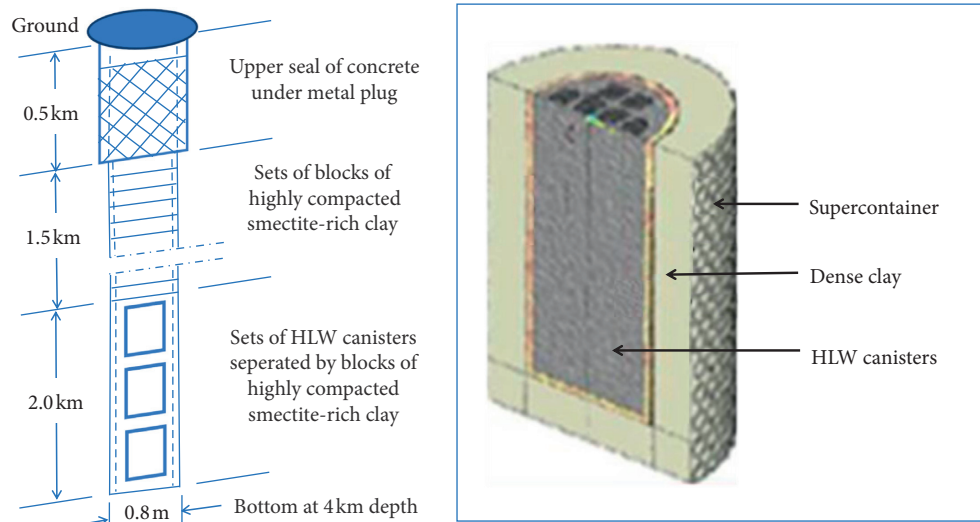
FIGURE 1: Schematic illustration of VDH concept. The package shown on the right consists of a supercontainer with a clay-embedded canister containing spent fuel [6, 7].

concept. If the maturation process goes too fast, it will be problematic to install the canisters and the dense clay into the boreholes. If the process goes too slow or stops before a proper barrier is created, leakage of radioactivity is not prevented as intended.

To verify the numerical model, laboratory tests of the maturation process were performed and the test results compared with the model predictions. The maturation process in real boreholes is also simulated in the study, as an example of how the numerical model can be utilized in real design.

2. Clay-Based Barriers in Very Deep Boreholes with Spent Reactor Fuel

Very deep boreholes repository concepts have gained interest in countries like the US and the UK because of lower costs, faster construction, and simpler and safer placement of high-level radioactive waste [3]. Sweden has 10 nuclear reactors, each with a 1,000 MW capacity, which need to dispose of 40 years' worth of spent fuel which is currently on intermediate storage. A successive placement of canisters could be made in 20 to 25 years, utilizing 4 to 12 multiple borehole sites with depths between 2.5 and 4 km, and a spacing of 200 m between individual holes to prevent thermal overlap. Further details on the concept can be found in, e.g., the paper by Sandstedt et al. [4].

Figure 1 illustrates the barriers—the metal canisters and the surrounding dense smectite-rich clay—that prevent the dissemination of radionuclides in the "deployment zone" [5]. Above the canisters, the hole is sealed by placing perforated supercontainers filled solely with dense smectite clay. The containers will be submerged in smectite clay mud. The containers are necessary in order to get the clay in place, and the dense clay will be in contact with the mud when the clay swells through the holes in the supercontainers.

In this study, the numerical model is utilized on the part of the borehole where the supercontainers are filled with only dense swelling clay. The heat production caused by radioactive decay in the zone with canisters is not accounted for in the numerical model. The influence of the perforated supercontainers (tubes in laboratory tests) on the maturation process is not included in the numerical model, but the influence was examined by deriving a relationship between the maturation times with and without a tube, based on laboratory tests.

3. Laboratory Test of Maturation

Laboratory tests of the maturation process were performed to simulate the in situ situation of a VDH. The test setup is presented in Figure 2(c). The components in the setup, from the outside to the inside, are as follows: a 9 mm thick pervious acrylate-stabilized sand tube (sand filter), the 6.5 mm thick soft clay mud, a 2 mm thick steel tube with 50% perforation (representing a supercontainer), and dense swelling clay with the radial thickness 43 mm as sealing material. The 124 mm high steel tubes were closed at the ends by steel plates. The entire setup was submerged in water in order to keep the sand filter continuously saturated during the tests.

The expansive Holmehus clay, produced in Southern Denmark, was the sealing material used in the tests [7]. It is an illite/smectite mixed-layer clay with approximately 60% montmorillonite. The behaviour of swelling clays can be studied in, e.g., the paper by Mitchell and Soga [8]. The clay specimens were manufactured by mixing the air-dry granulate with dry water [9] to become fully water-saturated at uniaxial compaction to a dry density of 1550 kg/m^3 [7]. The dense clay blocks in the perforated tubes, surrounded by soft clay mud, were contained in the filter for maturation in 6, 12, 24, 48, and 96 hours and one year. Figure 2(b) shows that, after a certain time of maturation, the dense clay started to swell through the perforation, forming small clay columns

(a)

(b)

Sand filter

Dense clay

Water

Mud

Perforated tube

(c)
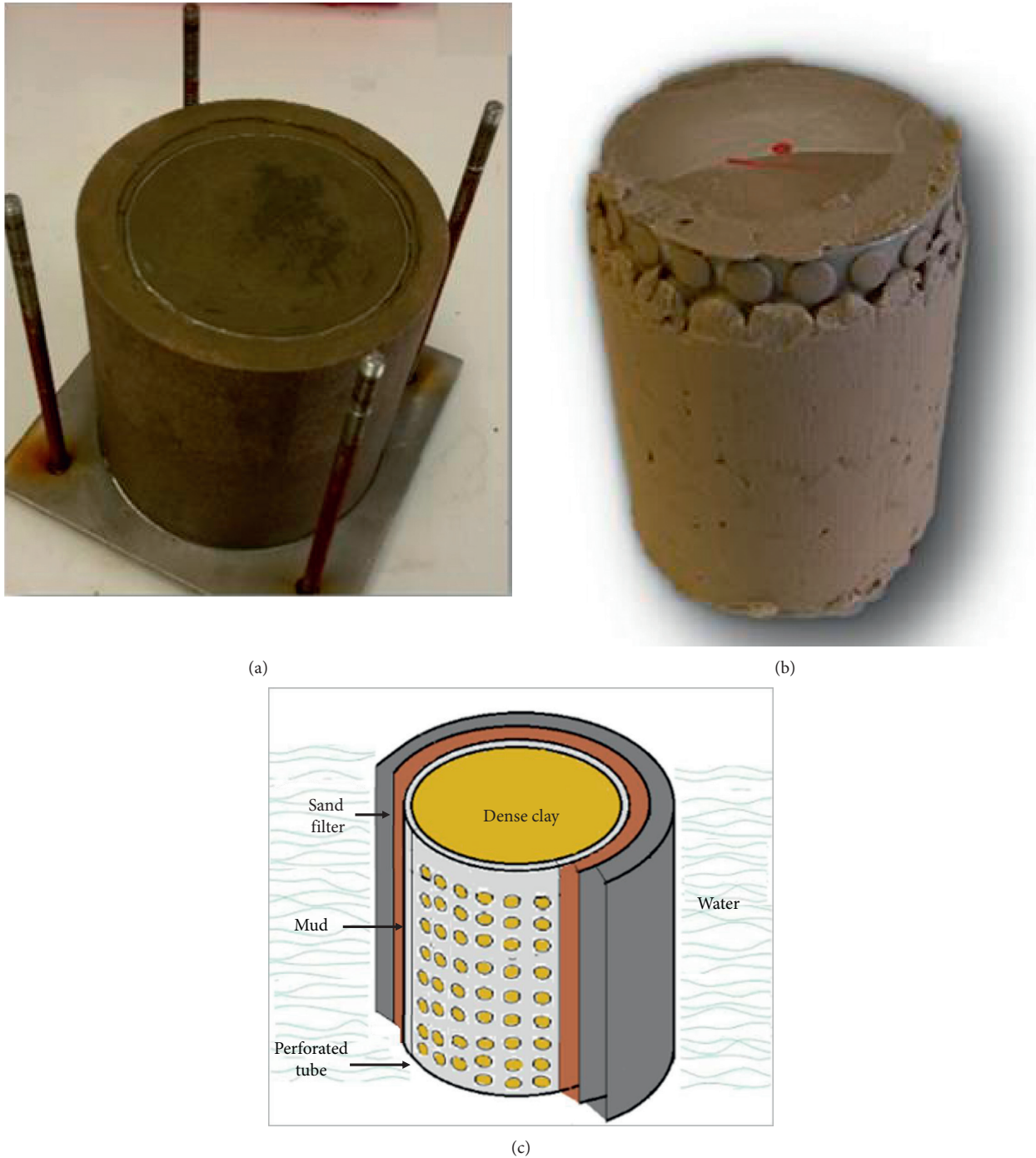
FIGURE 2: Instrument in the laboratory test. (a) Setup with clay seals after maturation, with the top lid removed; (b) 96-hour laboratory experiment with clay plugs in perforated steel tubes surrounded by mud; (c) schematic illustration of test setup with clay seals (soft clay mud and dense clay blocks).

that displaced mud. Due to the difference in suction between the mud and the dense clay, and also within the different parts of the dense clay, the mud hardened while the dense clay softened during the maturation process. Figure 2(a) illustrates the laboratory setup at an advanced stage of maturation. After each maturation test, the densified mud and the softened dense clay were examined with respect to the water content and the dry density at different radial distances from the middle, by cutting out and examining hollow cylindrical pieces of the specimen [7].

4. Numerical Model of Maturation of Clay Seals

4.1. The Proposed Model. In the case of maturation of clay seals in a borehole, the key assumptions and criteria in the model are as follows:

(1) Darcy's law is valid between each element in the numerical algorithm

(2) Both dense clay and mud are initially homogeneous

(3) The total volume inside the hollow cylinder filter, containing fully saturated dense clay and mud, is constant during the entire maturation process

(4) Expansion/contraction and flow take place only in the radial direction

(5) There is no temperature dependence, e.g., from heat production caused by radioactive decay

Darcy's law is expected to give an accurate representation of the flow within a porous medium for small discharge velocities [10]. Water flow is slow in the maturation process, so it is assumed that Darcy's law is applicable on the elements in the numerical algorithm. Darcy's law states that $q = Aki$, where the fluid flux q is related to the cross-sectional area A, the hydraulic conductivity k, and the hydraulic gradient i. The permeated fluid volume Q in time t_0 is given by

$$Q = Akit_0. \tag{1}$$

With the height of the cylinder specimen H and the radius R, the permeated fluid volume becomes

$$Q = 2\pi R H k \frac{dh}{dR} t_0, \tag{2}$$

where h is the water head and (dh/dR) is the hydraulic gradient i.

Rearranging and integrating equation (2) gives

$$Q \cdot \int_{R_1}^{R_2} \frac{1}{R} dR = \int_{h_1}^{h_2} 2\pi k t_0 H dh. \tag{3}$$

Thus,

$$Q = \frac{2\pi k H}{\ln(R_2/R_1)} (h_2 - h_1) \cdot t_0, \tag{4}$$

where R_1 and R_2 represent the flow path. $(h_2 - h_1)$ is the hydraulic head difference causing water transport.

The hydraulic gradient and thereby the hydration/dehydration of the dense clay is a function of the position of the clay elements and of the maturation time. Therefore, the dense clay is considered to consist of a sequence of elements (Figure 3(a)), subjected to one-dimensional hydration or dehydration, implying only radial flow and clay particle migration. Because of the rotational symmetry, only the radial plane of the clay sample is viewed (Figure 3(b)). If a unit sample with height ΔZ and initial radial length R is divided into N elements (N is a natural number), the initial size of each element and the distance from its centre to the symmetry axis are Δr_n and r_n ($n = 1, 2, 3, \ldots, N$), respectively. For the mud, the corresponding parameters are Δr_{mud} and r_{mud}, respectively.

Theoretically, in the clay seals, water is absorbed from the mud by the nearest clay element, followed by the water movement in the series of elements taking place from the centre of an element to the centre of the adjacent one. Therefore, in the model, the values of permeability and suction should be representative from the centre of the clay element to the centre of the adjacent one. The hydraulic conductivity is proposed to be a weighted average value $\overline{k}_n(t)$ between the centres of clay elements. If the hydraulic conductivities in the flow path direction have large differences in magnitude, they can lead to numerical problems. To avoid these problems, the weighted average hydraulic conductivity is calculated using equation (18) and the weighted average dry density $\overline{\rho}_{d(n)}(t)$, which is the value weighted with respect to the thickness of clay elements.

Based on the derived equation (4), the suction difference between elements $\Delta U_{e(n)}(t)$ associated with the hydraulic head difference gives the volume of transported water from element $n - 1$ to element n as

$$Q_n(t) = \frac{2\pi \overline{k}_n(t)_{r_{(n-1)}(t) \longrightarrow r_n(t)} \Delta Z}{\ln r_{(n-1)}(t)/r_n(t)} \cdot \frac{\Delta U_{e(n)}(t)}{\gamma_{\text{water}}} \Delta t, \tag{5}$$

where γ_{water} is the unit weight of water. Δt is the maturation time in the tth time step, assuming T to be the total time. Thus, $t \in (1, 2, 3, \ldots, \lfloor T/\Delta t \rfloor)$, and $(t - 1) = 0$ means the initial status before maturation. The subscript $(n - 1) = 0$ represents the mud. The parameters hydraulic conductivity $k_n(t)$ and suction $U_{e(n)}(t)$ are a function of the dry density. The hydraulic conductivity depends on the void ratio, which is a function of dry density. Yang et al. [7] have experimentally verified that the suction is a function of dry density. The expressions of $k_n(t)$ and $U_{e(n)}(t)$ as function of dry density are based on laboratory experiments and presented in Section 4.2.

The initial dry density of the mud in the laboratory tests was $222 \, \text{kg/m}^3$, meaning that the clay particles formed a stable clay gel. At the beginning of the maturation process, due to the easily accessible water in the mud, the water transport is from the interface of mud/dense clay to the centre of the first element at distance $r_1(t)$. The permeability controlling the transport into the first element is determined by the k value of the first element. Therefore, the volume of water flowing into the first element during the initial maturation period is

$$Q_1(t) = \frac{2\pi k_1(t)_{R(t) \longrightarrow r_1(t)} \Delta Z}{\ln(R(t)/r_1(t))} \cdot \frac{\Delta U_{e(1)}(t)}{\gamma_{\text{water}}} \Delta t. \tag{6}$$

Along with the reduction of water in the mud, the soil particles come in closer contact with each other and from the moment $(k_1(t)/\ln(R(t)/r_1(t))) \geq (\overline{k}_1(t)/\ln(r_{\text{mud}}(t)/r_1(t)))$, water is no longer considered to be easily accessible from the mud. From that point, it is assumed that water starts to be transported from the centre of the mud to the centre of the first dense clay element, and the densified mud is considered to be one element among all others. The mathematical expression of the water volume flowing into the first element during this subsequent maturation period is

$$Q_1'(t) = \left(\frac{2\pi \overline{k}_1(t)_{r_{\text{mud}(t)} \longrightarrow r_1(t)} \Delta Z}{\ln(r_{\text{mud}}(t)/r_1(t))} \right) \cdot \left(\Delta U_{e(1)}(t)/\gamma_{\text{water}} \right) \Delta t. \tag{7}$$
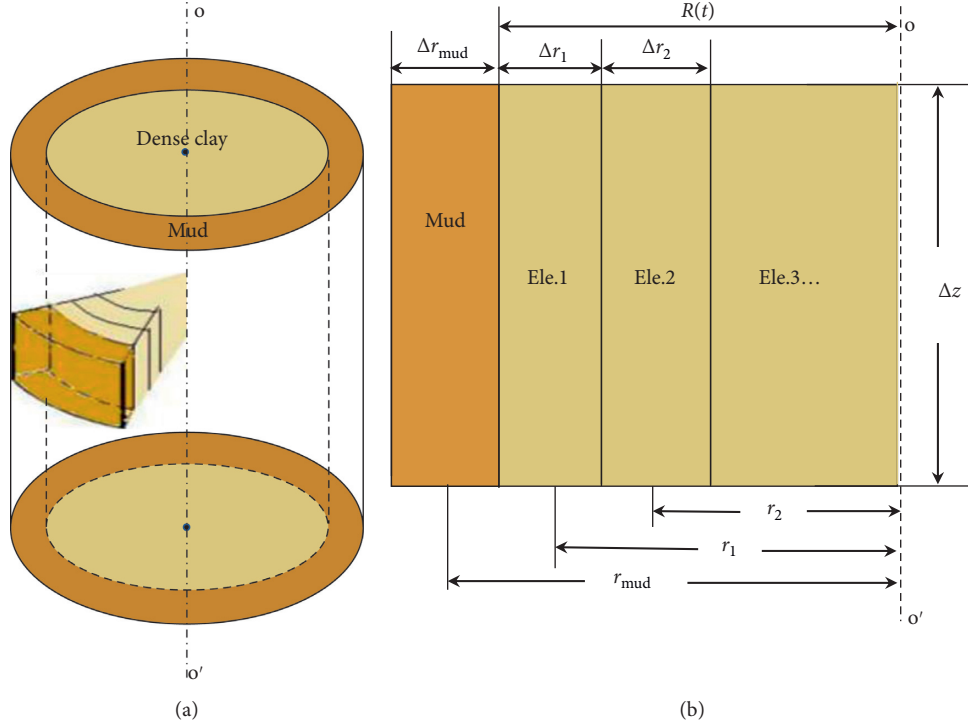
FIGURE 3: Schematic view of specimen and maturation. (a) Clay specimen surrounded by water-rich mud, absorbing water in radial direction. (b) Division of dense clay into elements for the numerical modelling.

For each element, water is both flowing into and out of the element. The volume of water that stays in the element is

$$\Delta Q_n(t) = Q_n(t) - Q_{(n+1)}(t). \tag{8}$$

Since the clay seals are closed at the top and the bottom, the dense clay swells only in the radial direction. The volume of clay expansion in each element is equal to the volume of water taken up by the element. Thus, the radial expansion of each element during the time Δt becomes

$$\Delta r_n^*(t) = -\frac{2r_n(t-1) + \Delta r_n(t-1)}{2}$$
$$+ \sqrt{\left(\frac{2r_n(t-1) + \Delta r_n(t-1)}{2}\right)^2 + \frac{\Delta Q_n(t)}{\Delta Z} \cdot \frac{1}{\pi}}. \tag{9}$$

The total radial expansion of all clay elements during the time step is

$$r_n^*(t) = \sum_{i=1}^{N} \Delta r_i^*(t). \tag{10}$$

The new radius of the dense clay $R(t)$ after swelling becomes

$$R(t) = R(t-1) + r_n^*(t). \tag{11}$$

The mud will be compressed with the same volume as the increased volume of the dense clay. The reduced radial thickness of the mud $\Delta r_{mud}^*(t)$ is the negative value of the total radial expansion of the dense clay elements.

Based on the expansion of clay, the state parameters of clay elements and mud can be updated with time as follows:

$$r_n(t) = r_n(t-1) + \frac{1}{2}\Delta r_n^*(t) + \sum_{i=n+1}^{N} \Delta r_i^*(t), \tag{12}$$

$$\Delta r_n(t) = \Delta r_n(t-1) + \Delta r_n^*(t), \tag{13}$$

$$r_{mud}(t) = r_{mud}(t-1) - \frac{1}{2}\Delta r_{mud}^*(t), \tag{14}$$

$$\Delta r_{mud}(t) = \Delta r_{mud}(t-1) + \Delta r_{mud}^*(t). \tag{15}$$

Thereby, the dry density of each element becomes

$$\rho_{d(n)}(t) = \rho_{d(n)}(t-1)\frac{\Delta r_n(t)r_n(t)}{\Delta r_n(t-1)r_n(t-1)}. \tag{16}$$

And for the mud

$$\rho_{d(mud)}(t) = \rho_{d(mud)}(t-1)\frac{\Delta r_{mud}(t)r_{mud}(t)}{\Delta r_{mud}(t-1)r_{mud}(t-1)}. \tag{17}$$

4.2. Soil Properties for the Numerical Modelling.
To understand how the physicochemical processes of swelling clay are accounted for in the numerical model, these processes need to be briefly described. Air-dry expansive smectite clay has one thin layer of water molecules between the thin clay lamellae and on the outside of the stacks of lamellae. In

humid air and submerged in water, additional water is adsorbed by the strong affinity of the clay to water molecules, which become ordered through a pseudo-crystalline process. The adsorption is driven by this affinity (hydration potential) that causes tension in the water ("suction") and strives to disjoin adjacent particles by causing a "swelling pressure." The swelling pressure is logically of the same order of magnitude as the tension and in practice one assumes that tension is a negative pressure ("suction") while swelling pressure is considered as a positive, real pressure. The affinity

to water reduces with increasing numbers of adsorbed water "hulls" associated with the clay particles; when only a few water molecule layers are adsorbed, no further swelling will occur.

During the numerical modelling, the hydraulic conductivity k and suction for the selected clay material must be known for each element and time step. The suction is expected to be the negative value of the swelling pressure P_s. The parameters k and P_s can be calculated utilizing the following relationships:

$$k = 6 \cdot 10^{-6} \exp\left(-0.01\rho_d\right), \tag{18}$$

$$P_s = \begin{cases} -2.16114 \cdot 10^6 + 0.49613 \cdot 10^6 \exp\left(1.53378 \cdot 10^{-3}\rho_d\right), & \rho_d \geq 960 \,\dfrac{\text{kg}}{\text{m}^3}, \\ 0, & \rho_d < 960 \,\dfrac{\text{kg}}{\text{m}^3}. \end{cases} \tag{19}$$

Based on results obtained from laboratory experiments on Holmehus clay conducted by the authors [7], the relations (18) and (19) are established for quantities in SI-units. Note that the expressions will change with the type of clay, i.e., if the mineral composition and the smectite content are different. Equation (19) is used to calculate the suction difference between elements, a parameter introduced in equation (5).

The physicochemical processes of swelling clay are included in the numerical model by the experimentally established relations of hydraulic conductivity (equation (18)) and swelling pressure (equation (19)), both as a function of dry density. These relations should be seen as soil properties needed for the numerical model.

4.3. Numerical Simulation Procedure. In the numerical simulation, modelling begins with the selection of material properties, i.e., the initial dry density of mud and dense clay, the geometrical parameters $R, \Delta r, r$, and the initial hydraulic conductivity and suction. The modelling was implemented using MATLAB. The procedure is schematically shown in Figure 4 and can be described as follows:

(i) Assume the number of elements to be N and the time for each time step in the computation to be Δt sec. The total computation time is T, which is divided into two parts: $t_1 \in (1, 2, \ldots, m)$ and $t_2 \in (m + 1, \ldots, \lfloor T/\Delta t \rfloor)$. t_1 represents the time step numbers for maturation in the initial stage where water moves from the mud/dense clay interface to the first dense clay element, while t_2 represents the time step numbers in the second stage implying water movement from the centre of the mud to the adjacent dense clay element (Figure 4, right.).

(ii) Computation starts from the first stage t_1, followed by the second stage t_2. In both of these two stages, the volume of water flowing into the first element

and the subsequent elements $Q_n(t)$ is computed. Utilizing the volume of water staying in the elements $\Delta Q_n(t)$, the swelling $\Delta r_n^*(t)$ of each element is computed.

(iii) In each time step, the state parameters of each element are assumed to be constant. As soon as $\Delta r_n^*(t)$ is computed, all the state parameters $R, \Delta r, r, \rho_d, k, U_e$ for both mud and clay elements have to be updated for the next time step (equations (11)–(19)). The iterative simulation process continues until the total time T has been reached, the computation finished, and a solution obtained.

(iv) The procedure above is repeated for the computation with $(N + a)$ elements with time $\Delta t'$ (equation (20), Section 5.1). Here, $a \in (1, 2, \ldots)$. When the computation is completed, the solution is compared with the solution for N elements. If the solutions converge according to a convergence criterion, the solution is accepted. Otherwise, the number of elements is gradually increased with the associated time interval until convergence is reached (Figure 4, left).

5. Numerical Modelling of Laboratory Tests

Numerical modelling has been performed using parameters and boundary conditions relevant to the laboratory tests described in Section 3. The initial dry density was 222 kg/m^3 for the mud and 1550 kg/m^3 for the dense clay. The initial radial thickness was 6.5 mm and 43 mm for mud and dense clay, respectively. Computations for 20, 40, 60, 80, 100, 150, 200, 250, 300, 400, 500, and 800 elements were made, and convergence was reached for 200 elements (see Section 5.1).

5.1. Simulation Results of Clay Maturation

5.1.1. Dry Density of Clay Seals in Maturation. Figure 5 shows that the dry density of the clay components changes
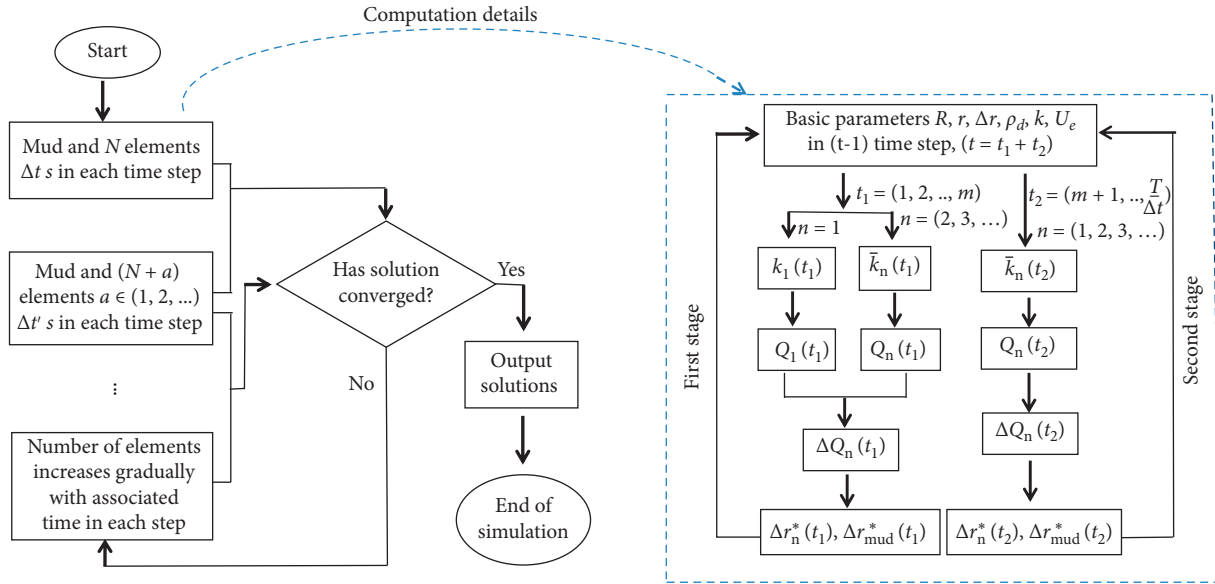
FIGURE 4: Flowchart of numerical solution procedure. Left: overview of the procedure. Right: computation with a certain number of elements N starting with the first time stage t_1, followed by the second time stage t_2.
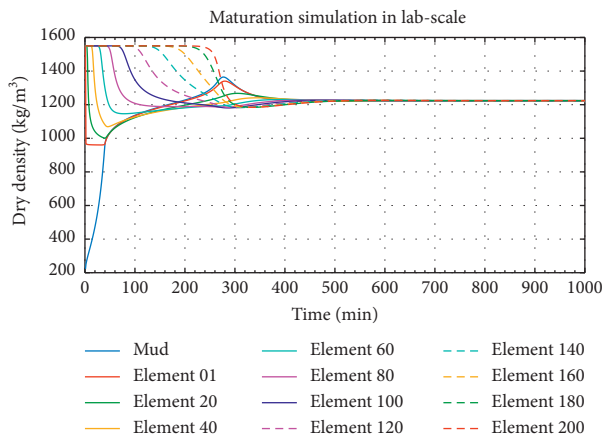
FIGURE 5: Maturation of clay seals in simulation with 200 elements. Plotting with mud and every 20th element.

with the hydration time in the numerical modelling with 200 elements. Along with the fluid flow into the fully saturated dense clay, microstructural reorganisation was successively generated in each of the elements. The study revealed that the dry density of the dense clay elements decreased from $1550\,\mathrm{kg/m^3}$, while the dry density of the mud increased from $222\,\mathrm{kg/m^3}$. In the numerical simulation, the lab-scaled clay seals became isotropic and uniform with a dry density of $1225\,\mathrm{kg/m^3}$ in around 540 minutes. The corresponding hydraulic conductivity and swelling pressure would be $2.90E - 11\,\mathrm{m/s}$ and $1.08\,\mathrm{MPa}$, respectively.

5.1.2. Solid Mass Conservation.
The process of maturation, implying water movement in the clay seal, involves simultaneous swelling of the dense clay and densification of the soft mud in a closed system. The solid mass of both mud and dense clay is conserved throughout the process.

5.1.3. Time Δt for Each Time Step in the Numerical Computation.
The accuracy of the solution is, in general, improved by using a small spacing of elements and a short spacing of time. However, to obtain an accurate and economical solution, the number of elements and the time intervals should not be chosen randomly with respect to each other. In order to simplify these choices, an empirical formula was developed and utilized in the modelling. In a numerical test procedure, the largest Δt for an acceptable solution was determined for each different number of elements. By curve-fitting the results, Δt was obtained as

$$\frac{1}{\Delta t} = -50 + 60\exp\left(N \cdot 6.31522 \cdot 10^{-4}\right), \quad N \le 4500.$$

(20)

Assume the total number of elements N was given.

In a computation, a time step shorter than the designated Δt in equation (20) can also work but is not economical because of the longer computation time. Equation (20) is applicable for numerical simulations of the maturation of the Holmehus clay. The choice of Δt has to be further investigated and verified for other clay types.

5.1.4. Numerical Solution Convergence.
The convergence of the numerical solution is evaluated by using the correlation coefficient ρ_{XY}, implying a certain statistical relationship between two maturation curves X and Y. ρ_{XY} is calculated as covariance divided by standard deviation. For ρ_{XY} approaching unity, the similarity of the curves is high. For $\rho_{XY} = 1$, there is a maximum positive similarity between the two curves, while for $\rho_{XY} = 0$, there is no similarity between them.

The maturation graphs for 20, 40, 60, 80, 100, 150, 200, 250, 300, 400, 500, and 800 elements (Figure 6) show that convergence is reached between 150 and 300 elements.

FIGURE 6: Maturation of the mud in computations with different number of clay elements.

TABLE 1: Correlation coefficient values for multiple number of elements and 800 elements.

Element no., (N)	Correlation coefficient, (ρ_{XY})	Element no., (N)	Correlation coefficient, (ρ_{XY})
20	0.966051	200	0.999911
40	0.994154	250	0.999953
60	0.997926	300	0.999974
80	0.999021	400	0.999991
100	0.999441	500	0.999997
150	0.999805	800	1.000000

FIGURE 7: Maturation of dense clay with and without perforated tubes for 12 and 48 hours, respectively.

Compared with the result with 800 elements, the values of the correlation coefficient for the maturation curves are calculated and given in Table 1. Since the correlation coefficient is higher than 0.9999, the simulation with 200 elements is considered to have converged.

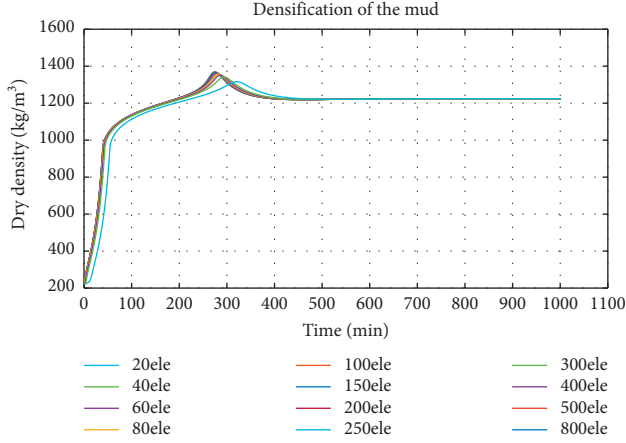*5.2. Verification of the Numerical Model.* In order to validate the numerical model, it is expected to show that the simulation of the laboratory-scaled clay seals agrees with the experimental results. Although the retardation of the maturation process caused by the perforation of the tubes cannot be readily modelled, it is shown in the following that it is still possible to assess its impact.

5.2.1. Maturation Influence by Perforated Tubes. Two series of laboratory tests were performed with the duration of 12 and 48 hours. In each of the series, two tests were performed, one test with and one test without the perforated tube for the same maturation time. The results are presented in Figure 7. Considering the area between the maturation curve and the initial horizontal line, one can calculate the volume obtained if the area is rotated around the dry density axis as $V_{\text{with--12 h}}$, $V_{\text{with--48 h}}$ and $V_{\text{without--12 h}}$, $V_{\text{without--48 h}}$ for maturation in 12 and 48 hours with and without perforated tube, respectively. Building relationships of the volume of rotation as a function of time for $V_{\text{with--12 h}}$ and $V_{\text{with--48 h}}$, as well as $V_{\text{without--12 h}}$ and $V_{\text{without--48 h}}$, one obtains relationships between V_{with} with time T_{with}, and V_{without} with time T_{without}. Assuming that maturation is synchronous for the experiment and computation when V_{with} is equal to V_{without}, one arrives at the following relationship of the maturation time for the cases with and without a tube:

$$T_{\text{without}} = 0.013112 * T_{\text{with}}^{1.309506}, \tag{21}$$

where T_{with} and T_{without} represent the maturation time in the experiment and numerical simulation in hours, respectively. With the value of maturation time in the experiment, the corresponding time in computation at the same maturation

state is calculated utilizing equation (21). The results are collected in Table 2.

5.2.2. Comparison with Experimental Results. Based on the relationship of maturation time T_{with} and T_{without}, as well as the values of the time in Table 2, the dry densities of maturated clay in numerical simulations are compared with the corresponding dry densities from experimental results (Figure 8). In Figure 8, the blue curve, which presents the computed result with 200 elements and the mud (regarded as one element), consists of 201 data points. Each point represents one element, providing information on the dry density and the position in the seal for the maturation time studied. To determine the dry density in the experiments, the dense clay sample to be analysed after hydration was divided in the radial direction into hollow cylindrical pieces with the same thickness. Therefore, each point in the experimental red curve represents the mean dry density of one piece of clay in its radial position.

The black curve is plotted based on the simulated result. The curve consists of 8 points, each representing the average of 25 computed elements, in order to achieve the same number of data points as in the experimental result. The orange triangle point, on the right on the blue curve, represents mud. In the simulation, the thickness of the mud changes with the maturation of the dense clay elements, so the position of the orange point changes as well. In contrast,

TABLE 2: Maturation time in experiment compared with time in numerical simulation to reach the same maturation state.

Time in experiment, (T_{with}, h)	Time in simulation, $(T_{without}, min)$
6	8
12	20
24	50
48	125
96	310
1 (year)	10^5

(a)

(b)

(c)

(d)
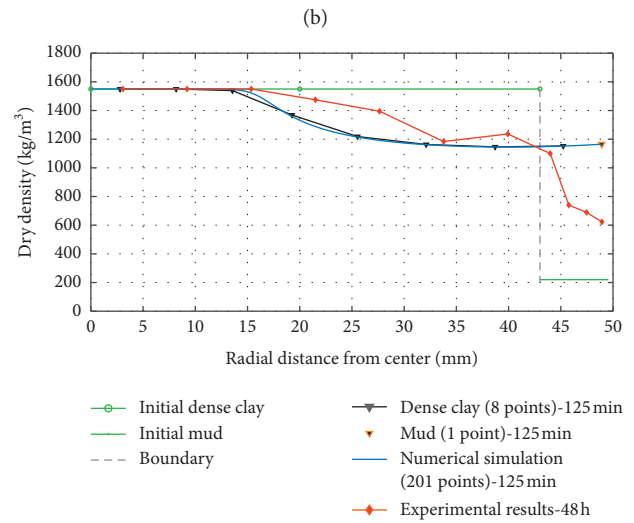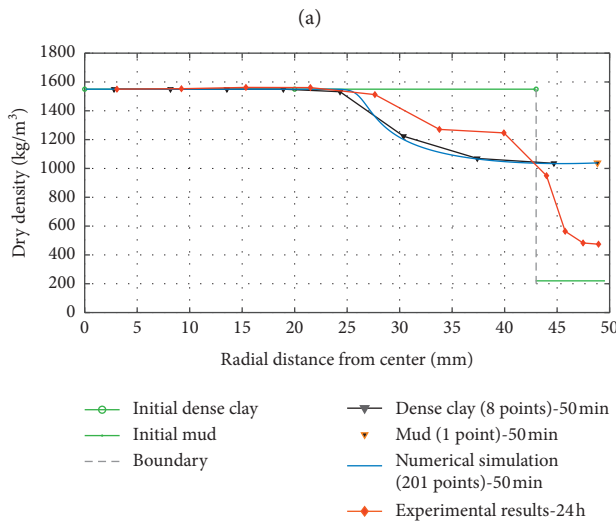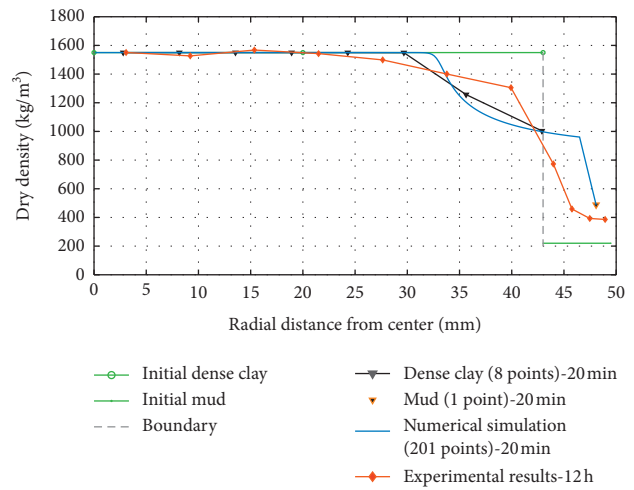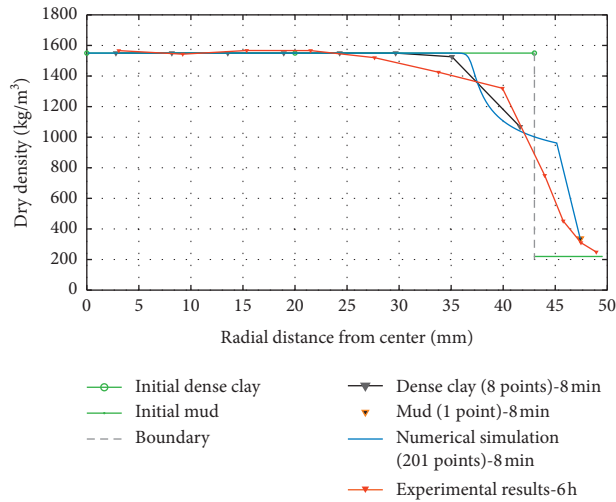
FIGURE 8: Continued.

(e)

(f)
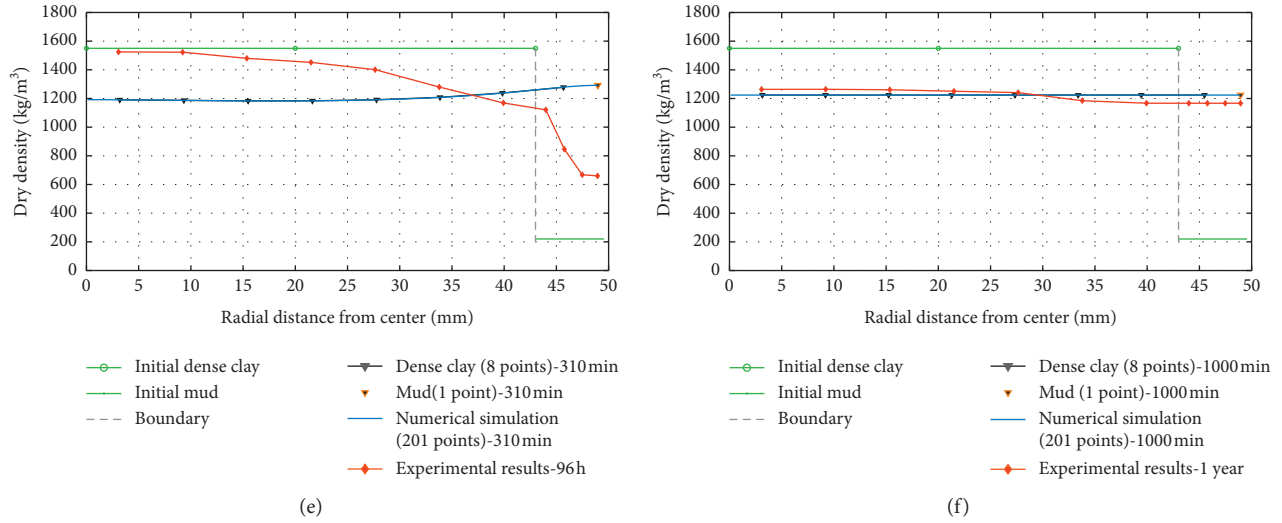
FIGURE 8: Comparison of clay maturation in numerical modelling and laboratory experiments. In Figure 8(f), the simulation results of 1000 minutes were used for comparison since end of maturation was reached. (a) Maturation with 6 h (experiment), 8 min (simulation). (b) Maturation with 12 h (experiment), 20 min (simulation). (c) Maturation with 24 h (experiment), 50 min (simulation). (d) Maturation with 48 h (experiment), 125 min (simulation). (e) Maturation with 96 h (experiment), 310 min (simulation). (f) Maturation with 1 year (experiment), 1000 min (simulation).

the tested mud in the experiments contains some expanded dense clay since the same thickness of mud as the initial thickness was tested without any regard to the maturation process. Therefore, the experimentally determined dry density of the mud becomes increasingly incorrect as the maturation process progresses. The comparison in Figure 8 should mostly be focused on the dense clay part to the left.

Figure 8 indicates that the numerical model works in a good way since the simulated results agree quite well with the experimental results for 6, 12, 24, and 48 hours and one year of maturation. However, for the maturation time of 96 hours in the experimental test in Figure 8(e), the difference between the simulated and the experimental results is considerably large. It seems that the numerically simulated results are ahead of the experimental results in the maturation process. A possible reason for this discrepancy is the relationship equation (21), which is based on the limited number of experimental tests resulting in this equation. The agreement between the simulated and the experimental results in Figure 8, in particular Figure 8(e), is expected to improve if the relationship given in equation (21) is developed further based on more laboratory tests.

5.3. Maturation Progress of Clay Seals. The maturation process of clay seals includes both water transport and clay migration. Water transport is generated by suction differences. Water is absorbed in the interlamellar space of the crystals, as a result of the hydration of the exchangeable cations and the osmotic phenomena [11]. The clay migration is generated by the expansion of the crystal layers and the microstructural reorganisation.

From the result of the numerical simulation (with 200 elements), the maturation progress of the clay seals can be studied in Figure 9. A water content ratio, corresponding to

the colour bar in Figures 9(a)–9(c), 9(g)–9(i), 9(m)–9(o), is introduced for visual representation of the water transport in the mud and dense clay by colour shadings. The water content ratio is normalised between 0 and 1 and is calculated by

$$\text{water content ratio} = \frac{w - w_{\text{dense clay}}^{\text{initial}}}{w_{\text{mud}}^{\text{initial}} - w_{\text{dense clay}}^{\text{initial}}}, \quad (22)$$

where w is the water content in the element, $w_{\text{dense clay}}^{\text{initial}}$ is the initial water content of the dense clay, and $w_{\text{mud}}^{\text{initial}}$ is the initial water content of the mud. The value 0 in the colour bar thus represents the same water content as the dense clay has initially, while 1 denotes the same water content as the mud has initially. A higher value of the water content ratio means higher water content.

At the beginning of the maturation process, the water content in the area of the interface of mud and dense clay is very high. Therefore, water moves rapidly into the part of the dense clay that is very close to the mud (Figures 9(a)–9(c)). With water gradually spreading into more elements, the dense clay becomes wetter but will not be as water-rich as the elements next to the mud in the earliest stage (Figures 9(g)–9(i)). As the maturation progresses, the difference in water content between the elements will be less significant as in the initial stage. The clay seal becomes increasingly more uniform, and the maturation process slows down gradually since the water-driving suction becomes lower with time (Figures 9(m) and 9(n)). After a long time, the water content is evenly distributed in the entire seal, and homogenization is then achieved (Figure 9(o)).

In the modelling, the solid mass in mud and clay elements is conserved during the process. Because of the
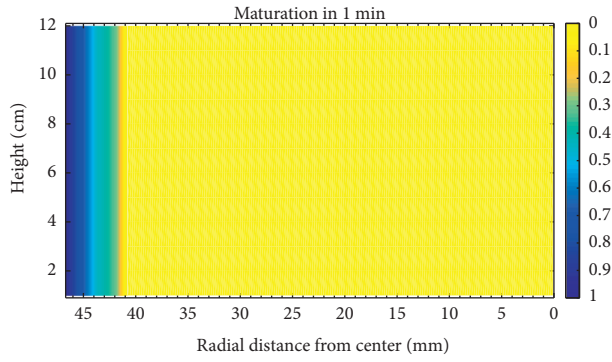
(a)
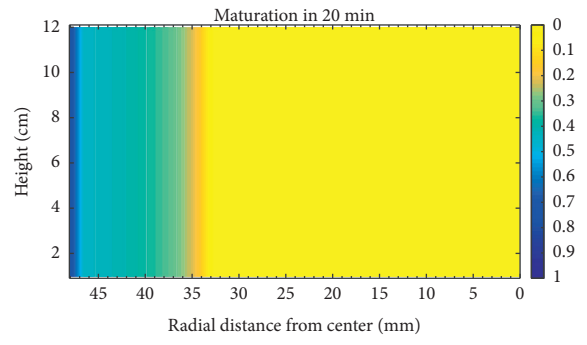
(b)
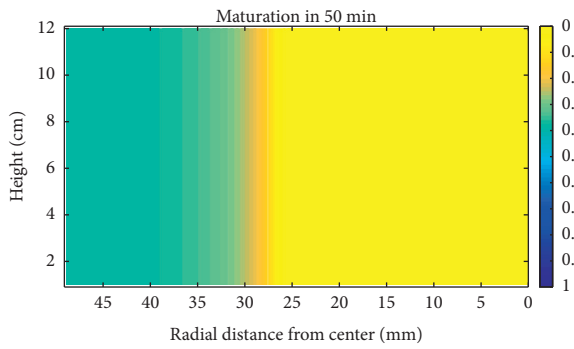
(c)
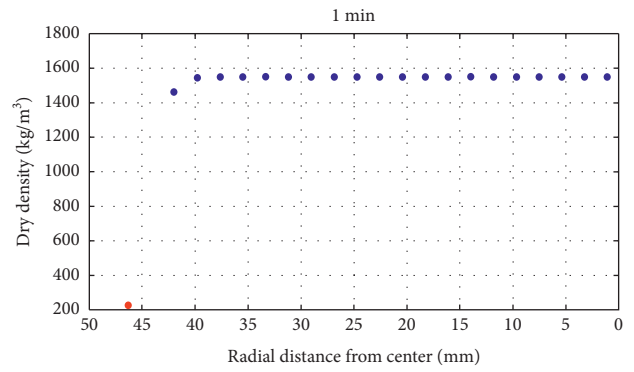
(d)
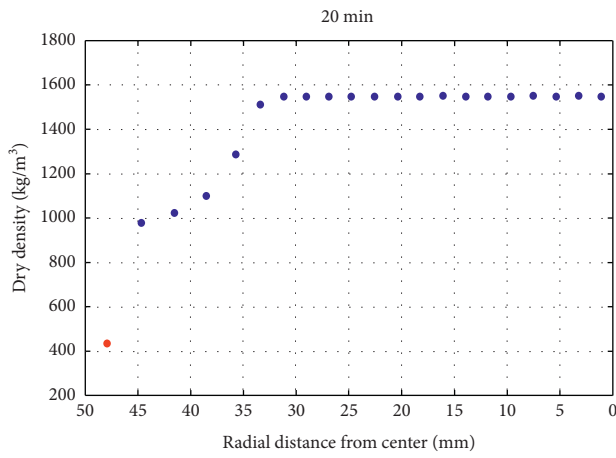
(e)
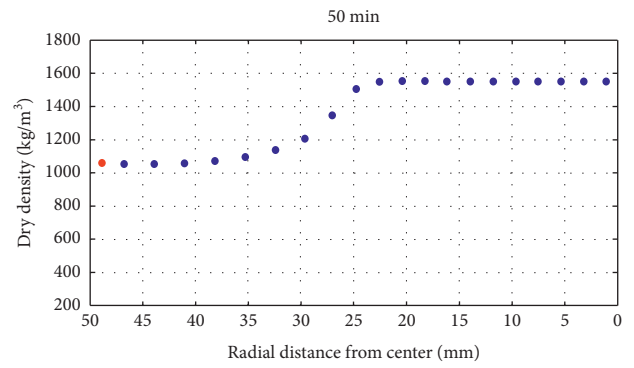
(f)

FIGURE 9: Continued.

(g)

(h)

(i)

(j)

(k)

(l)

(m)

(n)

Figure 9: Continued.

(o)

(p)

(q)

(r)
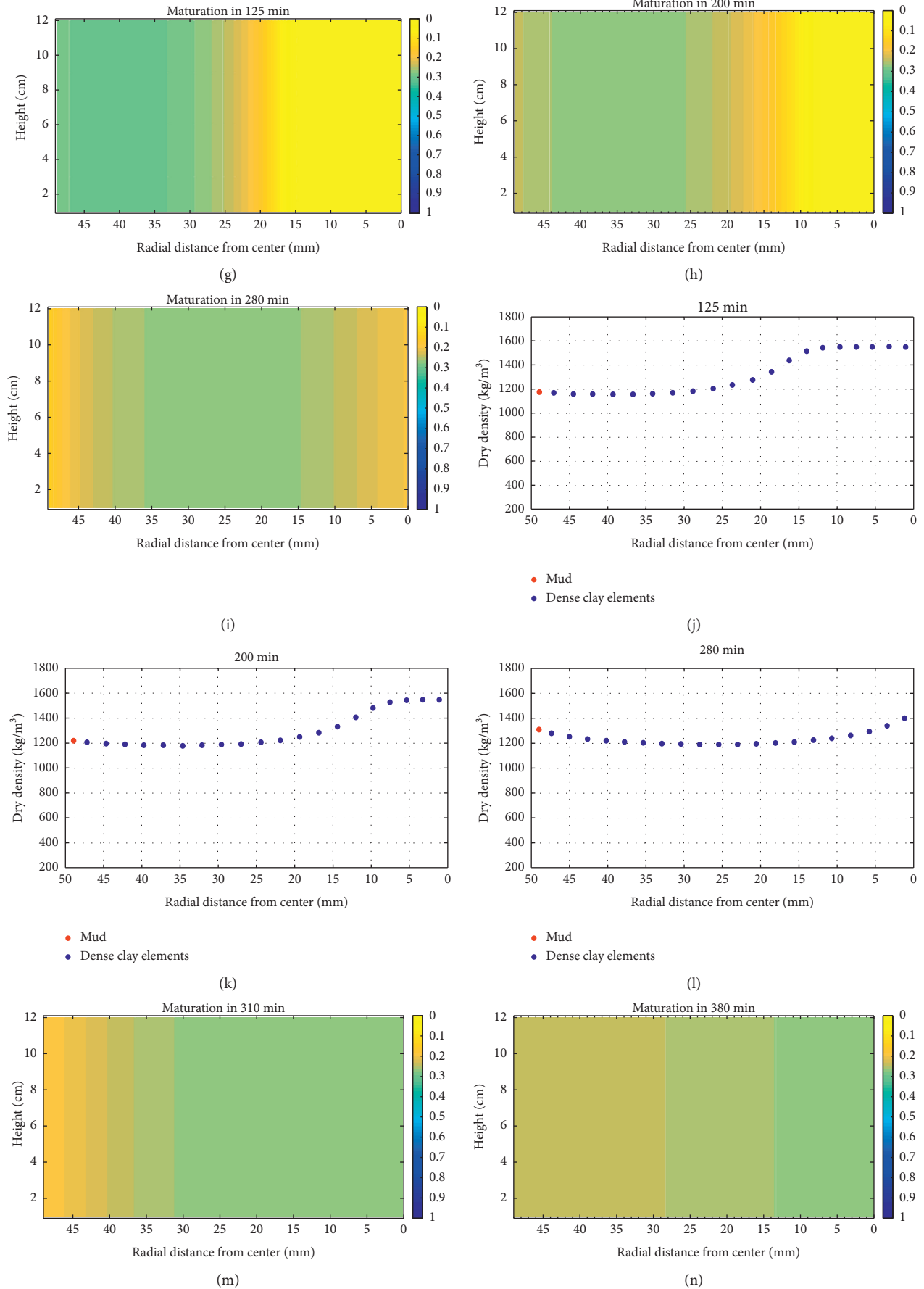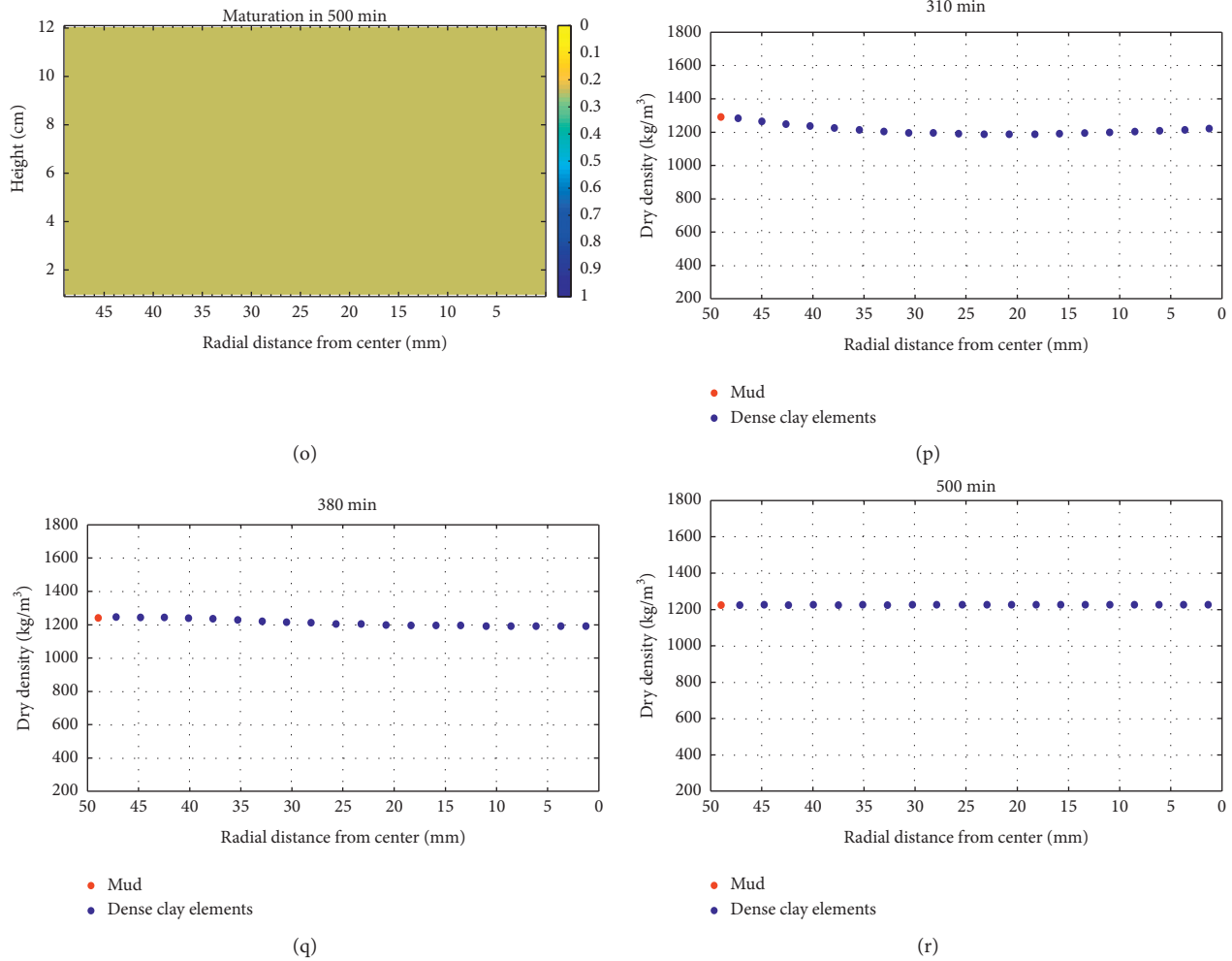
Figure 9: Simulated maturation process of the clay seals. (a, b, c, g, h, i, m, n, o) The water transport in clay as a function of maturation time. (d, e, f, j, k l, p, q, r) The clay migration, presenting density changes of different parts of the clay seal as a function of time.

expandability of smectite clay, the variation of the dry density is associated with a change in volume of the elements, which remain fully saturated throughout the maturation process. Initially, the mud loses a substantial volume of water and densifies rapidly until it reaches a density that approaches that of the adjacent elements. During this period, the red mud-dot in Figures 9 changes its position gradually and moves closer to the filter boundary (Figures 9(d)–9(f)). Simultaneously, as shown by the blue dots, the dense clay elements that are located close to the mud absorb water, expand, and move towards the mud.

Along with more elements closer to the centre of the sample gradually undergoing expansion, the swelling forces further compress the mud and some elements close to the mud. They will temporarily become even denser than some elements in the more central region (Figures 9(j)–9(l)). With time, elements in the central part become less dense than the mud and the elements in its vicinity (Figures 9(p) and 9(q)). Water is sucked from the softer parts of the clay by the denser parts. The volumes of mud and elements slightly adjust until they ultimately obtain the same density (Figures 9(r)).

6. Numerical Modelling of the Evolution of Clay Seals in a Real Borehole

In a VDH for HLW disposal, the upper 500 m to 2000 m part (Figure 1) is tightly sealed with smectite-rich clay which is also the case for the lower 2000 m part, where the containers are filled with clay and nuclear waste canisters. In this section, the proposed numerical model is applied for real borehole cases. In the numerical model, no attention is paid to the impact of the heat production caused by radioactive decay. This implies that the numerical model in its present form might only be valid for the upper part of the borehole.

Juhlin and Sandstedt [12] and Pusch [6] have proposed a VDH diameter of 80 cm for the borehole and 60 cm for the tubes with clay-embedded HLW canisters, or alternatively 50 cm for the tubes if a borehole casing is required. The maturation of clay seals in a full-scale borehole with the diameter of 80 cm/60 cm for borehole/clay plugs, termed "real Case 1," and 80 cm/50 cm, termed "real Case 2," has been numerically simulated with the model. The result from the simulations is presented in Table 3 and Figure 10.

TABLE 3: Numerical simulation of maturation in reference to real VDH with Holmehus clay.

| Case | Initial dry density (dense clay/mud) (kg/m^3) | End of process | | | | Case | Initial dry density (dense clay/mud) (kg/m^3) | End of process | |
		Dry density (clay seals) (kg/m^3)	Time (days)	k (m/s)	U_e (MPa)			Dry density (dense clay/mud) (kg/m^3)	Time (days)
1	1550/222	969	78	$4.06E-10$	0.002	2	1650/222	(910–960)/450	43
	1650/222	1025	74	$2.12E-10$	0.229		2000/222	(878–960)/960	75
	1800/222	1112	104	$8.89E-11$	0.570		2250/222	1014/1014	137
	1900/222	1166	155	$5.18E-11$	0.806		1900/245	(891–960)/933	57
	1900/245	1178	140	$4.59E-11$	0.861		2000/245	(879–960)/960	78
	1900/490	1283	277	$1.61E-11$	1.389		1900/490	1042/1042	85
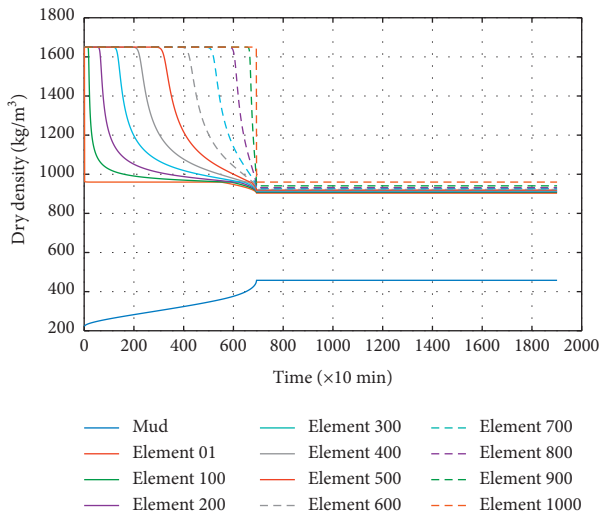
FIGURE 10: Maturation of clay seals in real Case 2. Plotting with mud and every 100th element.

For "real Case 1" (Table 3), with the 80 cm/60 cm design of the borehole repository, a suitable initial dry density for Holmehus clay plugs is more than 1800 kg/m^3, assuming the initial dry density of the mud is 222 kg/m^3. The maturation process will take more than 100 days. If the initial dry density of the mud is high, e.g., around 490 kg/m^3, the time to reach homogenization will be much longer.

For "real Case 2," with an initial dry density of 222 kg/m^3 for the mud and 1650 kg/m^3 for the dense Holmehus clay, the migration of solids is not fast enough to densify the mud early because of the high ratio between the thickness of mud and dense clay. As shown in Figure 10, the ultimate dry density of the mud is around 450 kg/m^3, while that of the dense clay is 910–960 kg/m^3.

The maturation progress ends when the dry density of Holmehus clay reaches 960 kg/m^3 since the water suction potential of the clay with this dry density is extremely low. The heterogeneous condition lasts until the initial dry density of dense clay is as high as 2000 kg/m^3, in which case the mud and clay plugs become relatively uniform with a dry density around 960 kg/m^3 after about 75 days. With a higher initial dry density of 490 kg/m^3 for the mud and 1900 kg/m^3 for the dense clay, the dry density of the clay seals is predicted to be 1042 kg/m^3 after 85 days. However, with the high density of the mud, a significant increase in shear resistance for installing clay packages is expected. To speed up the maturation of the entire clay system and to achieve ultimate homogeneous sealing status, it would be preferable to use a more smectite-rich clay than Holmehus clay or to install it in an incompletely saturated form.

7. Concluding Remarks

The goal of this paper is to present a numerical model for the simulation of the maturation of clay seals. It can be concluded that the proposed numerical model works well in describing the maturation process that takes place in the smectite clay barrier in the storage of spent reactor fuel in very deep boreholes.

The numerical model takes into account neither the influence of the perforated tube on the maturation process nor the supercontainer surrounding the dense clay. In the present study, this influence was considered by formulating a relation between the maturation times with and without a perforated tube. This relation was based on two series of laboratory tests. It is believed that this relation could be improved by increasing the number of laboratory tests.

The numerical model is based on the assumption that both the dense clay and the mud are fully saturated during the maturation process. This is probably the case in most practical situations because of the high pore pressures that exist at the great depths in the storage concept. In any case, if non-saturated conditions are to be modelled, the numerical model needs to be modified.

By performing numerical simulations for various clay types, as well as using different combinations of dimensions and initial densities of mud and dense clay, the maturation process and the end result could be studied theoretically. In the storage concept, it is important that the boreholes become properly sealed to avoid radioactive waste leakage. It is also important that it is possible to install the supercontainers through the soft mud in the deep boreholes in a practical way. Whether the boreholes become properly sealed depends on reaching full homogenization on the end densities in the seals and on the maturation time. To be able to install the supercontainers, it is important that the maturation process does not go too fast. If that is the case, the clay in the seals could expand against the borehole walls, which would increase the shear resistance, and make the installation of the supercontainers difficult. All practical

issues mentioned above serve as examples of what can be further studied by use of the numerical model.

Data Availability

The experimental image data used to compare with the findings of this study are from the author Ting Yang's previously reported studies.

Conflicts of Interest

The authors declare that there are no conflicts of interest regarding the publication of this paper.

Acknowledgments

References

[1] R. Pusch and T. Yang, "Long-term performance of contacting concrete and smectite clay in deep disposal of highly radioactive waste," *International Journal of Sustainable Development and Planning*, vol. 11, no. 5, pp. 740–750, 2016.

[2] L. Börgesson, A. Dueck, and J. Hernelind, "Bentonite homogenisation—modelling of homogenisation processes in bentonite buffer materials in repositories"" *Journal of Earth Sciences and Geotechnical Engineering*, vol. 9, pp. 133–163, 2019.

[3] C. Andersson, I. Bárcena, N. Bono et al., "Full-scale testing of the KBS-3V concept for the geological disposal of high-level radioactive waste," Technical Report FIKW-CT-2000-00055, European Commission, Brussels, Belgium, 2005.

[4] H. K. Sandstedt, C. Wichmann, R. Pusch, L. Börgesson, and B. Lönnerberg, "Storage of nuclear waste in long boreholes," Technical Report TR 91-35, SKB, Solna, Sweden, 1991.

[5] R. Pusch and R. N. Yong, *Microstructure of Smectite Clays and Engineering Performance*, Taylor & Francis, Westminster, UK, 2006.

[6] R. Pusch, *Geological Storage of Radioactive Waste*, Springer, Berlin, Germany, 2008.

[7] T. Yang, R. Pusch, S. Knutsson, and X. Liu, "Lab testing of method for clay isolation of spent reactor fuel in very deep boreholes," *Procedia Earth and Planetary Science*, vol. 15, pp. 152–158, 2015.

[8] J. K. Mitchell and K. Soga, *Fundamentals of Soil Behavior*, Wiley, Hoboken, NJ, USA, 3rd edition, 2005.

[9] T. Forsberg, R. Pusch, T. Yang, and S. Knutsson, "Clay/water mixture by use of nano-sized water droplets "dry-water"" in *Proceedings of the 19th International Conference on Soil Mechanics and Geotechnical Engineering*, Seoul, Republic of Korea, 2017.

[10] M. E. Harr, *Groundwater and Seepage*, Dover Publications, New York, NY, USA, 1991.

[11] T. Yang, S. Knutsson, and X.-D. Liu, "Swelling properties and permeability of expandable clays of potential use for nuclear waste disposal," *Journal of Earth Sciences and Geotechnical Engineering*, vol. 6, no. 2, pp. 49–61, 2016.

[12] C. Juhlin and H. Sandstedt, "Storage of nuclear waste in very deep boreholes: feasibility study and assessment of economic potential. Part I: geological considerations. Part II: overall facility plan and cost analysis," Technical Report TR 89-39, SKB, Solna, Sweden, 1989.

Research Article

Experimental Research on Mechanical Property and Environmental Safety of an Industrial Residue Waste Subgrade Material

Yangpeng Zhang,[1,2,3,4] **Jianping Xiong,**[1,2,3,4] **Qinglin Li** [ORCID],[5] **and Jiuhui Cui**[6]

[1]*Guangxi Transportation Science & Technology Group Co., Ltd., Nanning 5300007, China*
[2]*Guangxi Key Lab of Road Structure and Materials, Nanning 5300007, China*
[3]*Research and Development Center on Technologies, Nanning 5300007, China*
[4]*Materials and Equipment of High-Grade Highway Construction and Maintenance Ministry of Transport, Nanning 5300007, China*
[5]*College of Water and Architectural Engineering, Shihezi University, Shihezi 832003, China*
[6]*China Bluestar Chengrand Co., Ltd., Chengdu 610000, China*

Correspondence should be addressed to Qinglin Li; liql1150142@163.com

Received 13 June 2020; Accepted 24 July 2020; Published 12 August 2020

Guest Editor: Guocheng Lv

In order to promote the sustainable use of oil shale residues, a novel subgrade material (SOF) composed of silty clay, oil shale ash residue, and fly ash was developed. The aim of this paper is to study the mechanical behavior and environmental impact of SOF, which is regarded as the safety assessment and prediction for the application of this novel material. To this purpose, the road performance, dynamic properties, and environment impact tests are conducted. In terms of the road performance, the test results of SOF exceed the standard requirement, especially for CBR (California bearing ratio), which can maintain good performance at bad conditions of low compaction degree and being soaked for a long time. The dynamic properties under cyclic loadings are better than most of original and stabilized soils. The shear strength parameters and the anti-damage mechanism are also discussed; research results show that the friction of SOF mostly contributes to shear strength under high stress conditions, while its cohesion tends to play a more important role under low stress conditions. According to the deformation variation, the accumulation settlement of SOF under vehicle loadings after several years is predicted, which is far lower than the limit of expressway and Grade I highway. Furthermore, the chemical stability and toxicity of SOF leachates are environmentally friendly, which are in line with the benchmarks of Class II surface water and Class III ground water. All the experimental results manifest that SOF used as subgrade filling has good application potential and safety.

1. Introduction

As the nonrenewable fossil energy like petroleum, gas, and coal, the utilization of oil shale has a history of nearly 200 years in terms of distribution situation, basic properties, extraction technology, and applied research [1]. With higher ash and oil content than coal, oil shale is processed into gasoline, diesel, and burning oil and is co-exploited with coal as associated resources. In China, the detected oil shale reserves of approximately 72 billion tons rank among the top in the world. According to the preliminary exploration by

the government [2], a national oil shale reserve distribution map is drawn in Figure 1. Due to abundant oil shale resources, there are more than 10 oil shale retorting companies in service. Therefore, a large amount of oil shale waste residue has also been generated with the continuous development. From incomplete statistics, China's annual production of shale oil reaches 700,000 tons with by-product wastes of 1.75 million tons [3, 4].

The recycle of oil shale wastes mainly focuses on the aspects of construction materials, fertilizer, and soil stabilization, which follows the application experience of fly ash,

Jilin province has the highest oil shale reserve all over the China. Several large and comprehensive utilization oil shale industry corporations are located here.
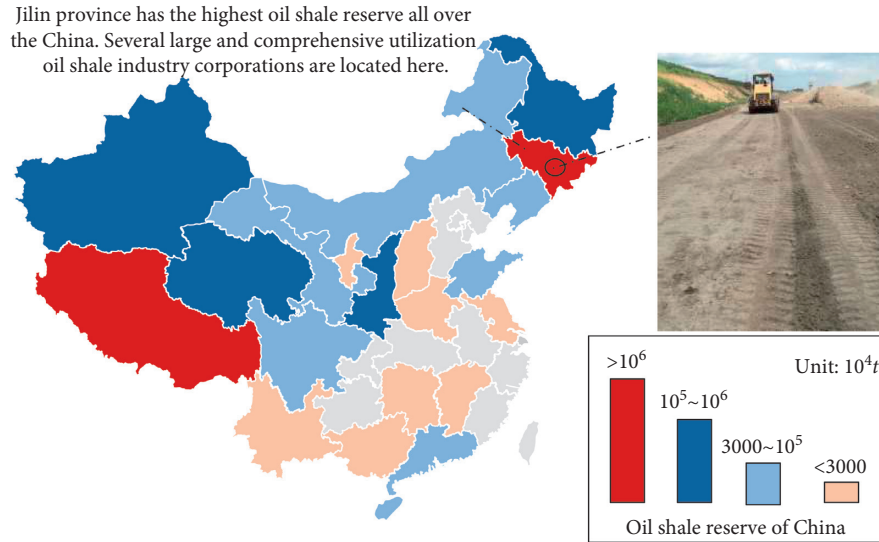
FIGURE 1: Distribution of oil shale resources in China.

mineral slags, and so on [5, 6]. Recently, with the rapid development of China's highway, industry-industrial wastes have been widely used in road structures. Taking the reuse of waste tires as an example, the processed crumb rubbers by cutting and grinding tires have been applied in asphalt and related road products. Similar applications are also conducted for fly ash and slags. Compared with the utilization of other wastes, the current application of oil shale wastes is in the early stage. Azzam and Al-Ghazawi [7] added oil shale wastes into hot mix asphalt based on Superpave design method. The result indicated that the mixed asphalt possessed favorable performance in aspects of resilient modulus, creep, and fatigue tests. Wang et al. [8] investigated the positive impact of oil shale wastes on the temperature properties of asphalt mastics and observed the difference between oil shale ash and semi-coke when they were used as the filling material of asphalt mastics.

Subgrade is a broad field for the application of oil shale wastes. Turner stabilized soils by OSA (oil shale ash) and established the corresponding database of engineering properties [9, 10], and it was also found that the combination of OSA and limestones showed better road performance. To dispose the byproduct OSA of Narva Power Plant, Koroljova and Pototski [11] added the residues to soft peat soils to replace the traditional addition of cement. Since 2013, this technology has been widely used for road construction in swamp areas of Estonia [12]. The group of Jilin University also carried out a comprehensive research on the modification of OSA as subgrade materials; an economical and efficient method for the utilization of OSA has been proposed after a series of tests, including basic physical characteristics, material proportion, and mechanical properties [13–15].

In view of the huge advantages of this novel filling, authors and the local transportation department are conducting an experimental road to accumulate more experience and foundation for further application. As a matter of fact, the process of development, application, and promotion for a new subgrade material requires a long-term verification on

performance, economy, and safety. To a certain extent, safety assessment holds the first priority. For the filling of SOF, even though a systematic research has been conducted, there are still significant and necessary works worth studying, for example, the mechanical response and deformation characteristics under actual vehicle loadings and the evaluation of durability and chemical composition stability, which are also the purpose and main contents of this paper.

Road performance is the earliest but the most important factor in the evaluation of the feasibility of subgrade. It can be analyzed from CBR, resilient modulus, unconfined compressive tests, and so on. Mohajerani et al. [16] researched the road performance of modifying the biosolid wastes of Melbourne East and West Plant by lignite fly ash based on a series of CBR tests. Deb and Narnaware [17] adopted the unconfined compressive strength to determine the effectiveness of fiber on clay. The recognized mixing ratio of 1 : 2 of fly ash on soil is also found by means of road performance tests. With the deep understanding of road structure and failure mechanism, more property of materials has been concentrated on, such as mechanical strength and deformation characteristics. Murthy et al. investigated the dynamic modulus and damping ratio of the cement-stabilized soils by triaxial tests [18]. Research results showed that the microporous soils, with the addition of cements, possessed high dynamic strength and better resistance to deformation. The similar conclusions had been got by Baig et al. [19]. To discuss the deformation characteristics of saturated friable sand modified by silica slurry, Gallagher and Mitchell [20] conducted parallel cyclic vibrations with different addition amounts and stress conditions. They obtained the positive results for total axial deformation and liquefaction strength. Based on summarizing the previous research, the above evaluation methods of the dynamic characteristic of subgrade have been mature and effective.

As mentioned above, the objective of this study is to perform the safety assessment of SOF, which is regarded as the vital prediction and reserved information for the

Figure 2: Preparation of test samples.

construction of experimental road. To this purpose, a series of experiments of CBR, static resilient modulus, dynamic strength, and deformation are conducted to investigate the road performance and mechanical properties of modified soils. Further analysis from the aspects of shear failure and accumulation deformation is also conducted. Finally, to master the environmental suitability of this novel filling material, a comprehensive evaluation of chemical composition stability and toxicity is performed.

2. Material Properties and Experimental Methods

2.1. Physical Properties of SOF. The material of SOF is made by evenly mixing silty clay, oil shale ash, and fly ash at the mass ratio of 2 : 2 : 1, and before making testing samples, oil shale ash, silty clay, and fly ash samples were dried in an oven at 105–110°C for 24 h and then cooled at room temperature in a desiccator. The sample preparation of road performance test is shown in Figure 2, and the preparation process follows the impact molding method [21]. Silty clay is the typical bad filling in northeast China because of its undesirable water instability. Oil shale ash is completely provided by the nearby oil shale industrial park, which is collected by the combustion of oil shale ores. The range of particle size 0–5 mm guarantees the activity to be used in construction material improvement, fertilizer production, and stabilization of soft soils. The fly ash used in this study is classified into F Class with the content of CaO of 0.92%, $SiO_2 + Al_2O_3 + Fe_2O_3$ of 88.64%, and the loss on ignition of 3.19%.

2.2. Experimental Methods

2.2.1. Road Performance Test. In the specification of design for highway subgrades [22], road performance of CBR and resilient modulus are mandatory indexes to evaluate the serviceability of subgrade materials. Road materials strength tester and lever tester are adopted to measure the above two parameters, respectively. According the national standard [21], testing specimens (the height of 170 mm, the diameter of 76 mm) are produced by heavy compaction method at the degrees of 96% and 100%. Three parallel specimens are also designed for each test condition. Moreover, for the CBR tests, the test specimens are soaked with water for 96 h in order to simulate the worst service environment.

2.2.2. Dynamic Properties Test. For subgrade materials, dynamic properties are more available for assessing the application safety in practical engineering, especially for constructions in seasonally frozen regions. So, the strength and deformation characteristics related to dynamic loadings are tested in this part. The dynamic triaxial testing system, made in Gansu, China, is used in this part. Cylindrical specimens with a diameter of 39.2 mm and a height of 80 mm are prepared according to the national standard [21]. To make the results more realistic for the site, the states of saturated water and F-T (freeze-thaw) cycles are also designed.

In testing strength characteristics, all specimens are brought to outer vacuum saturation for 24 h and back-pressure saturation in device. An initial axial stress is added to consolidate specimens with a factor of 1.9. The confining pressure varies from 50 to 150 kPa, and the vibration frequency is set as 1 Hz. Furthermore, several parallel experiments are conducted for specimens after 1, 3, 5, and 7 F-T cycles. A F-T cycle means the test specimen is frozen at the temperature of −15°C and then thawed at the temperature of 15°C for 24 h. During this process, the specimens are sealed with plastic film to reduce the moisture change and external impact. There is another long-term deformation experiment to test the deformation characteristics of SOF. The specimens are performed at the optimum moisture and dry

density. All experiment procedures are carried out in the confining pressures of 100 kPa with the vertical stress ratio of 0.5 and 1.5. The confining pressure of 100 kPa is chosen because it is the closest situation to the application engineering. Similar tests are repeated for specimens after different F-T cycles as well.

2.2.3. Chemical Composition Test. Road performance and mechanical property are the essential premise to judge the serviceability of subgrade filling. However, the safety assessment of subgrade filling on the surrounding environment also cannot be ignored. The potential threats of SOF on the environment are related to its chemical composition and precipitated trace elements after immersion in water. In this part, the detailed analysis of the composition of SOF and its leachates are conducted at Testing Center of Jilin University; the XRD (x-ray diffraction), FTIR (Fourier transform infrared spectroscopy), and ICPMS (inductively coupled plasma-mass spectrometry) are adopted in the analysis.

3. Results and Discussion

3.1. Road Performance of SOF. The results of CBR and resilient modulus for SOF are listed in Tables 1 and 2. In Table 1, the CBR values of SOF at the compaction degree of 100% are slightly higher than those at the degree of 96%. The same phenomenon is reflected in the measured resilient modulus in Table 2. This can be attributed to the denser structure of specimens during forming process. The water absorption and swelling capacity of 6.92% and 5.47% at the maximum compaction condition are lower than the results of 7.62% and 5.84% at the compaction degree of 96%, which indicates the small distinction in structure. It also should be noted that the CBR values of specimens treated by soaking decline sharply by 46.2% and 45.4%. The result proves the effect of bad service environment of subgrade on the road performance.

For subgrade materials, explicit standard is required for the road performance. For expressway and first-class highway, the regulated minimum CBR values of roadbed and embankment are 5%~8% and 3%~4%, respectively. The minimum resilient modulus of upper roadbed for cement concrete and bituminous pavement at the extremely heavy or heavy traffic load is 80 and 70 MPa, respectively. Taking into account the compaction difficulty in actual construction, the results of CBR and resilient modulus at the compaction of 96% are used as the evaluation index of road performance for SOF. Both CBR and resilient modulus are far higher than the specified standard, especially for CBR. The good performances of SOF are related to the stable structure formed by fly ash and oil shale ash, which has been mentioned in a previous study [13]. Thus, the road performance of SOF is considered safe even at some undesirable conditions.

3.2. Dynamic Strength Characteristics. Dynamic failure strength σ_s is the most acknowledged parameter to evaluate the dynamic properties of soils. In this paper, σ_s is

defined as the half value of σ_d when the axial strain exceeds 5%. The relationship curves of σ_s and $\log(n)$ (where n represents the vibration numbers of failure) of SOF under the pressures of 50, 100, and 150 kPa are drawn in Figure 3. As shown in Figure 3, σ_s possesses higher values when the confining pressure is higher, and is a good linear decrease relation with $\log(n)$. The higher the confining pressure, the faster the decline rate. For example, the gradient of 111.44~125.44 under σ_c of 150 kPa is nearly 3.56~4.43 times that under σ_c of 50 kPa, which indicates that the effect of confining pressure on the failure strength is gradually weakened as the vibration numbers increase. The action of F-T cycles is another important factor influencing the failure strength. Comparing the results under the same testing conditions, σ_s decreases sharply after F-T cycles especially for the situation of high confining pressure, and the linear relationship between σ_s and $\log(n)$ is still obvious after F-T cycles. Furthermore, from the perspective of numerical values, the dynamic properties under cyclic loadings are better than those of most of original and stabilized soils [23, 24]. Therefore, the filling material of SOF can be classified as a high-strength subgrade material.

To understand the dynamic strength characteristics of SOF more deeply, shear strength parameters including dynamic cohesion c_d (kPa) and dynamic inter friction angel φ_d (°) can be obtained by Mohr–Coulomb Curve. Just as shown in Figure 4, σ_{c1}, σ_{c2}, and σ_{c3} are confining pressures of 50, 100, and 150 kPa, respectively; σ_{a1}, σ_{a2}, and σ_{a3} are the axial failure principal stress (kPa) corresponding to the above three confining pressures, respectively. According to the experiment schedule, the value of axial failure principal stress can be calculated as follows:

$$\begin{aligned} \sigma_d &= 2\sigma_s, \\ \sigma_a &= \sigma_1 + \sigma_d, \\ \sigma_i &= k \times \sigma_c, \end{aligned} \tag{1}$$

where σ_i is the initial static axial stress on the specimens (kPa) and k is the consolidation coefficient of 1.9. Based on the theory of ultimate equilibrium, the failure envelope, which is the common tangent of three Mohr circles, can be drawn. Then, c_d and φ_d are obtained by measuring the intercept and slope of the failure envelope by Lambe plane (s, t) method. Taking into account the significant influence of the physical property and experimental stress condition on specimens, the parameters of c_d and φ_d at different failure points and F-T cycles are separately calculated in this part. The relation functions of $t = (\sigma_a - \sigma_c)/2$ and $s = (\sigma_a + \sigma_c)/2$ are plotted in Figure 5. The calculated shear strength parameters of SOF under different testing conditions are listed in Table 3.

From Table 3, some valuable conclusions can be obtained. The dynamic friction angle φ_d and cohesion c_d vary with the vibration numbers of failure which proves the significant influence of stress conditions on specimens. As the failure number increases, the parameter of φ_d decreases whereas c_d increases. It means the friction mostly

TABLE 1: Results of CBR test.

CD[1] (%)	No	Water absorption and swelling capacity				CBR values			
		WA[2] (%)	Average/SD[3] (%)	SI[4] (%)	Average/SD[3] (%)	CBR$_s$[5] (%)	Average/SD[3] (%)	CBR$_{ws}$[6] (%)	Average/SD[3] (%)
100	1	7.01		5.42		41.79		79.52	
	2	6.98	6.92/0.14	5.51	5.47/0.05	44.11	42.37/1.53	78.65	78.74/0.73
	3	6.76		5.48		41.21		78.06	
96	1	8.12		5.92		38.86		71.38	
	2	7.34	7.62/0.43	5.83	5.84/0.07	38.39	38.41/0.44	69.14	70.16/1.13
	3	7.41		5.78		37.99		69.96	

[1]CD = compaction degree; [2]WA = water absorption; [3]SD = standard deviation; [4]SI = swelling increment; [5]CBR$_s$ = CBR soaked with water; [6]CBR$_{ws}$ = CBR without soaking.

TABLE 2: Results of resilient modulus test.

CD[1] (%)	Resilient modulus (MPa)			
	Value 1	Value 2	Value 3	Average/SD
100	133.56	136.42	137.63	135.87/2.09
96	121.34	124.48	126.82	124.21/2.75

[1]CD = compaction degree. [2]SD = standard deviation.

50 kPa $\sigma_s = 154.80 - 28.32 \log (n)$ $R^2 = 0.97$
100 kPa $\sigma_s = 306.66 - 83.04 \log (n)$ $R^2 = 0.99$
150 kPa $\sigma_s = 442.93 - 125.44 \log (n)$ $R^2 = 0.99$

(a)

50 kPa $\sigma_s = 120.49 - 31.27 \log (n)$ $R^2 = 0.99$
100 kPa $\sigma_s = 234.24 - 74.651 \log (n)$ $R^2 = 0.97$
150 kPa $\sigma_s = 343.85 - 111.44 \log (n)$ $R^2 = 0.91$

(b)
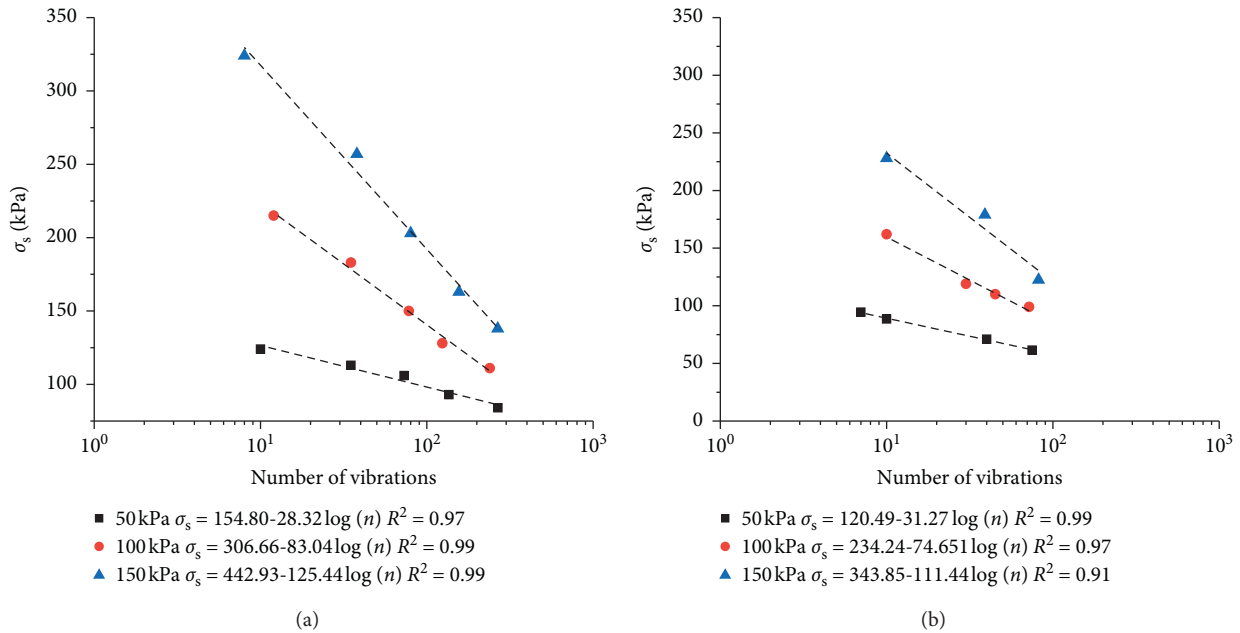
FIGURE 3: Dynamic strength of SOF. (a) Before F-T cycles. (b) After F-T cycles.

contributes to shear strength under high stress conditions, while the cohesion tends to play a more important role under low stress conditions. Furthermore, the friction angle and cohesion of SOF decrease at the ratio of 9.2%~12% and 30%~45% under the same testing condition after F-T cycles, which verifies the above conclusion.

3.3. Long-Term Deformation Characteristics. Figure 6 shows long-term deformation diagrams of SOF subjected to 8000 cyclic loadings. In the figure, the area swept by the graphic strips is the deformation range, where the upper edge

represents the maximum elastic deformation and the lower edge is the minimum permanent deformation. The deformation remains as large values at the condition of higher vertical stress after F-T cycles. All deformation curves increase sharply during the first 500 cyclic loadings and then tend to be at a steady growth, which reflects the typical plastic characteristics of SOF. The stress-strain hysteresis ring of the first and 8000th vibration is shown in Figure 7, where the slight elasticity decay can be found. Moreover, according to traditional calculated expressions, the resilient modulus of SOF subjected to long-term cyclic vibrations is derived and shown in Figure 8. Just as the figure describes,

Figure 4: Diagram of Mohr–Column strength method.

■ $n = 10\ t = 9.377 + 0.702 \times s\ R^2 = 0.99$
● $n = 50\ t = 16.485 + 0.627 \times s\ R^2 = 0.99$
▲ $n = 100\ t = 20.750 + 0.582 \times s\ R^2 = 0.99$

(a)

■ $n = 10\ t = 7.005 + 0.649 \times s\ R^2 = 0.99$
● $n = 50\ t = 9.702 + 0.569 \times s\ R^2 = 0.99$
▲ $n = 100\ t = 11.916 + 0.520 \times s\ R^2 = 0.99$

(b)
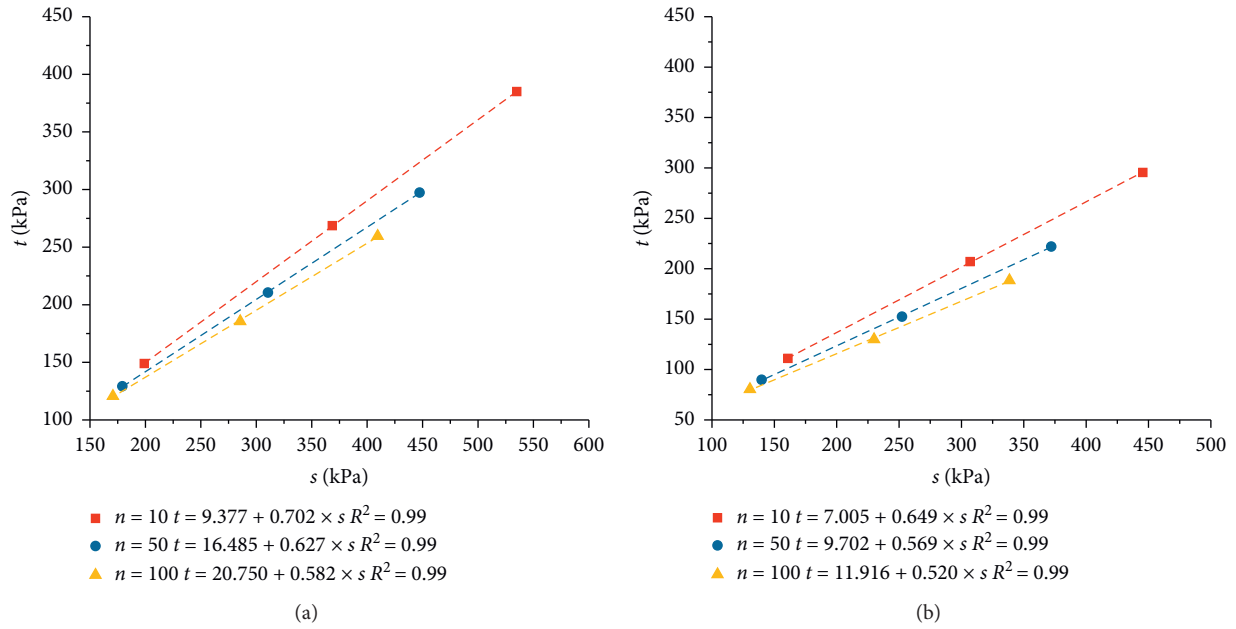
Figure 5: S-t diagrams for the test soils. (a) Before F-T cycles. (b) After F-T cycles.

Table 3: Shear strength parameters of test specimens.

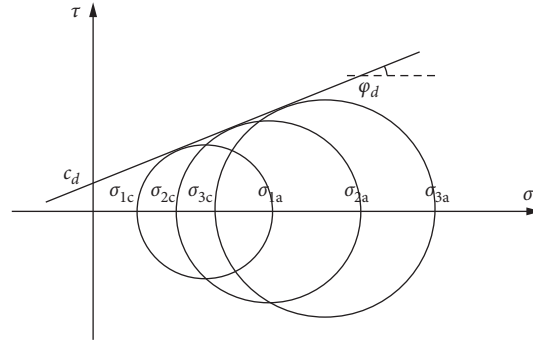| F-T state	Vibration numbers of failure (n)	Strength parameters	
		φ_d	c_d
Without F-T cycles	10	44.59	13.17
	50	38.83	21.16
	100	35.59	25.52
After F-T cycles	10	40.47	9.21
	50	34.68	11.80
	100	31.33	13.95

the resilient modulus exhibits a small attenuation. The deformation performance is far better than that of other subgrade filling materials [25, 26].

For subgrades, the accumulation deformation under repeated vehicle loadings is a very important index to assess the long-term stability of road structure. There are specified requirements for subgrade of highway and railway in China

[27, 28]. Figure 9 shows the detailed deformation curve of SOF during the first 10 cyclic vibrations. Lines A and B, corresponding to the fitting curves of minimum deformation points and force equilibrium points, are usually taken to predict the potential deformation of filling materials under long-term repeated loadings. In this part, Line B is adopted to fit the deformation points in the form of following equation:

$$\varepsilon = An^b, \tag{2}$$

where ε represents the accumulation deformation (%), n represents the vibration numbers, and A and b are fitting parameters. The calculated results are shown in Table 4.

In Table 4, the fitting model presents a good credibility. The fitting parameters of A and b change from 0.063 to 0.447 and 0.078 to 0.139, respectively. The effects of stress and F-T cycles on A and b are not reflected apparently. The variation trend of accumulation deformation is determined by the product of parameters A and b. Based on the traffic statistic
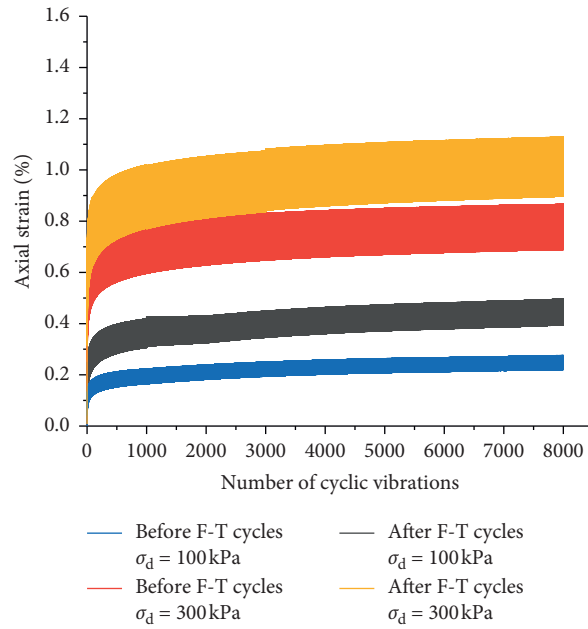
FIGURE 6: Long-term deformation curves of SOF.
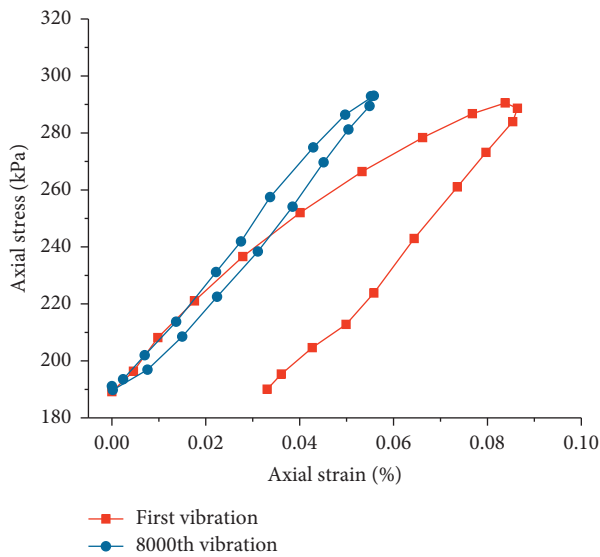
FIGURE 7: Stress-strain rings of the 1st and 8000th vibration.

FIGURE 8: Resilient modulus of SOF during large times of vibration.

data, 10 million vibrations are used to predict the residual deformation of SOF subgrade after operation of several years. Furthermore, taking account of the worst service environment, the fitting result at the deviator stress of 300 kPa after F-T cycles is adopted. The calculated accumulation strain is 1.57%. Consequently, the calculated accumulation deformation is 0.79 cm with the filling thickness of 50 cm, which is far lower than the limit of 10 cm for expressway and Grade I highway.

After large numbers of vehicle loads, the deformation of SOF is similar to the dynamic strength, which show good road performance and F-T durability related to the structure of SOF. According to the previous research by the authors [13], it is found that the particles of SOF are small and

uneven and have no obvious direction. The particles are interconnected by cementation and binding water to form an agglomerate-plate structure, which possesses good mechanical fatigue characteristics, especially for the F-T environment, because fine particles will soon find new stable structures and quickly shape, and then maintain relatively stable performance.

3.4. Environment Impact Assessment of SOF. The x-ray diffraction reflectogram and spectra of FTIR for three raw materials and SOF are shown in Figures 10 and 11, respectively. Furthermore, the parallel tests of SOF after F-T
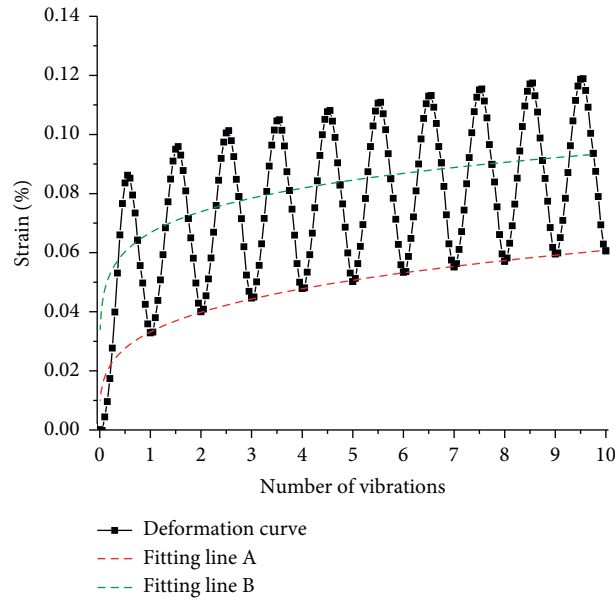
Figure 9: Detailed deformation curve of SOF during the first 10 cyclic vibrations.

Table 4: Fitting results of long-term deformation prediction model.

Testing state	Deviator axial stress (kPa)	$\varepsilon = An^b$		
		A	b	R^2
Without F-T cycles	100	0.063	0.139	0.986
	300	0.349	0.076	0.989
After F-T cycles	100	0.127	0.125	0.983
	300	0.447	0.078	0.993

cycles are also carried out. In figures, the fluctuations of the reflectogram and waveforms represent the corresponding substances, and the higher peak represents the larger content of the substance. Consequently, the mineral compositions of specimens are listed in Table 5. Just as shown, the fluctuations of oil shale, fly ash, and silty clay are all reflected in SOF, and the peaks are basically consistent with the superimposed values at the mix ratio. However, some subtle differences are still worth discussing, especially for the effect of F-T cycles on SOF. In Figure 10, the fluctuation in 2-theta of 27.5° is slightly fiercer after F-T cycles, which represents the transformation of potassium feldspar to plagioclase in SOF. The same situation occurs in the wave number of $1425\,cm^{-1}$ in Figure 11, where amorphous calcium carbonates generate. Furthermore, the wave fluctuations in the wave number of 916 and $3620\,cm^{-1}$ of Figure 11 disappear during the mixing process and regenerate after F-T cycles, which is the change manifestation of hydroxyl substances. For the safety assessment of SOF, the small amount of chemical bonds transformation and morphological substance exhibit little effect on the overall material composition. Therefore, it can be concluded that the chemical composition of SOF is stable enough.

The potential hazards of SOF leachates on environment are derived from their toxicity and corrosivity. The surface and ground water standard of China [29, 30] are used to judge the negative impact of leachates on the surrounding
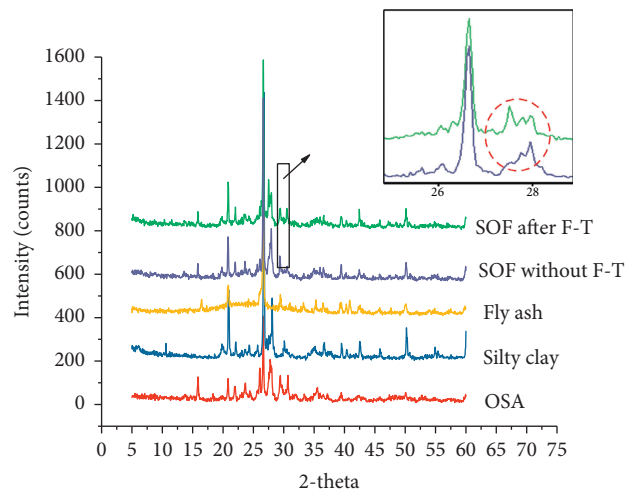
Figure 10: X-ray diffraction reflectograms of test soils.

water resources. As seen from Table 6, the concentration of trace elements plays a more decisive role than that of cations and anions. The soil leachates are in line with the benchmarks of Class II surface water and Class III ground water, which accords with the domestic water for drinking, breeding, and agriculture production. Moreover, SOF can be classified as the alkaline soil based on the pH value. The
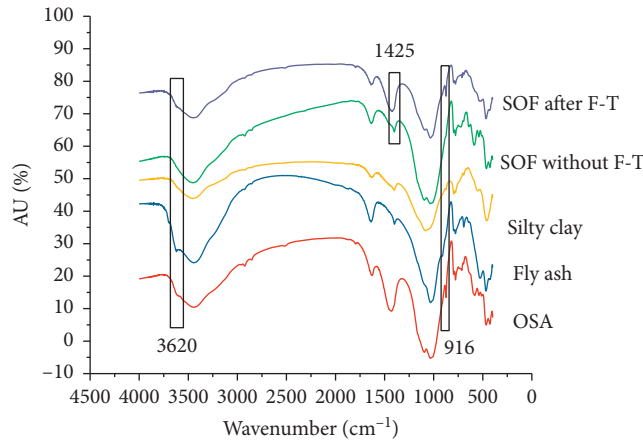
FIGURE 11: FTIR analysis for test soils.

TABLE 5: Mineral composition of raw materials and SOF.

Composition	OSA (%)	Fly ash (%)	Silty clay (%)	SOF (%)
Quartz	25	50	30	32
Plagioclase	8	12	--	8
Orthoclase	--	2	--	1
Analcime	5	--	--	2
Calcite	10	--	--	4
Kaolinite	--	5	--	1
Illite/montmorillonite	48	30	--	33
Mullite	---	--	10	4
Organic material	4	1	--	2
Amorphous	--	--	60	13

TABLE 6: Chemical composition analysis of SOF leachates.

Test items	Contents	Standard
Concentration of cations and anions	Na^+, K^+, Ca^{2+}, Mg^{2+}, NH_3-N, Cl^-, SO_4^{2-}, CO_3^{2-}, NO_3^-, F^-, PO_4^-	Surface water (Class I) Ground water (Class I)
Concentration of trace elements	Al, As, Ba, Cd, Cr, Cu, Fe, Pb, Mn, Cs, Se, Ag, V, Zn	Surface water (Class II) Ground water (Class III)
Corrosivity	pH value = 8.26	Alkalinity

alkaline soil always belongs to a good subgrade filling material because of the easy compaction and great water absorption. Its stable mechanical property determines a huge advantage in rainy weather construction or concrete pavement. Some detailed experimental demonstrations in situ will be conducted in the follow-up study to perform environment impact assessment of SOF, and that will be the focus of subsequent research.

4. Conclusions

In order to provide a safety assessment for the experimental road of SOF, a series of standardized experiments are performed. Some valuable conclusions are obtained as follows:

(1) In terms of CBR and resilient modulus, the road performance of SOF exceeds the standard requirement of the relevant specifications. It can maintain good performance at bad conditions of low compaction degree and being soaked for a long time.

(2) The dynamic strength of SOF is higher than that of most of original and stabilized soils. By the analysis of Mohr–Coulomb theory, it can be inferred that the friction of SOF mostly contributes to shear strength under high stress conditions, while its cohesion tends to play a more important role under low stress conditions.

(3) The deformation characteristics of SOF conform to the conventional deformation phase and variation trend. The increase rates of plastic deformation and modulus attenuation with repeated vibrations are slightly low, which results in the overall small accumulation settlement. The prediction results by the fitting formula show that the accumulation deformation of SOF after 10 million traffic loadings is far lower than the specified limit of relevant standards.

(4) According to the environment impact assessment of SOF, the chemical composition during mixing preparation and F-T cycles is basically stable. The leachates are in line with the benchmarks of Class II surface water and Class III ground water. Moreover, the corrosivity analysis is alkalinity with pH value of 8.26, which indicates its good workability.

In conclusion, the workability of SOF has been proven to be great theoretically. However, more practical cases are needed to verify the results of laboratory tests, especially for the durability under unfavorable circumstances. Further research will focus on the data acquisition method, in-depth comparison, and environment impact assessment of experimental road.

Data Availability

The data used to support the findings of this study are available from the corresponding author upon request.

Conflicts of Interest

The authors declare no conflicts of interest.

Acknowledgments

References

[1] E. Knaus, J. Killen, K. Biglarbigi, and P. Crawford, "An overview of oil shale resources," *ACS Symposium Series*, vol. 1032, pp. 3–20, 2010.

[2] C. Yan and X. Jiang, "The utilization of oil shale energy in China," *Energy of China*, vol. 9, pp. 21–25, 2000, in Chinese.

[3] J. Hou, Y. Ma, S. Li, and J. Teng, "Development and utilization of oil shale worldwide," *Chemical Industry and Engineering Process*, vol. 34, pp. 1183–1190, 2015, in Chinese.

[4] C. Gen, S. Li, and J. Qian, "New development and utilization of Chinese oil shale," in *Proceedings of the 33th Oil Shale Symposium*, Colorado School of Mines Golden, Tallinn, EstoniaColorado School of Mines Golden, Tallinn, Estonia, 2013.

[5] M. Smol, J. Kulczycka, A. Henclik, K. Gorazda, and Z. Wzorek, "The possible use of sewage sludge ash (SSA) in the construction industry as a way towards a circular economy," *Journal of Cleaner Production*, vol. 95, pp. 45–54, 2015.

[6] K. Ghuzlan, G. Al-Khateeb, and A. A. Damrah, "Using oil shale ash waste as a modifier for asphalt binders," *Journal of Material Cycles and Waste Management*, vol. 15, no. 4, pp. 522–529, 2013.

[7] M. O. J. Azzam and Z. Al-Ghazawi, "Evaluation of incorporating oil shale filler aggregate into hot mix asphalt using Superpave mix design," *Construction and Building Materials*, vol. 101, pp. 359–379, 2015.

[8] W. Wang, Y. Cheng, G. Tan, Z. Liu, and C. Shi, "Laboratory investigation on high- and low-temperature performances of asphalt mastics modified by waste oil shale ash," *Journal of Material Cycles and Waste Management*, vol. 20, no. 3, pp. 1710–1723, 2018.

[9] J. P. Turner, *Soil Stabilization Using Oil Shale Solid Wastes: Laboratory Evaluation of Engineering Properties*, Department of Civil Engineering, University of Wyoming, Laramie, WY, USA, 1991.

[10] J. P. Turner, "Soil stabilization using oil-shale solid waste," *Journal of Geotechnical Engineering*, vol. 120, no. 4, pp. 646–660, 1994.

[11] A. Koroljova and A. Pototski, "Use of oil shale fly ash as a binder material in stabilization of soft soils," in *Proceedings of the 12th International Symposium on Tropical Problems in the Field of Electrical and Power Engineering*, pp. 11–16, Kuressaare, Estonia, 2012.

[12] M. Rokainen, A. Koroljova, A. Pototski, H. Puhkim, P. Lahtinen, and O. Kiviniemi, "Utilization of oil shale ashes in road construction," in *Proceedings of Nordic Geotechnical Meeting*, pp. 1–10, Copenhagen, Denmark, May 2012.

[13] H. Wei, Y. Zhang, F. Wang, G. Che, and Q. Li, "Experimental research on resilient modulus of silty clay modified by oil shale ash and fly ash after freeze-thaw cycles," *Applied Sciences*, vol. 8, no. 8, p. 1298, 2018.

[14] Y. Zhang, "Research on dynamic properties and deformation characteristics of subgrade filling modified by oil shale wastes in seasonally frozen area," Ph. D. thesis, Jilin University, Changchun, China, 2019, in Chinese.

[15] J. Cui, "Research on stability of subgrade soil modified by oil shale waste residue and fly ash," Master's thesis, Changchun, China, 2018, in Chinese.

[16] A. Mohajerani, S. Lound, G. Liassos, H. Kurmus, A. Ukwatta, and M. Nazari, "Physical, mechanical and chemical properties of biosolids and raw brown coal fly ash, and their combination for road structural fill applications," *Journal of Cleaner Production*, vol. 166, pp. 1–11, 2017.

[17] K. Deb and Y. K. Narnaware, "Strength and compressibility characteristics of fiber-reinforced subgrade and their effects on response of granular fill-subgrade system," *Transportation in Developing Economies*, vol. 1, no. 2, p. 1, 2015.

[18] R. Murthy, S. Nazarian, and M. Picornell, "Dynamic properties of naturally-cemented silt," in *Proceedings of Geotechnical Earthquake Engineering & Soil Dynamics Congress IV*, pp. 1–8, Sacramento, CA, USA, 2008.

[19] S. Baig, M. Picornell, and S. Nazarian, "Low strain shear moduli of cemented sands," *Journal of Geotechnical and Geoenvironmental Engineering*, vol. 123, no. 6, pp. 540–545, 1997.

[20] P. M. Gallagher and J. K. Mitchell, "Influence of colloidal silica grout on liquefaction potential and cyclic undrained behavior of loose sand," *Soil Dynamics and Earthquake Engineering*, vol. 22, no. 9–12, pp. 1017–1026, 2002.

[21] Ministry of Transport of the People's Republic of China, *Test Methods of Soils for Highway Engineering (JTG E40-2007)*, China Communications Press, Beijing, China, 2007, in Chinese.

[22] Ministry of Transport of People's Republic of China, *Specifications for Design of Highway Subgrades (JTG D30-2015)*, China Communications Press, Beijing, China, 2015.

[23] S. Sağlam and B. S. Bakır, "Cyclic response of saturated silts," *Soil Dynamics and Earthquake Engineering*, vol. 61, pp. 164–175, 2014.

[24] J. Wang, H. Liu, C. Wu, and X. Qu, "Influence of freeze-thaw cycles on dynamic characteristics of subgrade soils with

different plasticity indices," *Chinese Journal of Geotechnical Engineering*, vol. 36, pp. 633–639, 2014.

[25] Y. Cai, Q. Sun, L. Guo, C. H. Juang, and J. Wang, "Permanent deformation characteristics of saturated sand under cyclic loading," *Canadian Geotechnical Journal*, vol. 52, no. 6, pp. 795–807, 2015.

[26] S. K. Navaratnarajah and B. Indraratna, "Use of rubber mats to improve the deformation and degradation behavior of rail ballast under cyclic loading," *Journal of Geotechnical and Geoenvironmental Engineering*, vol. 143, no. 6, Article ID 04017015, 2017.

[27] Ministry of Railways of People's Republic of China, *Code for Design of Railway Earth Structure (TB10001-2016)*, China Communications Press, Beijing, China, 2016.

[28] Ministry of Ecology and Environment of People's Republic of China, *Environmental Quality Standards for Surface Water (GB 3838–2002)*, China Communications Press, Beijing, China, 2002.

[29] General Administration of Quality Supervision, Inspection and Quarantine of People's Republic of China, *Standard for Groundwater Quality (GB 14848–2017)*, China Communications Press, Beijing, China, 2017.

[30] Ministry of Ecology and Environment of People's Republic of China, *Identification Standards for Hazardous Wastes-Identification for Extraction Toxicity (GB 5085.3-2007)*, China Communications Press, Beijing, China, 2007.

Research Article

Surface and New Building Deformation Analysis of Deep Well Strip Mining

Yuanzhong Luan (ID)**, Yue Dong, Yanhe Ma, and Liyuan Weng** (ID)

College of Geodesy and Geomatics, Shandong University of Science and Technology, Qingdao, China

Correspondence should be addressed to Liyuan Weng; wengliyuanhh@163.com

Aiming at the problem of surface movement and long-term stability of a work plane of deep well strip mining in Shandong Province, an observation station is set up on the surface of strip mining, and the surface deformation value during strip mining is measured with advanced measuring instruments; on the stable surface of the old mining area, the surface deformation monitoring work is also carried out for new buildings. In addition, the FLAC3D simulation method is used to determine the subsidence factor of different mining depth, mining width, mining length, and mining thickness, and the mathematical model between the subsidence factor and mining depth, mining width, mining length, and mining thickness is established. After the surface of the old goaf is basically stable after strip mining, the high-rise buildings are built. By changing the size of the new buildings and the amount of the load imposed on the surface, the surface deformation is simulated and calculated, and the relationship between the different load positions, load sizes, loading building sizes, and the surface activated deformation is obtained. The measured value of the surface deformation confirms that the load of the new buildings can induce the activation of the old goaf and make the surface generate secondary deformation, but the activated deformation makes the new building within the range of 1, so the new building is safe.

1. Introduction

With the expansion of China's coal mining scale and the rapid development of urbanization, land resources for mining is becoming increasingly scarce. Thus, some important buildings have to be built over the goaf [1, 2]. However, the movement and deformation of the surface, after coal seam mining, is not a one-step process [3]. It takes several years or even more than 10 years to stabilize. Even after stabilization, mechanical properties of the falling rock strata in the goaf will change when external force (such as building loads) is applied above the goaf [4]. These factors can break the relative balance of the overlying strata in the goaf and cause surface movement again [5, 6]. All these will pose a threat to the foundation of the existing buildings built over the goaf, causing uneven settlement, destruction, and even collapse of the building.

The deformation of the new buildings over the goaf is mainly affected by the residual deformation of the surface movement after coal seam mining and the secondary deformation "activated" by the new building load [7]. The residual deformation value of the surface movement after the coal seam is mined can be obtained by subtracting the generated deformation value from the total deformation value of the area; for the total deformation value, it can be calculated by using the probability integral method according to the rock movement parameters such as the subsidence coefficient; for the generated deformation value, it can be obtained based on the *in situ* measured data [8, 9]. Therefore, studying the variation characteristic of the surface subsidence coefficient under different mining conditions is of great significance to choose the timing of building construction.

The broken rocks in the goaf tend to stabilize after a long period of natural compaction, and there are a large number of holes and cracks in the caving zone and the fractured zone [10, 11]. So, when affected by external forces (such as new

buildings on the surface), the hidden cavity, bed separation, and fracture zone will be compacted for the second time, which will cause the surface activation to produce new moving deformation [12, 13].

Over the years, scholars at home and abroad have done a lot of in-depth researches in this study, and there are many breakthroughs in the researches. Swift explains the relations between overburden strata movement of the internal joint and ground surface subsidence [14]. The surface subsidence rule affected by the ratio of extraction to reservation, mining and pillar width, thickness of bedrock, thickness of loose layer, and mining thickness of thick alluvium and thin bedrock is simulated and analysed by Zhang et al. [15]. Ghabraie et al. investigated the mechanism of multiple seam subsidence and established key parameters in the strata movement behavior after multiple-seam extraction using physical modeling [11]. Based on the method of superimposed stress, Zhou adopts the method of σ_z (superimposed stress) $= 0.10\sigma_{cz}$ (gravity stress) to determine the influenced depth of the building load and puts forward the formula of calculating the number of safety layers for the construction of new buildings [16]. However, the surface activated deformation value of new high-rise buildings after the stabilization of the surface of the 1 km-deep well strip mining work plane has been barely discussed.

In the present study, a case study was carried out on 11021 and 11041 working faces in the east wing strip of a coal mine in the Jining mining area of Shandong Province. Based on the measured data of surface movement and the surface deformation of different mining depth, mining thickness, mining width, and mining length simulated by FLAC3D, the corresponding subsidence factor is obtained, and the regression equations between the subsidence factor and mining depth, mining thickness, mining width, and mining length are established, respectively [17–20]. Furthermore, by means of loading to new buildings on the surface of the old goaf in strip mining, the characteristics of surface activated deformation of new buildings with different load positions, load sizes, and loading building sizes above the goaf are simulated and studied [21, 22]. The magnitude of increase in activated deformation and the level of surface deformation are determined based on the measured value of surface activated deformation.

2. The Measured Value of Surface Movement Factor in Strip Mining

2.1. Geology Overview.
The mine is located in Jining City, Shandong Province, China. The coal seam is nearly horizontal with a mean thickness of 8 m. All panels in this mine are using the fully mechanized top coal caving method.

Panels 11021 and 11041 are selected for this case study. These two panels are 100 m apart at a depth of 1000 m and both are approximately 80 m wide along the dip. Panels 11021 and 11041 are about 800 m long along the strike, respectively. The stratigraphic distribution of the mine is shown in Figure 1.

2.2. Surface Movement Observation.
In the mining process, the observation station of surface movement was established, the plane coordinates of the observation points were measured by the Network CORS system and the 2-second total station, and the elevation was observed by the Dini03 electronic level produced by the Trimble Company of the US. The observation points of surface movement are arranged along the strike and the trend of the work planes 11021 and 11041, and the arrangement of the observation points is shown in Figure 2.

In the work planes 11021 and 11041, work was stopped from March 2012, and from then, the task of the ground surface deformation observation was performed. The observation work was operated for one year after the end of mining process of the work planes, and then it was stopped. Many plane and vertical movement values were observed by using Network CORS, Tianbao Dini03, and other electronic levels according to some technical requirements about the *Regulations of the Building Deformation Observation*. The ground surface deformation calculation can be operated by the ground surface movement and the deformation data handling designed by MapInfo.

2.3. Calculation of Surface Movement Parameters.
By using the software of the probability integral method to invert the rock movement parameters, the parameter inversion calculation is carried out for the measured surface movement observation value, and the predicted parameters of the surface movement of the work planes 11021 and 11041 are obtained, as shown in Table 1.

2.4. Maximum Deformation Value of Any Point on the Ground Surface.
According to the parameters obtained by inversion, the maximum deformation value at any point under the influence of coal seal mining is obtained. The probability integral method, based on the normal distribution function as the influence function, expresses the surface subsidence basin with the integral formula. The related formulas for calculating the movement and deformation of any point on the surface, respectively, are expressed in the following [23–27]:
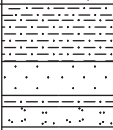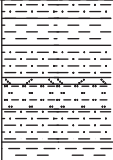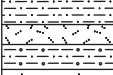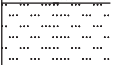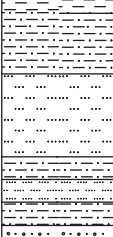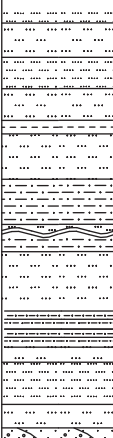
(1) Maximum subsidence value:

$$W(x, y) = f(t) \cdot W_{\max} \iint_D \frac{1}{r^2} e^{-\pi \left(\left((\mu - x)^2 + (\lambda - y)^2 \right) / r^2 \right)} \mathrm{d}\mu \mathrm{d}\lambda. \tag{1}$$

(2) Maximum dip:

$$i_x(x, y) = f(t) \cdot W_{\max} \iint_D \frac{2 \cdot \pi \cdot (\mu - x)}{r^4} e^{-\pi \left(\left((\mu - x)^2 + (\lambda - y)^2 \right) / r^2 \right)} \mathrm{d}\mu \mathrm{d}\lambda,$$

$$i_y(x, y) = f(t) \cdot W_{\max} \iint_D \frac{2 \cdot \pi \cdot (\lambda - x)}{r^4} e^{-\pi \left(\left((\mu - x)^2 + (\lambda - y)^2 \right) / r^2 \right)} \mathrm{d}\mu \mathrm{d}\lambda. \tag{2}$$

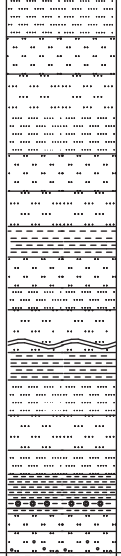| Stratum		Average thickness (m)	Composite column 1:500	Lithological characteristics
Period	Group			
Quaternary period	Upper group	61.32		It comprises the tawny luidity clay, sandy clay, brown maroon sand with the fine medium and coarse side, and hardpan strata. And, it partly contains the calcareous clay.
	Middle group	80.60		It comprises the greyish celadon and tawny clay, sandy clay with the gravel, and clayey sand. And, it contains the gravel with lens shape once in a while.
	Last group	30.00		The primary color is celadon, and the tawny color, maroon color, etc., are partly distributed on it. And, it mainly comprises the sandy clay, clayey sand gravel, and clayey sand.
Q Paleogene system E	Upper part	60.00		There are two parts on the regional information. This region just keeps the last part, which comprises the brown sandstone, siltstone, and red mudstone, and it has a poor cementation.
	Last part	40.00		
Jurassic system J	Santaizi group	110.00		The color is greyish and celadon, and the brown color is partly distributed on it. It primarily comprises the siltstone of the sandy mudstone with many fine sandstones. And, the sandy conglomerate is spreaded on the bottom. The sandstone is mainly composed of the quartz and mud. There is a phenomenon of partial calcareous cementation, and it is usually seen in a wave, gentle wave, and horizontal shape.
		200.00		It mainly comprises the fine sandstone that is purplish, maroon, and dove grey, and it is partly medium sandstone with purplish sandy mudstone, siltstone, and sandstone that mainly contains quartz which is composed of feldspar, mica flakes, and dark mineral. The mud material and iron material are cemented. The oblique bedding is promoted. The medium and bottom structures are not tight and contain the mudstone and siltstone that are comparatively soft.

(a)

Triassic system P	Shihezi group (Kui shan , Wan shan area)	260.61		It mainly comprises the mudstone and siltstone that are yellow green, light green, and partial maroon and the medium and fine sandstone that is celadon. Fossil flakes of plant and carbonize trunks can be seen occasionally. The sandstone is mainly composed of quartz which contains many feldspars and a few micas and green minerals. The mud material and silicon material are cemented, and they contain the mudstone and bands. Generally, the selection outcome is not reasonable. And, there is usually a layer of aluminous mudstone at the bottom, under which there is a medium sandstone at the bottom boundary. And, it partly contains gravel.
	Hei shan area	50.98		It mainly comprises the mudstone and siltstone that is yellow green, celadon, and purple and the fine sandstone that is celadon.
Triassic system P	Shan xi group	76.57		It mainly comprises medium and fine sandstone that is greyish, ashen, and celadon and the siltstone, mudstone, and coal that are dark grey. The upper part is mainly composed of the mudstone and siltstone. The medium and bottom part are composed of the medium and fine sandstone with the mudstone, siltstone, and coal.
	Tai yuan group	168.47		It comprises the fine sandstone, siltstone, sandy mudstone, and mudstone (the medium sandstone can be seen at the partial center area) that is grey, dark grey, and black grey and eleven layers of limestone and coal seam that are greyish.

(b)

Figure 1: Stratigraphic distribution of the mine.

(3) Maximum curvature:

$$K_x(x, y) = f(t) \cdot W_{\max} \iint_D \frac{2 \cdot \pi}{r^4} \left(\frac{2 \cdot \pi \cdot (\mu - x)}{r^2} - 1 \right) e^{-\pi \left(\left((\mu - x)^2 + (\lambda - y)^2 \right) / r^2 \right)} \mathrm{d}\mu \mathrm{d}\lambda,$$

$$K_y(x, y) = f(t) \cdot W_{\max} \iint_D \frac{2 \cdot \pi}{r^4} \left(\frac{2 \cdot \pi \cdot (\mu - y)}{r^2} - 1 \right) e^{-\pi \left(\left((\mu - x)^2 + (\lambda - y)^2 \right) / r^2 \right)} \mathrm{d}\mu \mathrm{d}\lambda.$$

(3)
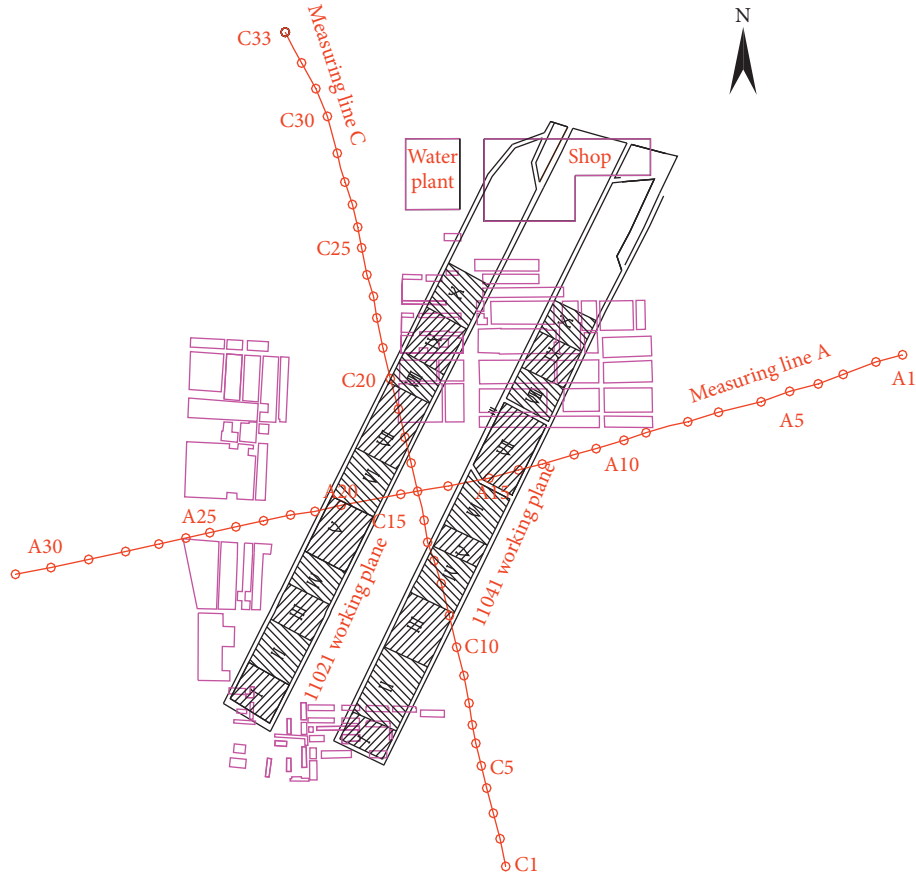
FIGURE 2: Map of observation points.

TABLE 1: List of improved probability integral method parameters.

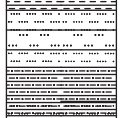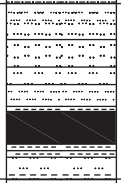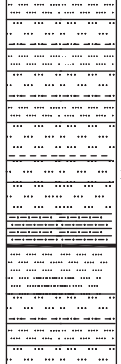| Coal rake	Rock movement parameters				
	q	b	$\tan \beta$	θ	S
3	0.14	0.26	2.1	90°	0.027H

(4) Maximum value of horizontal movement:

$$U_x(x, y) = f(t) \cdot U_{\max} \iint_D \frac{2 \cdot \pi \cdot (\mu - x)}{r^3} e^{-\pi\left((\mu-x)^2+(\lambda-y)^2/r^2\right)} \mathrm{d}\mu \mathrm{d}\lambda,$$

$$U_y(x, y) = f(t) \cdot U_{\max} \iint_D \frac{2 \cdot \pi \cdot (\mu - y)}{r^3} e^{-\pi\left((\mu-x)^2+(\lambda-y)^2/r^2\right)} \mathrm{d}\mu \mathrm{d}\lambda$$

$$+ W(x, y) \cdot \cot \theta_0.$$

$$(4)$$

(5) Maximum value of horizontal deformation:

$$\varepsilon_x(x, y) = f(t) \cdot U_{\max} \iint_D \frac{2 \cdot \pi}{r^3} \left(\frac{2 \cdot \pi \cdot (\mu - x)}{r^2} - 1\right) e^{-\pi\left((\mu-x)^2+(\lambda-y)^2/r^2\right)} \mathrm{d}\mu \mathrm{d}\lambda,$$

$$\varepsilon_y(x, y) = f(t) \cdot U_{\max} \iint_D \frac{2 \cdot \pi}{r^3} \left(\frac{2 \cdot \pi \cdot (\lambda - y)^2}{r^2} - 1\right) e^{-\pi\left((\mu-x)^2+(\lambda-y)^2/r^2\right)} \mathrm{d}\mu \mathrm{d}\lambda + i_y(x, y) \cdot \cot \theta_0.$$

$$(5)$$

In the above formulas, $W_{\max}$ and $U_{\max}$ are the maximum subsidence value and the maximum value of horizontal movement of the surface, respectively, when they are fully mined. The calculation formulas are as follows:

$$W_{\max} = q \cdot m,$$
$$U_{\max} = b \cdot W_{\max}, \tag{6}$$

where q represents the subsidence coefficient, m is the thickness (mm), and b represents the horizontal movement coefficient.

3. Relationship between Subsidence Factor and Mining Depth, Mining Width, Mining Length, and Mining Thickness

The influence of different mining depth, mining width, mining length, and mining thickness on the surface movement characteristic in deep well strip mining is quantitatively studied. According to the geological conditions of work planes 11021 and 11041, 16 three-dimensional models are established for different mining conditions, and the surface subsidence values of different models are calculated by numerical simulation, so as to determine the functional relationships between mining depth, mining width, mining length, mining thickness, and the surface subsidence factor in deep well strip mining.

Due to the large depth of work planes 11021 and 11041, the numerical model cannot cover all the rock strata, except for the coal, roof, and floor strata. Figure 3 shows the entire 16 rock strata with corresponding thickness.

The mechanical properties of the coal and rock strata in the FLAC3D numerical model are usually determined by the laboratory experiments.

3.1. Relationship between Subsidence Factor and Mining Depth.
Four calculation models of strip mining simulation are established on the basis of the FLAC3D numerical simulation software towards the mining depths 800 m, 900 m, 1000 m, and 1100 m, and its mining width is 80 m, leaving width is 100 m, and recovery ratio is 45%. The obliquity of the coal seam is calculated horizontally, and the outcomes of simulation are shown in Table 2.

According to the data in Table 2, the regression curve between the subsidence factor and the mining depth is shown in Figure 4.

It can be seen from Figure 4 that the subsidence factor is linear with the increase in mining depth, and the regression equation of the two is

$$q = -0.00024H + 0.333. \tag{7}$$

3.2. Relationship between Subsidence Factor and Mining Width.
Four numerical simulation models are established, respectively, for the mining width of 80 m, 100 m, 120 m, and 140 m. The mining depth of each model is 1000 m, the

leaving width is 100 m, and the mining thickness is 8 m. The coal seam dip is calculated horizontally. The simulation results are shown in Table 3.

According to the data in Table 3, the regression curve of the relationship between the subsidence factor and the mining width w is shown in Figure 5.

It can be seen from Figure 5 that the relationship between the subsidence factor and the increase in mining width w is a power correlation. The regression equation is

$$q = 0.02302 e^{0.01737w}. \tag{8}$$

3.3. Relationship between Subsidence Factor and Mining Length.
Towards the strip mining plan, that is to say, the mining depth is 1000 m, the mining thickness is 8 m, the mining width is 80 m, and the leaving width is 100 m, besides, the recovery ratio is 45%, four simulation models are set up. And, the mining length is 400 m, 600 m, 800 m, and 1000 m, respectively. The simulation outcomes of obliquity of the coal seam based on the horizontal calculation are given in Table 4.

According to the data in Table 4, the regression curve between the subsidence factor and the mining length is shown in Figure 6.

It can be seen from Figure 6 that the subsidence factor increases with the increase in the mining length, which mainly reflects the mining degree of the mining area. The regression equation is as follows:

$$q = 0.1165 \ln(L) - 0.6819. \tag{9}$$

3.4. Relationship between Subsidence Factor and Mining Thickness.
For the mining plan of "mining depth 1000 m, mining width 80 m, leaving width 100 m, and recovery ratio 45%," four calculation models are set up according to the mining thickness of 2 m, 4 m, 6 m, and 8 m, respectively. The boundary conditions and rock mass mechanical parameters of each model are consistent with the previous calculation. The numerical simulation results are shown in Table 5.

According to the data in Table 5, the regression curve of the relationship between the subsidence factor and the mining thickness is shown in Figure 7.

It can be seen from Figure 7 that, in strip mining, the mining thickness increases and the subsidence value also increases. The subsidence factor and mining thickness show a power function relationship. When the mining thickness reaches a certain value, the subsidence factor will change slowly. The regression equation between the subsidence factor and the mining thickness is as follows:

$$q = 0.3026 M^{-0.6027}. \tag{10}$$

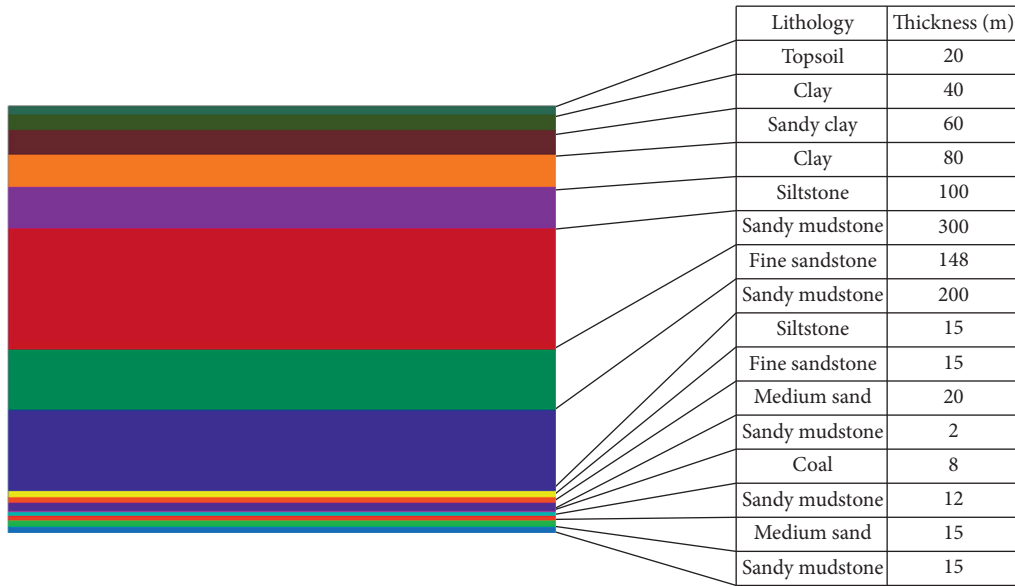| Lithology	Thickness (m)
Topsoil	20
Clay	40
Sandy clay	60
Clay	80
Siltstone	100
Sandy mudstone	300
Fine sandstone	148
Sandy mudstone	200
Siltstone	15
Fine sandstone	15
Medium sand	20
Sandy mudstone	2
Coal	8
Sandy mudstone	12
Medium sand	15
Sandy mudstone	15

FIGURE 3: 16 strata of the numerical model.

TABLE 2: Numerical simulation results in different mining depth.

Mining depth (m)	Maximum subsidence value (m)	Subsidence factor q	Remark
800	1.117	0.14	
900	0.961	0.12	Mining width 80 m
1000	0.719	0.09	Leaving width 100 m
1100	0.558	0.07	

4. Stability Analysis of New Surface Buildings in Strip Mining Area

The goafs that are introduced in the case analysis are composed of panels 11021 and 11041. With the mining depth of 1000 m, the mining width of 80 m, the leaving width of 100 m, and the mining thickness of 8 m, the inclination angles of the coal seam are ranging from degree one to degree two, and the goaf area is approximately 0.25 km^2. There are villages, factories, and other buildings on the surface above the goaf. After the surface of the goaf tends to be stable, the mechanical parameters of each layer are weakened to varying degrees.

In order to further study the influence of new buildings on the secondary deformation of the ground surface of the goaf, the rules between different load positions, loading building sizes, load weight, and the surface secondary subsidence values were explored. According to the geological conditions of work planes 11021 and 11041, several three-dimensional models are established, and the corresponding surface secondary subsidence values are solved by using the numerical simulation software. At the same time, the basic shape of the surface deformation is revealed by using the field survey data, which provides data for comparing with the numerical simulation data in this paper.

4.1. Relationship between Load Position and Surface Secondary Subsidence Value

4.1.1. Numerical Simulation Scheme. In order to study the surface secondary deformation characteristics of the building load in different positions of the old goaf, the simulation scheme is as follows. For the model after the surface of the old goaf is basically stable after strip mining, the three-level load with 0.4 MPa, 0.6 MPa, and 0.8 MPa is applied on the marginal area of the open-off cut, medium area of the work plane, medium area of the goaf, and marginal area of the stop line. As shown in Figure 8, the boundary conditions, rock parameters, and other influencing factors of each simulation scheme are consistent.

4.1.2. Analysis of Simulation Results. Due to the effect of the building load on the surface above the old goaf, the surface activation will generate new deformation, and the surface secondary subsidence values are shown in Figure 9.

Taking 0.6 MPa as an example, it shows the relationship between the load position and the surface secondary settlement caused by activation. Under 0.6 MPa, the secondary subsidence value of position 1 is 148.60 mm, position 2 is 131.53 mm, position 3 is 128.29 mm, and position 4 is 136.71 mm. It can be seen that under the same level of load, the relationship between the amount of the surface
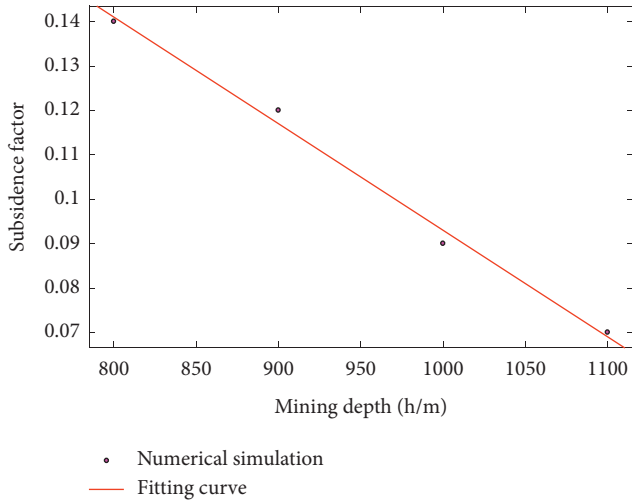
FIGURE 4: Relationship between the subsidence factor and the mining depth.

TABLE 3: Numerical stimulation results in different mining width.

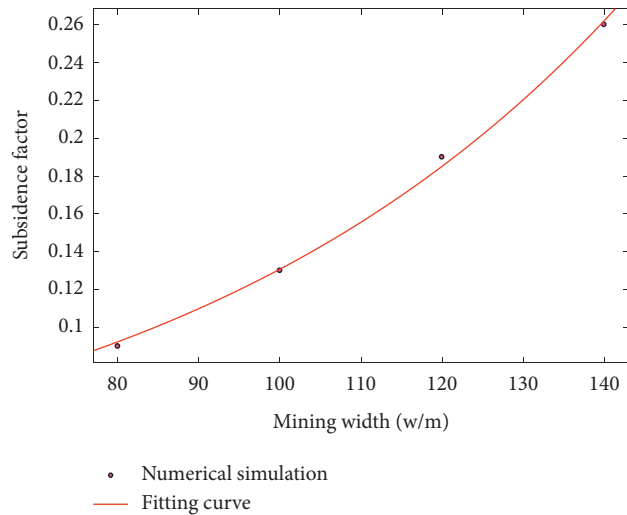| Mining width (m)	Maximum subsidence value (m)	Subsidence factor	Remark
80	0.719	0.09	Mining
100	1.403	0.13	length 800 m,
120	1.516	0.19	mining depth
140	2.064	0.26	1000 m

FIGURE 5: Relationship between the subsidence factor and the mining width.

secondary subsidence value at different load positions is position 1 > position 4 > position 2 > position 3. Under other levels of load, this relationship also holds.

It indicates that the secondary deformation value of the surface activated by the new buildings is different in the different building location. The secondary surface deformation value activated by the new buildings located in the medium area of the goaf is the least, followed by the medium

area of the work plane, the marginal area of the open-off cut, and the marginal area of the stop line. As the load level increases, the stability of the middle area of the goaf becomes more obvious. In order to reduce the impact of the secondary deformation of the surface on the new buildings and reduce the settlement range of the building foundation when the buildings are constructed over the old goaf, it is better to choose the medium area of the old goaf as much as possible to avoid the two dangerous areas, the marginal area of the open-off cut and the marginal area of the stop line.

4.2. Relationship between the Size of the Building Loads and Surface Secondary Subsidence of the Old Goaf

4.2.1. Numerical Simulation Scheme. In order to study the influence of the building size on the surface secondary subsidence value, the specific simulation scheme is as follows: nine numerical simulation models with a building size of $40 \times 20 \, m^2$, $20 \times 100 \, m^2$, $40 \times 60 \, m^2$, $40 \times 100 \, m^2$, $40 \times 140 \, m^2$, $60 \times 100 \, m^2$, $80 \times 100 \, m^2$, $100 \times 100 \, m^2$, and $120 \times 100 \, m^2$ are set up with 0.6Mpa. The boundary conditions and rock parameters of each simulation scheme remain unchanged.

4.2.2. Analysis of Simulation Results. After the completion of excavation, 0.6 MPa building load is applied on position 3 for different size of models. Due to the effect of building load on the surface above the goaf, the surface activation will generate new deformation, and its subsidence value is shown in Table 6.

It can be seen from Table 6 that when other influencing factors remain unchanged, the surface secondary subsidence value increases with the increase in the building size.

With the regression analysis on the maximum values of secondary deformation obtained by simulation of each scheme, the regression curve between the building size and the value of surface secondary settlement caused by activation is shown in Figure 10.

The quadratic polynomial function of the new building size and the maximum value of surface secondary settlement is as follows:

$$y = -7.25 \times 10^{-7} x^2 + 0.02065x + 54.47. \qquad (11)$$

The influence of the width-to-length ratio of new buildings on the secondary deformation of the ground surface of the goaf is further studied. The analysis of the building model selected with its length of 100 meters and different width-to-length ratios shows that the value of "activated" surface subsidence increases as the ratio of the building width to length becomes bigger, as shown in Table 7.

Maximum values of secondary deformation obtained by every plan and simulation are analysed by use of the MATLAB software. The curvilinear regression of the value of the secondary deformation and the width-to-length ratio of the building is shown in Figure 11.

When the length of the new building is 100 meters, the quadratic polynomial function about the building width-to-length ratio and the secondary settlement of the "activated" surface is

TABLE 4: Numerical stimulation results in different mining length.

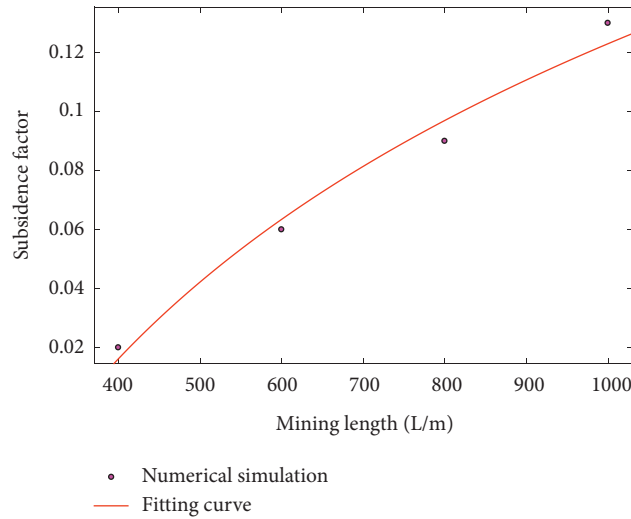| Mining length (m)	Maximum subsidence value (m)	Subsidence factor	Remark
400	0.561	0.02	
600	0.876	0.06	Mining depth 1000 m, mining thickness 8 m, mining width 80 m, leaving width 100 m
800	0.719	0.09	
1000	1.197	0.13	

FIGURE 6: Relationship between the subsidence factor and the mining length.

TABLE 5: Numerical stimulation results in different mining thickness.

Mining thickness (m)	Maximum subsidence value (m)	Subsidence factor	Remark
2	0.402	0.2	
4	0.515	0.13	Mining depth 1000 m, mining width 80 m, leaving width 100 m
6	0.597	0.1	
8	0.719	0.09	

$$y = -97.53x^2 + 244.5x + 43.35. \quad (12)$$

4.3. Analysis of Deformation Data of New Surface Buildings in Strip Mining Area. The exclusive e-commerce building with fifteen storeys was initially constructed by Jining on the surface of 11021 and 11041 strip mining work planes in March 2016 on the basis of the construction plan. Comparing the maximum deformation of the building location calculated by the probability integral method with the measured deformation data, it can be known that the surface of the goaf was approaching the maximum subsidence value due to the influence of the surface movement after coal seal mining. Due to the effect of the new building load on the surface of the old goaf, the secondary deformation was caused by the surface activation. In order to ensure the stability of the building foundation, deformation monitoring was carried out in the surface observation points A13, A14, A15, A16, A17, A18, A19, A20, C14, C15, C16, and C17

around the building in the initial construction stage, and the arrangement of the observation points is shown in Figure 12.

The observation began on March 1, 2016. After the first observation, the observation was conducted once for each additional layer until the top is closed. After the construction work is completed, the observation was conducted once every two months. By December 1, 2018, the observation had lasted for two years and nine months, with a total of 13 observations. The curve of the surface secondary settlement caused by activation of the monitoring point is shown in Figure 13. According to the curve of the surface settlement value and time, when the settlement rate is less than 0.01–0.04 (mm/d), it is considered that the surface has entered a stable stage and the observation is stopped.

It can be seen from Figure 13 that the maximum value of the surface secondary settlement caused by activation of the monitoring point is 112.3 mm, the minimum of that is 72.24 mm, and the average of that is 94.3 mm. The settlement rate is less than 0.01–0.04 (mm/d), the maximum horizontal
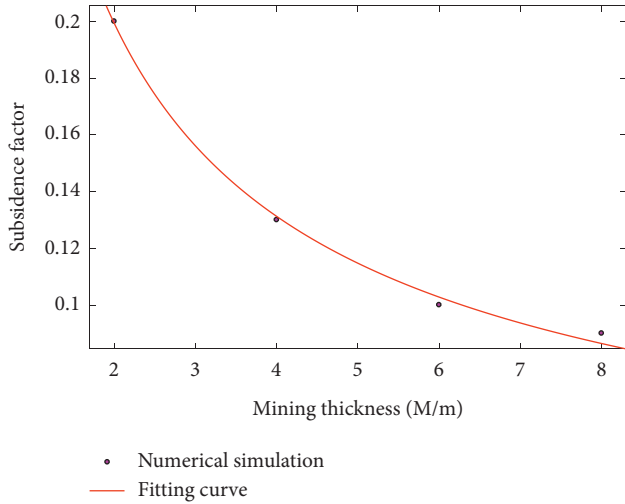
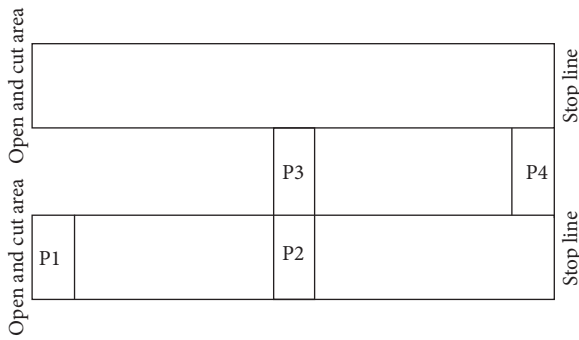FIGURE 7: Relationship between the subsidence factor and the mining thickness.

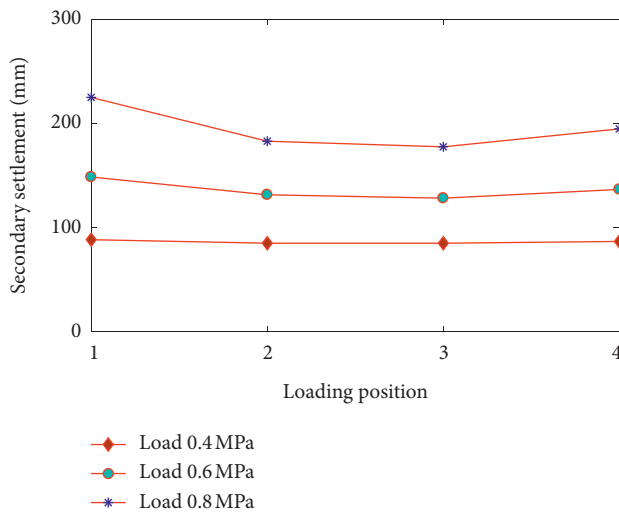
FIGURE 8: Building load location.

FIGURE 9: Relationship between load position and surface secondary subsidence.

TABLE 6: Secondary subsidence value with different building sizes.

Building size (m²)	Secondary subsidence value (mm)
40 × 20	68.13
20 × 100	86.55
40 × 60	111.11
40 × 100	128.29
40 × 140	136.4
60 × 100	155.99
80 × 100	174.93
100 × 100	188.44
120 × 100	197.84
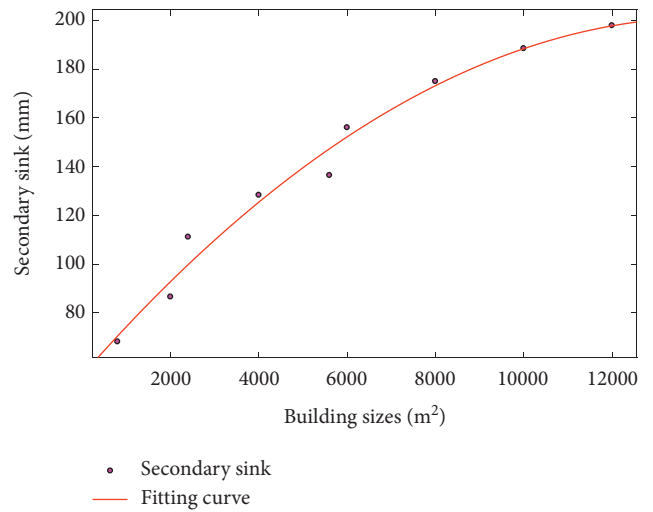
FIGURE 10: Fitting curve of building size and maximum surface secondary settlement.

TABLE 7: Secondary sink in different building width-to-length ratios.

Size of building (m²)	Width-to-length ratio of building	Value of secondary deformation (mm)
20 × 100	0.2	86.55
40 × 100	0.4	128.29
60 × 100	0.6	155.99
80 × 100	0.8	174.93
100 × 100	1.0	188.44
120 × 100	1.2	197.84

tends to be stable. Although the new building activates the surface of the old goaf and increases the surface subsidence value, according to the Safety Supervision Total Coal Loading (2017) No. 66 and "Coal pillar and coal mining regulations in buildings, structures, water, and mine," combined with the comprehensive factors including actual horizontal deformation, curvature, and dip, the deformation of the new building is still within the scope of Class I deformation.

In this area, the maximum subsidence of the ground surface monitored at the newly built 20-layer buildings in the nonexcavated areas is generally 20 mm to 30 mm, while the maximum subsidence of the 15-floor experience

deformation is 1.8 mm/m, the maximum curvature is $0.14 * 10^{-3}$/m, and the maximum dip is 3.0 mm/m, when the value of monitoring points near the experience building

FIGURE 11: Fitting curve of the building width-to-length ratio and maximum secondary settlement.

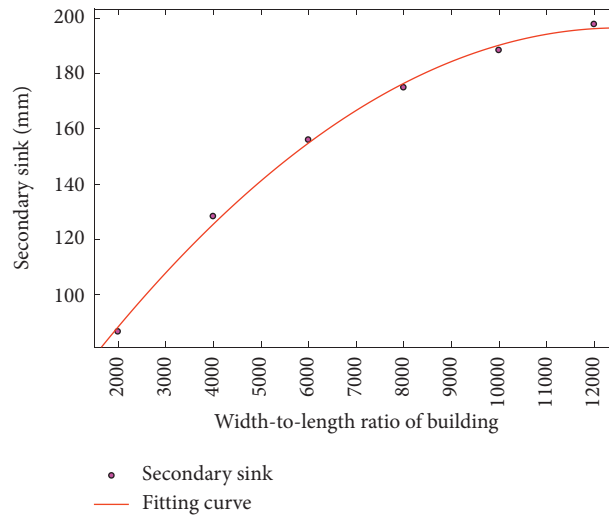building is 112.3 mm. The result indicates that the effect of the load of the newly built buildings induces the activation of the old goaf and secondary deformation of the ground surface. The maximum value of surface secondary deformation of the goaf is about 4 times than that of the nonexcavated areas.

5. Discussion

5.1. Monitoring Method of Surface Movement in Deep Well Strip Mining. Due to the small amount of surface movement and no water on the surface in deep well mining, Lidar and RTK technology are combined to collect field data of surface subsidence in mining areas, manual intervention processing is carried out on the acquired point cloud data, and the point cloud data and the generated DEM are used to analyze the surface subsidence deformation of the coal mine; besides, D-InSAR technology and deformation monitoring method of Network CORS based on Beidou can be carried out, and the "third class" elevation measurement accuracy can be achieved by improving the outdoor survey system and implementing a more precise data processing model [28–32].

5.2. The Characteristic of Mining Surface Movement in Deep Well Strip Mining. In order to control the surface deformation, protect the surface buildings, and prevent the impact of rock burst, the mining methods such as strip mining and backfill mining are adopted in the underground mining work plane [33]. Generally speaking, with the increase in mining depth, the surface movement and deformation decrease is relatively gentle, the main influence angle tangent increases, the subsidence factor decreases, the comprehensive movement angle increases, the comprehensive boundary angle increases first and then decreases, and the geological mining conditions of the work plane are quite different [34, 35]. For example, there are thick conglomerate strata or magmatic rock

and other hard rock layers in the overlying strata of some mining work planes, which results in a big difference in the law of surface movement and deformation [36, 37]. In order to meet the needs of safety production of mining, the characteristic of surface movement in deep well strip mining is an urgent problem.

5.3. Long-Term Stability of New Buildings above Old Goaf. After the mining of the underground coal seam, the overlying rock above the goaf will gradually be in a relatively balanced state after a long time of natural compaction. When the new building is located on the surface above the old goaf, under the effect of the building load, it will produce additional stress to the foundation soil and transfer it down according to certain rules, changing the stress state of the fractured rock above the old goaf, making the overlying rock of the goaf produce new deformation and failure [38]. The stability of the ground surface will be strengthened if the strip mining or backfill mining method is adopted by the work plane [39–41]. The stability of the ground surface will be comparatively favourable if the overlaying rock above the work plane has thick conglomerate strata and other hard rock layers [42]. As to the issue, the works of ground surface movement observation and numerical simulation are performed to explore the rules of the ground surface movement in the area of mines.

6. Conclusions

After the operation of the deep well strip mining, the surface movement and the secondary deformation of the goaf caused by the applied load have a great impact on the surface buildings. This paper analyzes the surface subsidence characteristic of the two work planes No. 11021 and No. 11041 in a Jining mine and the stability of the new building with 15 storeys after the surface of the goaf stabilizes. According to field measured data and FLAC3D numerical simulation data, the mathematical models of subsidence
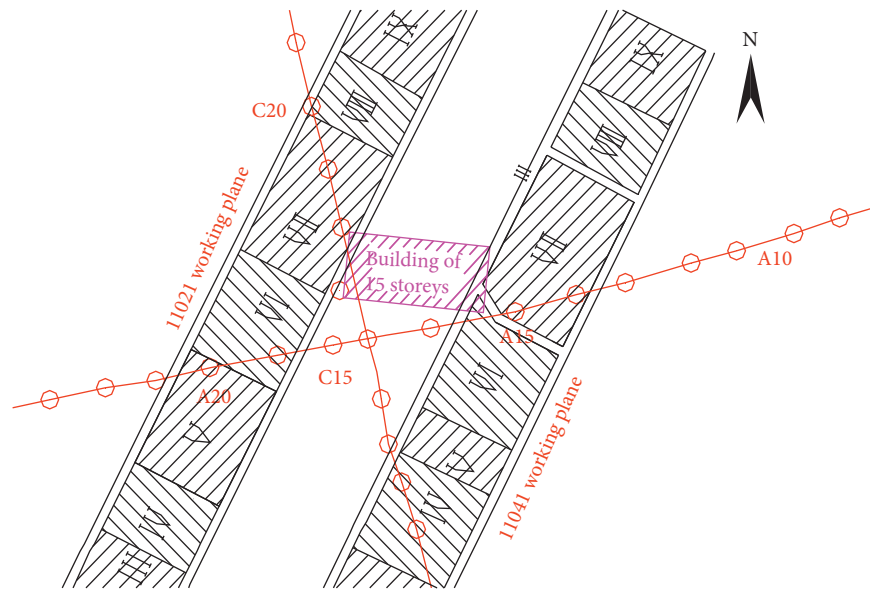
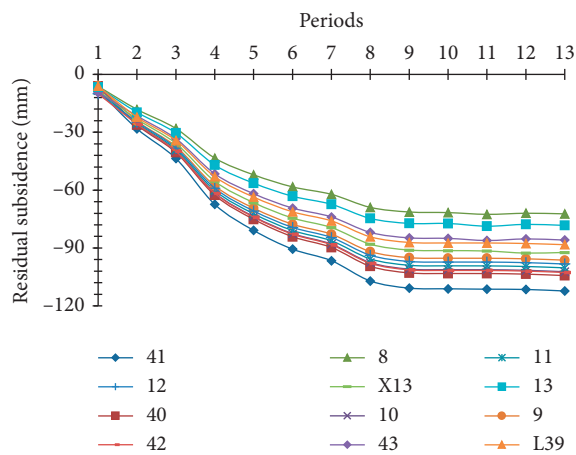FIGURE 12: Overview of observation points around the building.

FIGURE 13: Monitoring point settlement.

coefficients and "activated" deformation characteristics of the goaf were obtained under different mining conditions.

During deep well strip mining, under the premise of other fixed conditions, the subsidence coefficient decreases with the increase in the mining depth, showing a prior inverse relationship, and the function model expresses $q = -0.00024H + 0.333$. The subsidence coefficient increases with the increase in the mining width, showing a power correlation, and the function model expresses $q = 0.02302e^{0.01737w}$. The subsidence coefficient increases with the increase in the mining length, and the function model expresses $q = 0.1165 \ln(L) - 0.6819$. The subsidence coefficient increases with the thickness of the mining, showing a power function relationship, and the function model expresses $q = 0.3026M^{-0.6027}$.

The stability of the new buildings built on the surface in the medium area of the goaf is the best. When the buildings are

constructed over the old goaf, we should choose the medium area of the old goaf as much as possible. There is a quadratic function relationship between the size of the new building and the "activated" subsidence of the goaf, and the function model expresses $y = -7.25 \times 10^{-7}x^2 + 0.02065x + 54.47$; under the premise of the fixed length of the new building, the "activated" surface subsidence increases with the increase in the width-to-length ratio of the building, and the function model expresses $y = -97.53x^2 + 244.5x + 43.35$. The measured data show that the "activated" surface of the old goaf is subjected to secondary movement and deformation under the load of new buildings, and the maximum subsidence value of the old goaf is about 4 times than that of the nongoaf.

Based on the measured data and simulation analysis, the relationship between different geological conditions and the surface subsidence factor in deep well strip mining and the rule that how new buildings on the surface of the old goaf influence the secondary deformation are obtained. The conclusions can also be applied to the study of the stability of the building foundation of the goaf in the same geological conditions. It is also used to the construction of the infrastructure in the mining area, the planning of the town in the mining area, and the protection of buildings and the design of the coal seam mining.

Data Availability

The data used to support the findings of this study are available from the corresponding author upon request.

Conflicts of Interest

The authors declare that there are no conflicts of interest regarding the publication of this paper.

Acknowledgments

References

[1] N. Jiang, J. H. Zhao, X. Z. Sun, L. Y. Bai, and C. X. Wang, "Use of flyash slurry in backfill grouting in coal mines," *Heliyon*, vol. 3, no. 11, Article ID e00470, 2017.

[2] W. Li and X. Jia, "Ground control issues on photovoltaic power generation facilities construction in coal sinkhole region," *Procedia Engineering*, vol. 191, pp. 98–103, 2017.

[3] G. L. Guo, K. Z. Deng, and J. Chang, "Study on the foundation settlement of heavy buildings above mine gobs," *Journal of China University of Mining & Technology*, vol. 12, no. 2, pp. 54–57, 1996, in Chinese.

[4] Y. J. Zhang, "Research on the safety effect of reconstruction to frame structures in subsidence area," *Ph.D. thesis, North China University of Technology*, in Chinese, 2017.

[5] B. Shen, B. Poulsen, X. Luo, J. Qin, R. Thiruvenkatachari, and Y. Duan, "Remediation and monitoring of abandoned mines," *International Journal of Mining Science and Technology*, vol. 27, no. 5, pp. 803–811, 2017.

[6] X. Sun, P. Yang, and Z. Zhang, "A study of earthquakes induced by water injection in the Changning salt mine area, SW China," *Journal of Asian Earth Sciences*, vol. 136, pp. 102–109, 2017.

[7] K. Z. Deng, Z. X. Tan, H. Z. Zhang, H. D. Fan, and L. Y. Zhang, "Research on calculating method of residual subsidence of longwall goaf," *Journal of China Coal Society*, vol. 37, no. 10, pp. 1601–1605, 2012, in Chinese.

[8] B. You, *Evaluation of the Stability of Building Foundations on Old Goaf*, Jilin University, Changchun, China, 2012, in Chinese.

[9] X. Cui, Y. Zhao, G. Wang, B. Zhang, and C. Li, "Calculation of residual surface subsidence above abandoned longwall coal mining," *Sustainability*, vol. 12, no. 4, p. 1528, 2020.

[10] J. Ning, J. Wang, Y. Tan, L. Zhang, and T. Bu, "In situ investigations into mining-induced overburden failures in close multiple-seam longwall mining: a case study," *Geomechanics and Engineering*, vol. 12, no. 4, pp. 657–673, 2017.

[11] B. Ghabraie, G. Ren, X. Zhang, and J. Smith, "Physical modelling of subsidence from sequential extraction of partially overlapping longwall panels and study of substrata movement characteristics," *International Journal of Coal Geology*, vol. 140, pp. 71–83, 2015.

[12] Y. Sun, X. Zhang, W. Mao, and L. Xu, "Mechanism and stability evaluation of goaf ground subsidence in the third mining area in Gong Changling district, China," *Arabian Journal of Geosciences*, vol. 8, no. 2, pp. 639–646, 2015.

[13] G. Yu, W. Mi, D. Wang, L. Gao, S. Lu, and G. Li, "Research on the relationship between the surface dynamic subsidence and overburden separated strata of coal mine and its model," *Procedia Engineering*, vol. 191, pp. 196–205, 2017.

[14] G. Swift, "Relationship between joint movement and mining subsidence," *Bulletin of Engineering Geology and the Environment*, vol. 73, no. 1, pp. 163–176, 2014.

[15] W. Q. Zhang, H. L. Liu, and K. Zhao, "Influential factors on surface subsidence in stripe mining under thick unconsolidated layers and thin bedrock," *Journal of Mining & Safety Engineering*, vol. 33, no. 6, pp. 1065–1071, 2016.

[16] G. L. Zhou, "Evaluation and analysis of the stability of goaf under new building load," *Journal of North China Institute of Science and Technology*, vol. 14, no. 2, pp. 23–27, 2017, in Chinese.

[17] L. Y. Wang, K. Z. Deng, and M. N. Zheng, "Research on ground deformation monitoring method in mining areas using the probability integral model fusion D-InSAR, sub-band InSAR and offset-tracking," *International Journal of Applied Earth Observations and Geoinformation*, vol. 85, Article ID 101981, 2020.

[18] C. Wang, Y. Lu, C. Qin, Y. Li, Q. Sun, and D. Wang, "Ground disturbance of different building locations in old goaf area: a case study in China," *Geotechnical and Geological Engineering*, vol. 37, no. 5, pp. 4311–4325, 2019.

[19] X. Chi, K. Yang, Q. Fu, and L. Dou, "The mechanism of mining-induced stress evolution and ground pressure control at irregular working faces in inclined seams," *Geotechnical and Geological Engineering*, vol. 38, no. 1, pp. 91–107, 2019.

[20] G. Li and Q. H. Yang, "Prediction of mining subsidence in shallow coal seam," *Advances in Civil Engineering*, vol. 2020, Article ID 7956947, 9 pages, 2020.

[21] Y. H. Bao, *Foundation Stability Analysis of Newly Buildings on Old Goaf Surface*, Shandong University of Science and Technology, Qingdao, China, 2018, in Chinese.

[22] H. R. Zhang, *Analysis and Research of Ground Deformation of Goaf in Meihe Coal Mine*, Jilin University, Changchun, China, 2013, in Chinese.

[23] J. F. Gu and Z. S. Gao, "Application of probability-integral method in the prediction of mining subsidence," *Mine Surveying*, vol. 2, pp. 47–49, 2011.

[24] Q. Yao, T. Feng, S. L. Li, S. L. Li, and Q. Y. Ning, "The subsidence prediction of coal mine "three under" mining based on probability integral method," *Safety in Coal Mines*, vol. 43, no. 7, pp. 188–190, 2012.

[25] M. Zheng, K. Deng, S. Du, J. Liu, J. Liu, and J. Feng, "Joint probability integral method and TCPInSAR for monitoring mining time-series deformation," *Journal of the Indian Society of Remote Sensing*, vol. 47, no. 1, pp. 63–75, 2019.

[26] X. Zhu, G. Guo, H. Liu, and X. Yang, "Surface subsidence prediction method of backfill-strip mining in coal mining," *Bulletin of Engineering Geology and the Environment*, vol. 78, no. 8, pp. 6235–6248, 2019.

[27] Z. S. Wang, *Study on the non-liner prediction theory of old goaf residual subsidence and its application*, Ph.D. thesis, China University of Mining and Technology, Xuzhou, China, 2011, in Chinese.

[28] S. Samsonov, N. d'Oreye, and B. Smets, "Ground deformation associated with post-mining activity at the French-German border revealed by novel InSAR time series method," *International Journal of Applied Earth Observation and Geoinformation*, vol. 23, pp. 142–154, 2013.

[29] B. Zhang, L. Zhang, H. Yang, Z. Zhang, and J. Tao, "Subsidence prediction and susceptibility zonation for collapse above goaf with thick alluvial cover: a case study of the Yongcheng coalfield, Henan province, China," *Bulletin of Engineering Geology and the Environment*, vol. 75, no. 3, pp. 1117–1132, 2016.

[30] M. Lyu, Y. Ke, L. Guo et al., "Change in regional land subsidence in Beijing after south-to-north water diversion project observed using satellite radar interferometry," *GIScience & Remote Sensing*, vol. 57, no. 1, pp. 140–156, 2020.

[31] B. Q. Gong, Z. H. Li, C. Yu et al., "Three-dimensional time-varying large surface displacements in coal exploiting areas revealed through integration of SAR pixel offset

measurements and mining subsidence model," *Remote Sensing of Environment*, vol. 240, Article ID 111663, 2020.

[32] A. Pal, J. Rošer, and M. Vulić, "Surface subsidence prognosis above an underground longwall excavation and based on 3D point cloud analysis," *Minerals*, vol. 10, no. 1, pp. 1–20, 2020.

[33] D. Xuan and J. Xu, "Longwall surface subsidence control by technology of isolated overburden grout injection," *International Journal of Mining Science and Technology*, vol. 27, no. 5, pp. 813–818, 2017.

[34] Z. Q. Wu, G. K. Wang, and L. Q. Zhao, "Study on the law of surface cracks while coal mining in the thin bedrock and thick unconsolidated layer of Yu-Shen-Fu mining area," in *Proceedings of the E3S Web of Conferences, 2018 3rd International Conference on Advances in Energy and Environment Research (ICAEER 2018)*, pp. 541–545, I-Shou University, University of the West of England, Hongkong Global Scientific Research Association, Guilin, China, August 2018.

[35] G. Zhao, W. Guo, and X. Li, "Mechanical properties of mega-thick alluvium and their influence on the surface subsidence," *Geotechnical and Geological Engineering*, vol. 38, no. 1, pp. 137–149, 2020.

[36] C. Liu, H. Li, and H. Mitri, "Effect of strata conditions on shield pressure and surface subsidence at a longwall top coal caving working face," *Rock Mechanics and Rock Engineering*, vol. 52, no. 5, pp. 1523–1537, 2019.

[37] H. Tu, H. Zhou, C. Qiao, and Y. Gao, "Excavation and kinematic analysis of a shallow large-span tunnel in an up-soft/low-hard rock stratum," *Tunnelling and Underground Space Technology*, vol. 97, Article ID 103245, 2020.

[38] S. Y. Wei, "Research on the Safety effect of residual deformation to reclaimed buildings in old goaf area," *Ph.D. thesis, North China University of Technology*, in Chinese, 2018.

[39] D. R. Tesarik, J. B. Seymour, and T. R. Yanske, "Long-term stability of a backfilled room-and-pillar test section at the Buick Mine, Missouri, USA," *International Journal of Rock Mechanics and Mining Sciences*, vol. 46, no. 7, pp. 1182–1196, 2009.

[40] A. M. Suchowerska, *The geomechanics of single-seam and multi-seam longwall coalmining*, Ph.D. thesis, University of Newcastle, Newcastle, Australia, 2014.

[41] C. Wang, Y. Lu, B. Cui, G. Hao, and X. Zhang, "Stability evaluation of old goaf treated with grouting under building load," *Geotechnical and Geological Engineering*, vol. 36, no. 4, pp. 2553–2564, 2018.

[42] Q. D. Wei, *Mechanism and prevention and control of rock burst in extra thick coal seams under super thick conglomerate stratum*, Ph.D. thesis, University of Science and Technology Beijing, Beijing, China, 2018.

Research Article

Effect of Calcium Carbonate on the Mechanical Properties and Microstructure of Red Clay

Lijie Chen,[1,2] **Xuejun Chen,**[1,2] **Xin Yang,**[1,2] **Pengyan Bi,**[1,2] **Xiang Ding,**[1,2] **Xiang Huang** ⬦[1,2] **and He Wang** ⬦[1,3]

[1]*College of Civil and Architecture Engineering, Guilin University of Technology, Guilin 541004, China*
[2]*Guangxi Key Laboratory of New Energy and Building Energy Saving, Guilin 541004, China*
[3]*Army Engineering University, Nanjing 21001, China*

Correspondence should be addressed to Xiang Huang; 6615031@glut.edu.cn and He Wang; wanghe502@126.com

The influence of precipitated calcium carbonate on the strength and microstructure of red clay was studied. Precipitated calcium carbonate was added to red clay at ratios of 0%, 5%, 10%, 15%, and 20%. Shear tests were carried out on the samples to observe the effect of calcium carbonate on the mechanical properties of red clay. The results showed that, with increasing calcium carbonate content, the strength of red clay first decreased and then increased. The maximum strength was obtained for the sample with 20% calcium carbonate. Scanning electron microscopy (SEM) was used to observe the changes in microstructure caused by addition of calcium carbonate. The pores and cracks analysis system (PCAS) was used to quantitatively characterize the microstructure changes detected in SEM images. The addition of calcium carbonate decreased the pore area and increased the total number of pores of red clay. The incorporation of calcium carbonate caused the red clay particles to agglomerate. The higher the calcium carbonate content, the stronger the agglomeration of red clay particles in the soil samples.

1. Introduction

Red clay is widely distributed in areas south of the Changjiang River in China, such as Guangxi, Guizhou, and Yunnan. Red clay is also locally distributed in Hunan, Hubei, Anhui, and Sichuan, mainly on plateaus, flats, hills, and low mountain slopes. Red clay develops in depressions and generally forms layers with a thickness of about 5–15 m. Red clay is characterized by its high liquid limit, large porosity ratio, tendency to shrink and crack, and poor water stability. The high strength of red clay means that it is often mistaken as a good foundation soil. However, because of the high shrinkage of red clay, when its thickness variation in the horizontal direction is large, uneven settling can easily occur over time, leading to building damage [1]. To promote economic development, China has stepped up its efforts to construct infrastructure in its western region. During the construction process, red clay with poor engineering properties is frequently encountered. At present, red clay is typically replaced by other soils prior to building construction. However, red clay is widely distributed in the southwest area of China. The disposal of large amounts of red clay will substantially increase the engineering cost of building and cause damage to the ecological environment.

The strength of red clay can be increased by chemical modification, such as adding lime, cement, fly ash, and other inorganic cementing materials [2–4]. These additives can also lower the liquid-plastic limit and improve the water stability of red clay. However, these methods can cause environmental pollution and are costly. In addition, the production of ordinary Portland cement has considerable environmental effects because it is an energy-intensive industrial process, accounting for 5%–7% of global CO_2 emission [5]. Many innovative approaches, such as liquid stabilizers [3, 6], have also been used to improve the properties of red clay. Calcium carbonate is widely distributed in regions with red clay, and it has a low mining cost and is easy to transport. The incorporation of precipitated

calcium carbonate into red clay has been shown to affect the strength of red clay [7]. However, the microstructural changes of red clay induced by doping with calcium carbonate have not been quantitatively analyzed. The soil microstructure affects its engineering properties, so its characterization has attracted the attention of many researchers.

Scanning electron microscopy (SEM) is a useful tool to investigate soil structure and accelerate research progress. SEM can be used to observe natural and synthetic soil samples, allowing the relationship between soil microstructure and engineering properties to be analyzed. Gillot [8] used SEM to study the structure of fine grains of soil. Diamond [9] analyzed the microstructure of impact-compacted kaolinite and illite clays after drying by SEM. Collins and McGown [10] conducted a qualitative study on the microstructure of soil and proposed some concepts to explain their results.

With the development of computer science and technology, computer image processing technology has been used to analyze the microscopic pore structure of soil. Tovey and coworkers [11, 12] conducted a quantitative analysis of electron micrographs of soil structures and combined several image processing and analysis techniques to study the porosity of clay particles. Their work provided a new method to study the mineralogy and microstructure of soil. Shi [13] quantitively analyzed clay samples using a D/MAX III-A fabric automatic goniometer and Video lab image analysis system, from which a plan of soil microstructures was proposed. More image processing software was then developed [14, 15], which allowed the geometric and structure parameters of pores and particles to be calculated. The PCAS image processing software [16] can accurately calculate the geometric parameters of soil microstructure, including pore size and pore shape, providing quantitative statistics. The PCAS software has been successfully applied to the quantitative analysis of the microstructure of both rock and soil [17, 18].

In this paper, the effect of precipitated calcium carbonate on the mechanical properties of red clay is analyzed by direct shear tests. SEM observation, particle size analysis, and stacking measurements are carried out to study the effect of precipitated calcium carbonate content on the microstructure of red clay. PCAS software is used to quantitatively analyze the influence of calcium carbonate incorporation on the porosity, micropore structure, and particle size distribution of red clay.

2. Materials and Methods

2.1. Materials. The red clay used in this study was from Yanshan, Guilin, China, collected at a depth of 3 m. The clay was brownish yellow mixed with brown in the plastic and hard plastic states. The parameters of the clay are listed in Table 1. Fine-grained soil with a particle size of less than 2 mm was obtained by drying and sieving the clay sample. The fine-grained red clay had a particle size ranging from

TABLE 1: Physical parameters of red clay.

Parameters	Values
Maximum dry density (g/cm^3)	1.67
Optimal moisture content (%)	22
Liquid limit (%)	49.68
Plastic limit (%)	37.53
Plasticity index (%)	12.15
Specific gravity	2.75

1.63 to 282.06 μm (Figure 1(a)). The precipitated calcium carbonate consisted of spindle-shaped particles with sizes ranging from 0.2 to 90 μm (Figure 1(b)).

2.2. Mechanical Testing. Calcium carbonate was blended into the fine-grained red clay at mass ratios of 0%, 5%, 10%, 15%, and 20%. The samples were thoroughly stirred and then sprayed with pure water to give a moisture content of 22%. The samples were shaped into cylinders with a length of 61.8 mm, diameter of 20 mm, and dry density of 1.4 g/cm^3. The shear rate of the direct shear test was 0.8 mm/min. Shear tests were carried out under vertical pressures of 100, 200, 300, and 400 kPa.

2.3. SEM Analysis. The red clay combined with precipitated calcium carbonate was made into a cylinder with a length of 10 mm and diameter of 10 mm, frozen in liquid nitrogen for 15 min, and then vacuum-dried for 24 h in a low-temperature vacuum machine. The sample was broken into pieces, which were attached to an SEM support with conductive tape, coated with metal, and then observed by field-emission SEM (Carl Zeiss). The magnification range of the field-emission SEM was between 12x and 1,000,000x, and the maximum diameter of the measurable sample was 25 mm.

2.3.1. Quantitative Analysis of Pore Structure. PCAS software developed by Liu et al. [16], which is a commercial software for analyzing the pore structure of soil in high-resolution SEM images, was used to analyze the calcium carbonate-doped red clay samples. PCAS software has previously been used to analyze the fractures and pores of clay minerals [19, 20].

The pore area and length analyzed by the PCAS software were calculated using pixels and converted to actual values by image resolution using equations (1) and (2):

$$S_f = \frac{S_P}{P^2}, \tag{1}$$

$$L_f = \frac{L_P}{P}, \tag{2}$$

where S_f is the actual area, S_p is the pixel area, L_f is the actual length, L_p is the pixel length, and P is the pixel resolution.

The fractal dimension (D_f) is used to measure shape irregularities. In this study, PCAS software was used to calculate D_f of the pores of the calcium carbonate-doped red
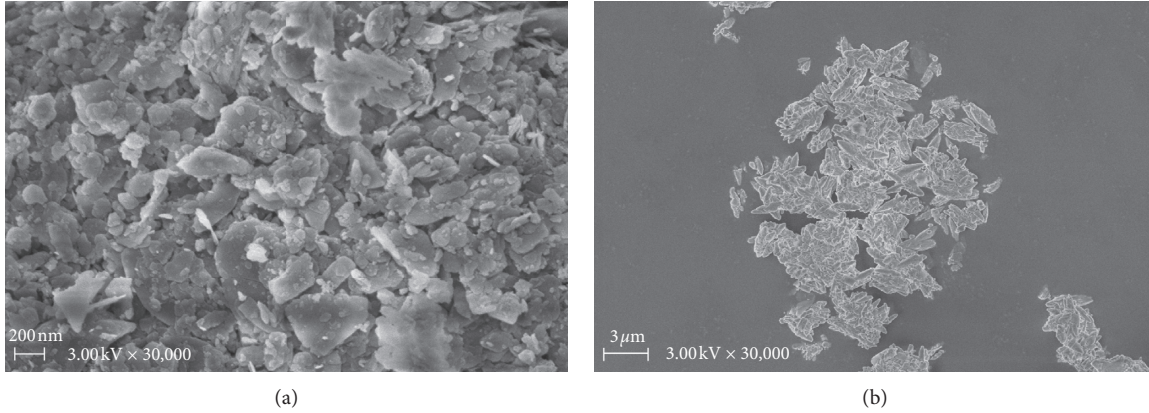
(a)

(b)

FIGURE 1: SEM images of (a) red clay and (b) precipitated calcium carbonate.

clay samples and quantitatively analyze the influence of calcium carbonate on the pore structure of red clay. The relationship between D_f [15] and the pore perimeter (c) and pore area (s) can be expressed as

$$\log(c) = \frac{D_f}{2\log s} + c_1,$$ (3)

where c_1 is a constant. The relationship between the complexity of the pore and its area is evaluated by the area-perimeter method, which generally gives a value within the interval [21, 22].

The complexity of the pore properties can be quantified by the shape factor (f_f). By calculating f_f, the changes caused by the incorporation of precipitated calcium carbonate can be analyzed. f_f is calculated as [16]

$$f_f = \frac{4\pi s}{c^2},$$ (4)

f_f for a perfect circle and square are 1 and 0.785, respectively. The f_f values of a material are within the interval of [0, 1].

The probability entropy can be used to reflect the pore space of red clay. For the two-dimensional analysis, the interval of the arrangement, [0, n], of the aggregate is divided into equal parts of n, and the probability of the pore assembly on the ith part is Pi. Then, H is the probability entropy of the pore structure arrangement state, which can be calculated using the following equation [18]:

$$H = -\sum_{i}^{n} P_i \log_n (P_i).$$ (5)

In this study, $n = 18$; that is, the orientation angle is between $0°$ and $180°$. H is a statistical parameter that describes the arrangement of pore structure in the red clay samples and is within the interval [0, 1]. When H is 0, the direction of all pores is the same. When H approaches 0, the pore arrangement is ordered, and the pore direction is inconsistent. In contrast, the closer the H to 1, the weaker the orientation of the pores, i.e., the more random the pore direction.

3. Results and Discussion

3.1. Mechanical Properties. The direct shear test results (Figure 2) revealed that the shear strength of red clay decreased first and then increased with rising calcium carbonate content. Under the action of 100 kPa of vertical pressure, the strength of the sample with 5% calcium carbonate was lower than that of the undoped red clay. With increasing calcium carbonate content above 5%, the shear strength of the samples gradually increased. The maximum shear strength was observed for the red clay sample with a calcium carbonate content of 20%. A similar behavior was observed at different vertical pressures. The greater the vertical pressure, the larger the degree to which calcium carbonate increased the shear strength of red clay. For example, under the action of 400 kPa of vertical pressure, 15% calcium carbonate increased the shear strength of red clay by 1.34 times, and 20% calcium carbonate raised the shear strength of red clay by 158%.

Figure 3 shows that as the calcium carbonate content of the red clay samples increases, the cohesion of red clay decreases. The internal friction angle (φ) was the smallest for the sample containing 5% calcium carbonate. When the doping content of calcium carbonate exceeded 5%, φ was positively correlated with the amount of calcium carbonate, indicating that the addition of calcium carbonate can increase the friction between the red clay particles.

3.2. Pore Structure Analysis of Calcium Carbonate-Doped Red Clay

3.2.1. Pore Morphology. SEM was used to observe and analyze the soil samples to study the effect of calcium carbonate doping on the pores and microstructure of red clay. The results are shown in Figures 4–7. As the calcium carbonate doping content increases, the red clay particles become more disperse. Figure 4 shows an SEM image of the undoped red clay at 30000x magnification. In this image, most of the red clay particles are lamellar, and the particle distribution is irregular.

Comparing Figures 4 with 6 indicates that the particles of the red clay samples doped with different contents of
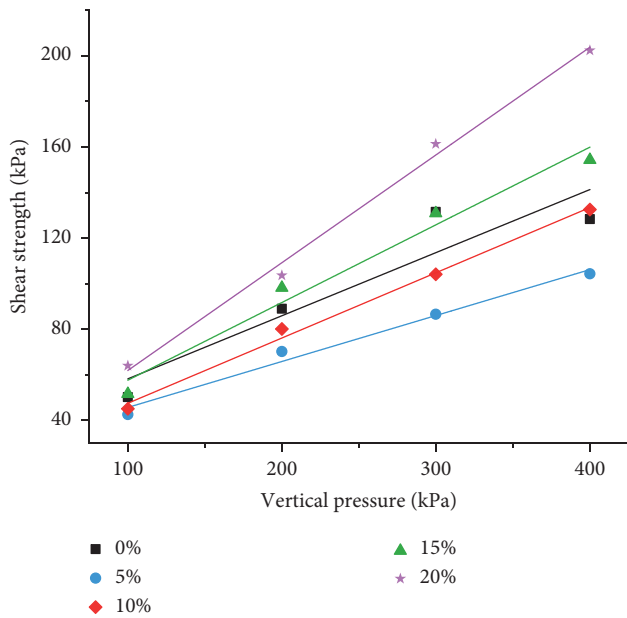
FIGURE 2: Shear strength of red clay samples with different calcium carbonate contents.
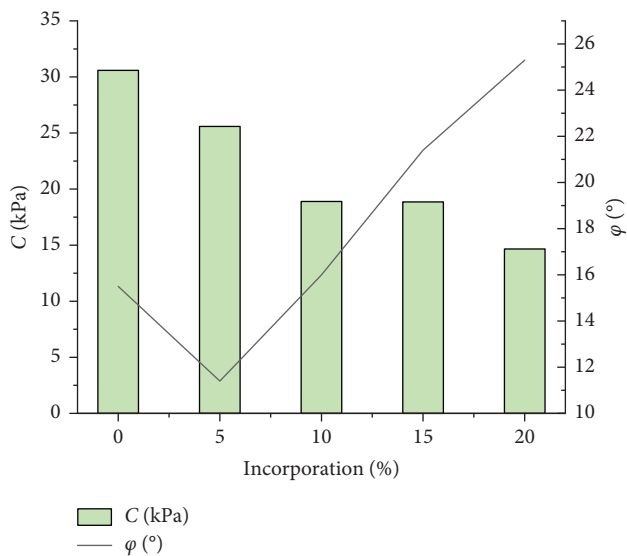

FIGURE 3: Cohesion (C) and internal friction angles (φ) of red clay samples doped with different contents of calcium carbonate.
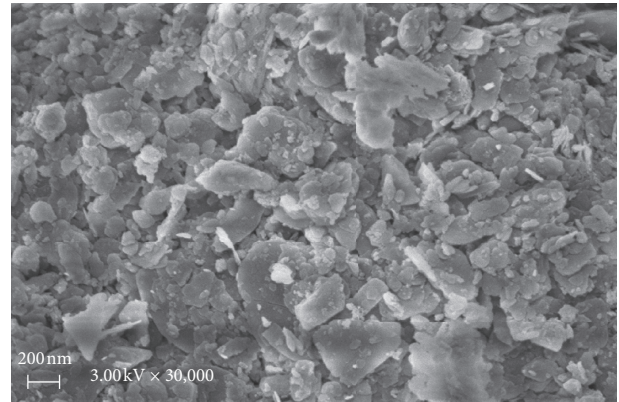

FIGURE 4: SEM image of red clay without calcium carbonate (0%).
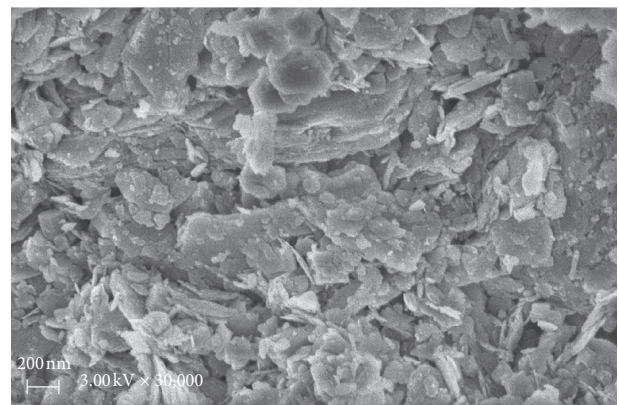

FIGURE 5: SEM image of 15% calcium carbonate-doped red clay.

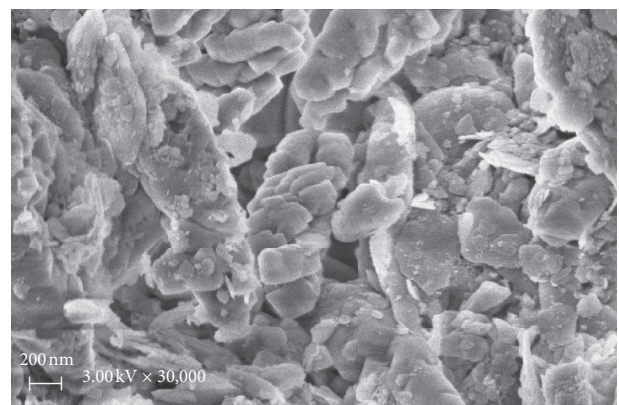FIGURE 6: SEM image of 20% calcium carbonate-doped red clay.

calcium carbonate do not have specific shapes. The distribution of soil particles tends to be random in the sample doped with 15% calcium carbonate (Figure 5). However, it can be clearly seen that the structure becomes loose when the calcium carbonate doping content is 20% (Figure 6). Figures 1(a) and 1(b) show that the spindle-shaped calcium carbonate particles and red clay mineral particles have obviously different shapes, and the calcium carbonate particles are larger than the soil particles. When calcium carbonate is incorporated into red clay, spindle-shaped calcium carbonate particles are embedded in the lamellar soil layers (Figure 7), which destroys the original lamellar soil layers (Figure 7), which destroys the original lamellar

structure of the red clay, causing the sample structure to become looser. Moreover, the greater the amount of calcium carbonate, the more obvious the structural change of the red clay. This is also the reason why the strength of the red clay decreased after calcium carbonate addition. However, when the amount of calcium carbonate was large enough, the effect of friction became more important than that of the loose structure, so the strength of the samples increased.
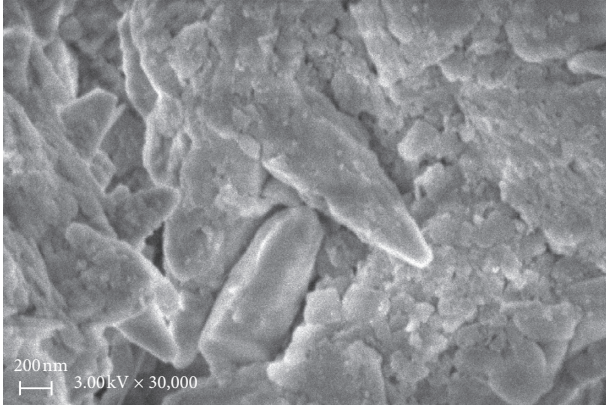
FIGURE 7: SEM image of 20% calcium carbonate-doped red clay.

TABLE 2: Soil and pore parameters obtained by PCAS software.

Parameter (%)	0	5	10	15	20
Pore number	433.6	488.8	679.8	600.8	495.2
Porosity (%)	21.55	22.11	23.86	24.09	28.15
Maximum region area (μm^2)	1.639	0.224	0.154	0.234	0.209
Average region area (μm^2)	0.016	0.004	0.003	0.004	0.005
Average form factor	0.400	0.402	0.367	0.369	0.367
Probability entropy	0.979	0.984	0.988	0.989	0.986
Fractal dimension	1.231	1.236	1.205	1.228	1.218

3.2.2. Quantitative Analysis of Pore Structure. The pores of soil samples doped with different contents of calcium carbonate were analyzed by the PCAS software. The minimum pore threshold was 50 pixels, and the closed radius was 2 pixels. For each soil sample, five SEM images at the same magnification (30,000x) were selected, and then average values were determined. The geometric parameters of the pores and soil particles were calculated using equations (4) and (5). The area of each pixel point after conversion was 12.69 nm^2, and the length of each pixel was 3.563 nm.

The pore number and area determined from the statistical analysis of five SEM images for each sample are summarized in Table 2. Doping with calcium carbonate caused the number of pores in red clay to increase up to the maximum value of 679.8 for the sample with 10% calcium carbonate. The porosity of the samples increased with the amount of calcium carbonate. The highest porosity was obtained for the sample with 20% calcium carbonate, which was 1.3 times larger than the porosity of the undoped red clay. The addition of calcium carbonate substantially lowered the maximum pore area and average pore area of red clay. All doping contents of calcium carbonate had effects on the maximum pore area and average pore area of red clay, indicating that calcium carbonate can fill some of the large pores of red clay and make the pore area relatively uniform.

Table 2 reveals that D_f was between 1.205 and 1.236 for the samples with different calcium carbonate contents. The pore shape was complicated, and D_f did not change markedly after the incorporation of precipitated calcium carbonate. The calcium carbonate content of the samples had no apparent effect on the shape of the pores. The f_f values of the soil were between 0.400 and 0.367, which are much smaller than the f_f of 0.785 for a square. The edges of the pore structures are complicated, and the incorporation of precipitated calcium carbonate did not make the sides of the pores smooth. The influence of the precipitated calcium carbonate on the pore structure of red clay was limited. For the samples with different calcium carbonate contents, H of the pores in red clay is close to 1, indicating that the soil pores have no orientation. As the doping content of calcium carbonate increases to 15%, H of the samples gets closer to 1,

showing that calcium carbonate caused the pores to become more disordered.

According to the International Association of Pure and Applied Chemistry [23], pores with a diameter of less than 2 nm are defined as micropores, pores with a diameter between 2 and 50 nm are defined as mesopores, and pores that are larger than 50 nm in diameter are defined as macropores. In our study, the smallest identifiable pore diameter was 25 nm, so the calcium carbonate-doped red clay samples contain mesopores and macropores. The pore size distributions of the samples are shown in Figure 8. Up to a calcium carbonate content of 10%, the total number of pores in the soil samples increased. The doping content of calcium carbonate had little effect on the number of macropores, whereas it influenced the number of mesopores. It is considered that the added calcium carbonate filled some of the large pores, thus changing macropores into several mesopores, which led to the notable change in the number of mesopores and increased the total number of pores. However, the fluctuation of macropores with changing calcium carbonate content was small.

3.3. Influence of Calcium Carbonate Doping on the Grain Size Distribution of Red Clay. The grain size distributions of the samples are plotted in Figure 9. The particle size of the precipitated calcium carbonate was between 0.2 and 90 μm and that of the red clay was 0.2 to 282 μm. The particle size distributions show that as the amount of calcium carbonate increased, the number of particles with a diameter larger than 282 μm increased. This phenomenon may be caused by the added calcium carbonate inducing aggregation of red clay particles, yielding newly formed particle much larger than the added calcium carbonate particles. The calcium carbonate particles could fill some of the macropores of the soil particles, which lowers the porosity of the red clay.

The nonuniformity coefficient (C_u) is used to indicate the grain composition of soil samples. When C_u is small, the slope of the grain size distribution curve is very steep, the soil particles are relatively uniform, and the grain size gradation is poor. When C_u is large, the particle size gradation curve is gentle, indicating that the grain size gradation is favorable. C_u was calculated using the following equation:

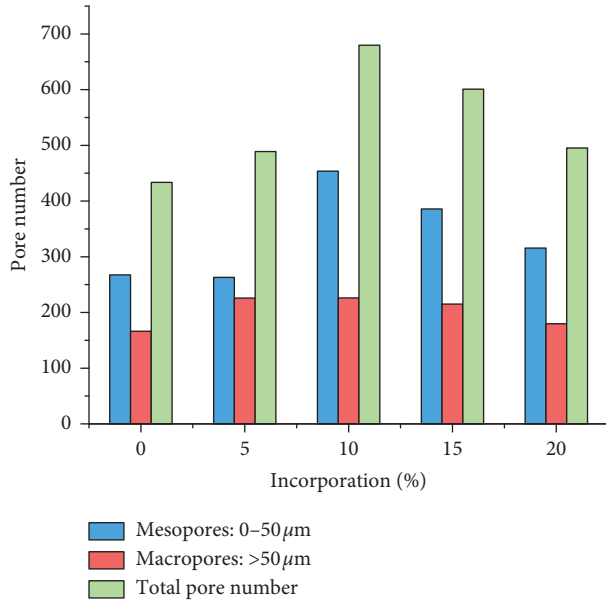$$C_u = \frac{d_{60}}{d_{10}}, \tag{6}$$

FIGURE 8: Distributions of mesopores and macropores in the calcium carbonate-doped red clay samples with different calcium carbonate contents.
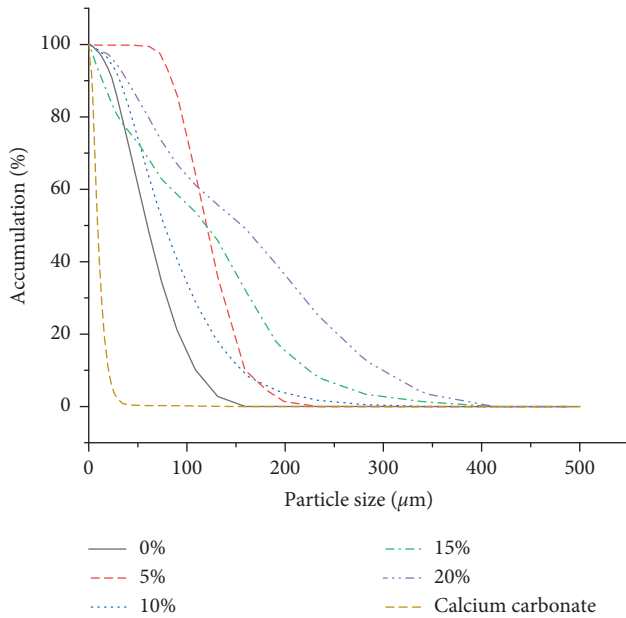

FIGURE 9: Grain size distributions of red clay samples doped with different contents of calcium carbonate.

where d_{60} is the confined particle size with 60% of the soil particles finer than this size and d_{10} is the effective particle size with 10% of the particles finer than this size.

The curvature coefficient (C_c) represents the compositional characteristics of soil particles and was calculated using the following equation:

$$C_c = \frac{(d_{30})^2}{d_{10} \times d_{60}}, \tag{7}$$
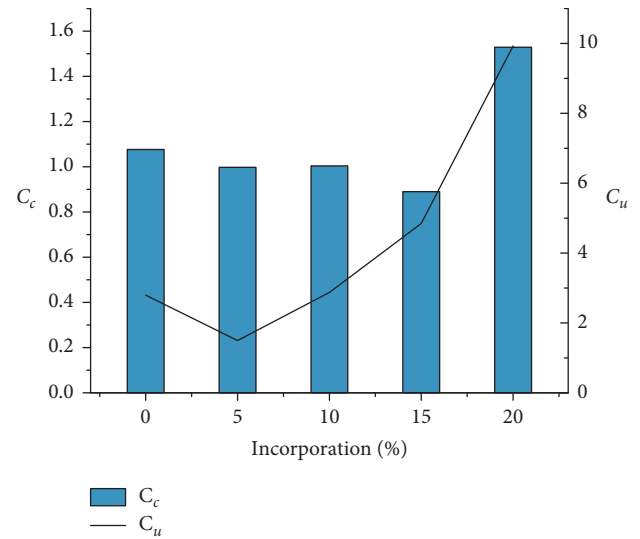

FIGURE 10: Particle size grading curve of red clay samples doped with different contents of calcium carbonate.

where d_{30} is the particle size corresponding to 30% of the ordinate on the particle size gradation curve. When $C_u \geq 5$, and $C_c = 1–3$, the gradation is suitable. If the gradation does not meet both these conditions at the same time, the gradation is poor.

Figure 10 shows that C_u of the red clay is 2.80 and its C_c is 1.08, which means that it is a poorly graded soil. C_u of the red clay samples increases with the doping content of calcium carbonate, illustrating that calcium carbonate modifies the grain size distribution of the soil samples. The addition of less than 15% calcium carbonate had little effect on C_c of the samples. The addition of 20% calcium carbonate increased C_c, making it a well-graded soil. Therefore, the addition of 20% calcium carbonate improved the particle size gradation of red clay and its shear strength.

3.4. Bulk Density Measurements. Figure 11 shows the results of the stacking test of the samples. With the increasing addition of calcium carbonate up to 15%, the loose density of the soil samples decreased markedly. When the calcium carbonate content was 20%, the loose density of the soil sample increased slightly. It can be considered that when the amount of calcium carbonate added is greater than 15%, calcium carbonate has little effect on the loose density of the soil sample. This result is also consistent with the SEM analysis. That is, increasing the calcium carbonate content of the soil samples increases their pore content.

4. Conclusions

The mechanical properties of red clay doped with calcium carbonate first weakened and then strengthened with increasing calcium carbonate content. The maximum shear strength was obtained for the red clay sample doped with 20% calcium carbonate. As the amount of calcium carbonate increased, the cohesion of red clay decreased and the internal friction angle first decreased and then increased, with the
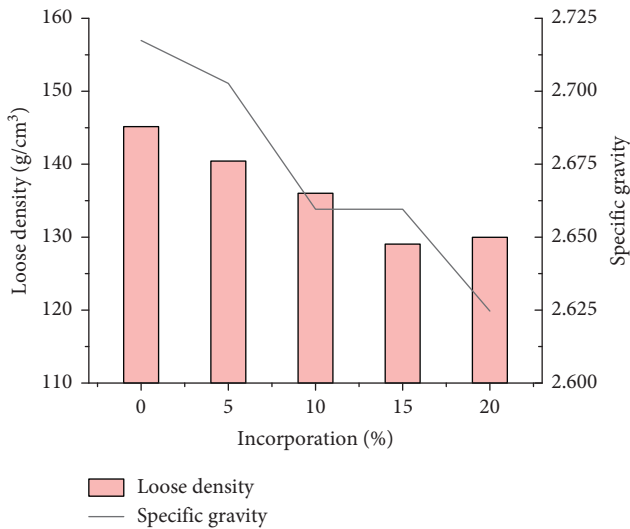
FIGURE 11: Loose density and specific gravity of red clay samples doped with different contents of calcium carbonate.

inflection point at 5% calcium carbonate. Adding calcium carbonate to red clay caused considerable changes of the microstructure of red clay, including substantial changes of porosity. The porosity of the calcium carbonate-doped red clay samples was positively correlated with the calcium carbonate content. The density of calcium carbonate is lower than that of red clay, and the specific gravity of the samples decreased with increasing content of calcium carbonate. The observed decrease of bulk density further proved that the incorporation of calcium carbonate strongly affected the microstructure of red clay, lowering its loose density and increasing its porosity.

Data Availability

The data used to support the findings of this study are available from the corresponding author upon request.

Conflicts of Interest

The authors declare that there are no conflicts of interest regarding the publication of this paper.

Acknowledgments

References

[1] B. D'Angelo, A. Bruand, J. Qin et al., "Origin of the high sensitivity of Chinese red clay soils to drought: significance of the clay characteristics," *Geoderma*, vol. 223–225, pp. 46–53, 2014.

[2] J. Z. Li, L. C. Zhuo, and X. Ni, "Behavior of cemented reticulate red clay," *Advanced Materials Research*, vol. 446–449, pp. 1666–1669, 2012.

[3] J. S. Tingle and R. L. Santoni, "Stabilization of clay soils with nontraditional additives," in *Proceedings of the 8th International Conference on Low Volume Roads*, pp. A72–A84, Reno, NV, USA, June 2003.

[4] F. G. Bell, "Lime stabilization of clay minerals and soils," *Engineering Geology*, vol. 42, no. 4, pp. 223–237, 1996.

[5] S. Pourakbar and B. K. Huat, "A review of alternatives traditional cementitious binders for engineering improvement of soils," *International Journal of Geotechnical Engineering*, vol. 11, no. 2, pp. 206–216, 2017.

[6] N. Latifi, A. Marto, and A. Eisazadeh, "Analysis of strength development in non-traditional liquid additive-stabilized laterite soil from macro-and micro-structural considerations," *Environmental Earth Sciences*, vol. 73, no. 3, pp. 1133–1141, 2015.

[7] X. J. Chen, J. L. Chen, Y. Song, H. Chen, and H. Wang, "Experimental study on strength characteristics of red clay under different particle size of calcium carbonate," in *Proceedings of the International Symposium on Energy Geotechnics*, Lausanne, Switzerland, September 2019.

[8] J. E. Gillott, "Study of the fabric of fine-grained sediments with the scanning electron microscope," *SEPM Journal of Sedimentary Research*, vol. 39, pp. 90–105, 1969.

[9] S. Diamond, "Microstructure and pore structure of impact-compacted clays," *Clays and Clay Minerals*, vol. 19, no. 4, pp. 239–249, 1971.

[10] K. Collins and A. McGown, "The form and function of microfabric features in a variety of natural soils," *Géotechnique*, vol. 24, no. 2, pp. 223–254, 1974.

[11] N. K. Tovey, D. H. Krinsley, D. L. Dent, and W. M. Corbett, "Techniques to quantitatively study the microfabric of soils," *Geoderma*, vol. 53, no. 3-4, pp. 217–235, 1992.

[12] N. K. Tovey and M. W. Hounslow, "Quantitative microporosity and orientation analysis in soils and sediments," *Journal of the Geological Society*, vol. 152, no. 1, pp. 119–129, 1995.

[13] B. Shi, "Quantitative research on the orientation of microstructures of clayey soil," *Acta Geologica Sinica (English Edition)*, vol. 1, pp. 36–44, 1997.

[14] M. R. Cox and M. Budhu, "A practical approach to grain shape quantification," *Engineering Geology*, vol. 96, no. 1-2, pp. 1–16, 2008.

[15] A. Dathe, S. Eins, J. Niemeyer, and G. Gerold, "The surface fractal dimension of the soil-pore interface as measured by image analysis," *Geoderma*, vol. 103, no. 1-2, pp. 203–229, 2001.

[16] C. Liu, B. Shi, J. Zhou, and C. Tang, "Quantification and characterization of microporosity by image processing, geometric measurement and statistical methods: application on SEM images of clay materials," *Applied Clay Science*, vol. 54, no. 1, pp. 97–106, 2011.

[17] K. Jiao, S. Yao, C. Liu et al., "The characterization and quantitative analysis of nanopores in unconventional gas reservoirs utilizing FESEM-FIB and image processing: an example from the lower Silurian Longmaxi Shale, upper Yangtze region, China," *International Journal of Coal Geology*, vol. 128-129, pp. 1–11, 2014.

[18] E. N. Yargicoglu, B. Y. Sadasivam, K. R. Reddy, and K. Spokas, "Physical and chemical characterization of waste wood derived biochars," *Waste Management*, vol. 36, pp. 256–268, 2015.

[19] Y.-L. Qu, W.-K. Ni, F.-J. Niu, Y.-H. Mu, G.-L. Chen, and J. Luo, "Mechanical and electrical properties of coarse-grained soil affected by cyclic freeze-thaw in high cold regions," *Journal of Central South University*, vol. 27, no. 3, pp. 853–866, 2020.

[20] L. Liu, J. Xin, and C. Huan, "Pore and strength characteristics of cemented paste backfill using sulphide tailings: effect of sulphur content," *Construction and Building Materials*, vol. 237, no. 13, 2020.

[21] M. L. Cao, X. Ming, and K. Y. He, "Effect of macro-, micro- and nano-calcium carbonate on properties of cementitious composites a review," *Materials*, vol. 12, p. 20, 2019.

[22] Y. Boyjoo, V. K. Pareek, and J. Liu, "Synthesis of micro and nano-sized calcium carbonate particles and their applications," *Journal of Materials Chemistry A*, vol. 2, no. 35, pp. 14270–14288, 2014.

[23] A. D. McNaught and A. Wilkinson, *IUPAC Compendium of Chemical Terminology, "The "Gold Book""*, Blackwell Scientific Publications, Oxford, UK, 2019.